1-1-2013

Differentiating the Characteristic Response of the Brain After Exposure to Blunt and Blast Trauma

Mark Gregory Tejada Begonia

Differentiating the characteristic response of the brain after exposure to blunt and blast trauma

By

Mark Gregory Tejada Begonia

A Dissertation
Submitted to the Faculty of
Mississippi State University
in Partial Fulfillment of the Requirements
for the Degree of Doctor of Philosophy
in Biomedical Engineering
in the Department of Agricultural and Biological Engineering

Mississippi State, Mississippi

December 2013

Differentiating the characteristic response of the brain after exposure to blunt and blast trauma

By

Mark Gregory Tejada Begonia

Approved:

_____

Lakiesha N. Williams
(Major Professor)

_____

Jun Liao
(Committee Member)

_____

Rajkumar Prabhu
(Committee Member)

_____

Mark F. Horstemeyer
(Committee Member)

_____

Avery James Cooley
(Committee Member)

_____

Steven H. Elder
(Graduate Coordinator)

_____

Achille Messac
Dean
Bagley College of Engineering

Name: Mark Gregory Tejada Begonia

Date of Degree: December 14, 2013

Institution: Mississippi State University

Major Field: Biomedical Engineering

Major Professor: Lakiesha N. Williams

Title of Study: Differentiating the characteristic response of the brain after exposure to blunt and blast trauma

Pages in Study: 133

Candidate for Degree of Doctor of Philosophy

Military personnel often experience mild traumatic brain injury (mTBI) from exposure to improvised explosive devices (IEDs). Soldiers typically endure blast trauma from the IED pressure wave as well as blunt trauma from ensuing head impacts. Researchers have not reached a consensus on whether the biomechanical response from blunt or blast trauma plays a more dominant role in mTBI because the specific biomechanical sources of injury are often undetermined. Consequently, the goal of this dissertation was to conduct three separate studies in order to characterize the mechanical behavior of the brain after exposure to mTBI conditions. For Study 1, mild blunt and blast trauma were induced in Sprague-Dawley rats using a custom-built device. In-house diffusion tensor imaging (DTI) software was used to make 3-D reconstructions of white matter fiber tracts before and after injury (1, 4, and 7 days). Axonal integrity was characterized by examining the fiber count, fiber length, and fractional anisotropy (FA). In-house image analysis software also quantified the microstructural variations in Hematoxylin and Eosin (H&E) stained brain sections, where significant differences in parameters such as the area fraction (AF) and nearest neighbor distance (NND) correlated

to voids that formed after water diffused extracellularly from axons. Study 2 employed a computational approach involving the development of a finite element (FE) model for the rat head followed by the simulation of blunt and blast trauma, respectively. FE parameters such as von Mises stress, pressure, and maximum principal strain were analyzed at various locations including the skull, cerebral cortex, corpus callosum, and hypothalamus to compare injury cases. Study 3 involved interruption mechanical testing of porcine brain, a suitable animal surrogate of human brain. Compression, tension, and shear experiments were performed at a strain rate of 0.1 s^{-1} to examine the differential mechanical response. Microstructural changes in H&E stained brain sections were analyzed with in-house image analysis software to quantify differences among stress states at strains of 0.15, 0.30, and 0.40. Studies 1 and 2 confirmed that the brain behaves differently in response to blunt and blast trauma, respectively, while Study 3 further demonstrated the stress state dependent behavior of brain tissue.

DEDICATION

I want to express my sincere gratitude and appreciation to my family and friends for assisting me throughout this long journey. I wish to dedicate this dissertation to my parents Drs. Greg and Maria Begonia and my brother Michael Begonia for their love and encouragement. I especially want to dedicate this work to my best friend and fiancée Hayley Britt for providing unending support and for bringing so much joy and happiness to my life.

ACKNOWLEDGEMENTS

I wish to acknowledge numerous individuals for their contributions toward this research effort. I want to acknowledge Wilburn Whittington, Joseph Purswell, Brian Luck, and Daniel Chesser for their respective technical assistance in developing our novel test device. I would also like to acknowledge Ruiyi Wu and Song Zhang for lending their computational expertise in diffusion tensor imaging. In addition, I wish to acknowledge Gary Sorrells from the Institute for Imaging and Analytical Technologies (I^2AT) for performing the required scanning. Furthermore, I acknowledge Bridget Willeford, Andrew Claude, and Jennifer Wardlaw for their respective veterinary assistance in completing the experiments. Jim Cooley, Stephanie Mays, and Mike Bassett also need to be acknowledged for their assistance in pathological assessment, histological processing, and animal handling, respectively. Mark Horstemeyer should be acknowledged for cultivating a competitive mindset that kept me driven and prepared for a professional working environment. I also wish to acknowledge Raj Prabhu for enhancing my critical thinking skills by constantly challenging me to synthesize my findings. Jun Liao should also be acknowledged for emphasizing collaborative research and creative problem solving. Lastly, I wish to thank my advisor Lakiesha Williams not only for her professional mentorship, but for her personal and spiritual guidance and for ultimately helping me realize my potential.

TABLE OF CONTENTS

LIST OF TABLES

LIST OF FIGURES

CHAPTER I

INTRODUCTION

1.1 Brain Anatomy

The human brain is a vital and complex organ that is protected by the scalp, skull, and meninges. The meninges consists of connective tissue that attaches to the outer linings of blood vessels and nerve fibers. Figure 1.1 shows the three layers of the meninges, which include the dura mater, the arachnoid, and the pia mater.

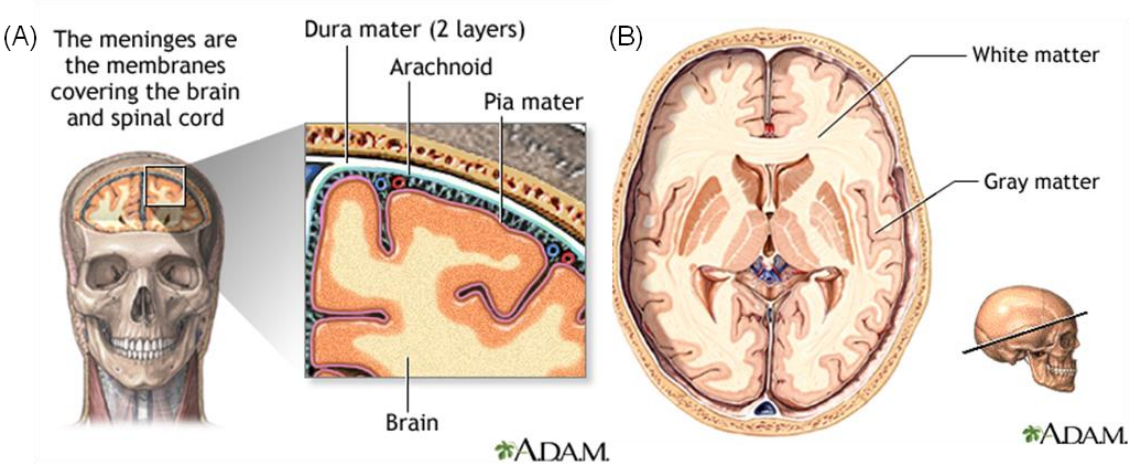

Figure 1.1 Diagrams of the (A) meninges and (B) brain

Notes: Diagram showing (A) connective tissue layers in the meninges and (B) gray matter and white matter regions in the brain (Courtesy: http://www.nlm.nih.gov/medlineplus/ency/imagepages)

The outermost layer of the meninges is a fibrous membrane called the dura mater, which consists of two distinct layers. The periosteal layer (outer layer) lines the inner

surface of the skull while the meningeal layer (inner layer) surrounds the brain. The middle layer of the meninges is the arachnoid, which consists of a webbed structure and is separated from the dura mater by the subdural space. The innermost layer of the meninges is the pia mater, which is separated from the arachnoid by the subarachnoid space. The pia mater consists of a thin network of connective tissue and capillaries that cover the brain surface including the fissures, or grooves (Melvin and Lighthall, 2002).

Cerebrospinal fluid (CSF) is found primarily in the brain ventricles and the subarachnoid space. CSF facilitates the delivery of nutrients to the brain and also functions as a shock absorber. With a specific gravity of 1.008, CSF has a composition similar to blood plasma. In addition, the continuous circulation of CSF (approximately 140 mL) allows it to support the weight of the brain. During normal head movement, the brain experiences minor elastic deformations but the CSF volume fluctuates in order to counterbalance these changes (Melvin and Lighthall, 2002).

The central nervous system (CNS) is composed of the spinal cord and the brain, which can be further separated into either gray matter or white matter. As shown in Figure 1.1, gray matter is found in the internal regions of the brain or along the outer surface. White matter is distributed throughout the intermediate regions of the brain and integrates various sections of the CNS through its fiber tracts. Gray matter mainly consists of neuron cell bodies that are distinguishable by cellular structures such as the soma and dendrites. White matter is primarily composed of neuron processes, or axons, which are encased in a myelin sheath that facilitates signal transmission and provides its distinctive color (Melvin and Lighthall, 2002).

Figure 1.2 shows the microstructure constituting both gray matter and white matter. Axons are only a few microns in diameter and extend from neuronal cell bodies. In addition, axons possess a membrane called the axolemma, which separates the microfilaments and microtubules inside the axon from the biochemical environment outside the axon (Bigler and Maxwell, 2012).

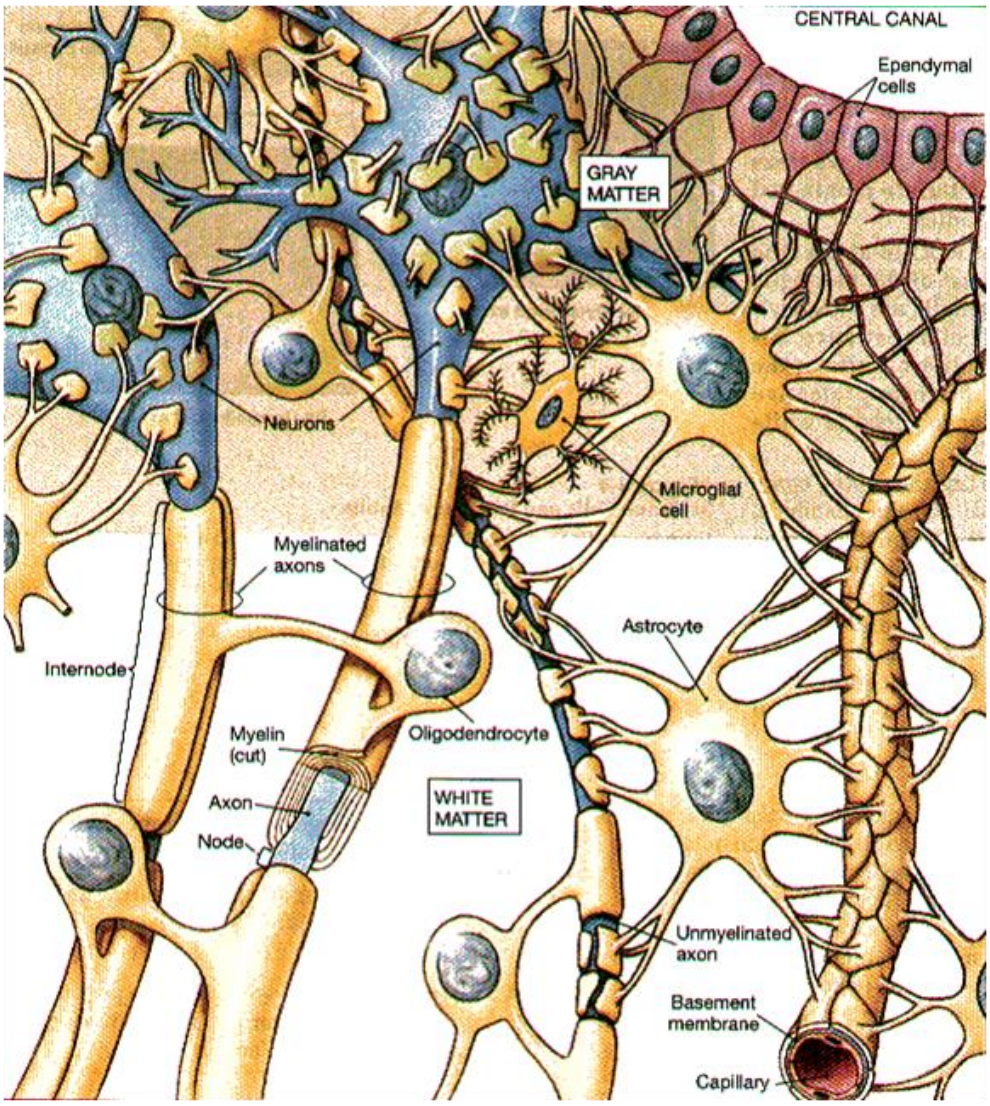

Figure 1.2 Diagram of microstructural components in gray and white matter. (Courtesy: http://fau.pearlashes.com/anatomy/Chapter 17/Chapter 17.htm)

1.2 Mild Traumatic Brain Injury (mTBI)

The term "concussion" is often used interchangeably with "mild traumatic brain injury" (mTBI). In 2009, the Concussion in Sport Group (CISG) proposed a definition for mTBI by stating that (McCrory et al., 2009):

> "Concussion is defined as a complex pathophysiological process affecting the brain, induced by traumatic biomechanical forces. Several common features that incorporate clinical, pathologic and biomechanical injury constructs that may be utilized in defining the nature of a concussive head injury include:
>
> - Concussion may be caused either by a direct blow to the head, face, neck or elsewhere on the body with an impulsive force transmitted to the head.
> - Concussion typically results in the rapid onset of short-lived impairment of neurologic function that resolves spontaneously.
> - Concussion may result in neuropathological changes but the acute clinical symptoms largely reflect a functional disturbance rather than a structural injury.
> - Concussion results in a graded set of clinical symptoms that may or may not involve LOC. Resolution of the clinical and cognitive symptoms typically follows a sequential course however it is important to note that in a small percentage of cases, post-concussive symptoms may be prolonged.
> - No abnormality on standard structural neuroimaging studies is seen in concussion."

1.3 Pathophysiology

Although biomechanical forces can directly produce immediate brain damage, they may also initiate a series of secondary biochemical cascades that gradually lead to cerebral hypofunction or even permanent damage. For instance, traumatic axonal injury (TAI) occurs when axons become completely detached (i.e. secondary axotomy) not because of the initial physical trauma, but due to a series of biochemical processes that subsequently follow. TAI is mainly observed in severe cases of injury but has been seen in mTBI (Barkhoudarian et al., 2011). Figure 1.3 shows various biochemical events involving disrupted metabolic function (1-9) and axonal physiology (A-D).

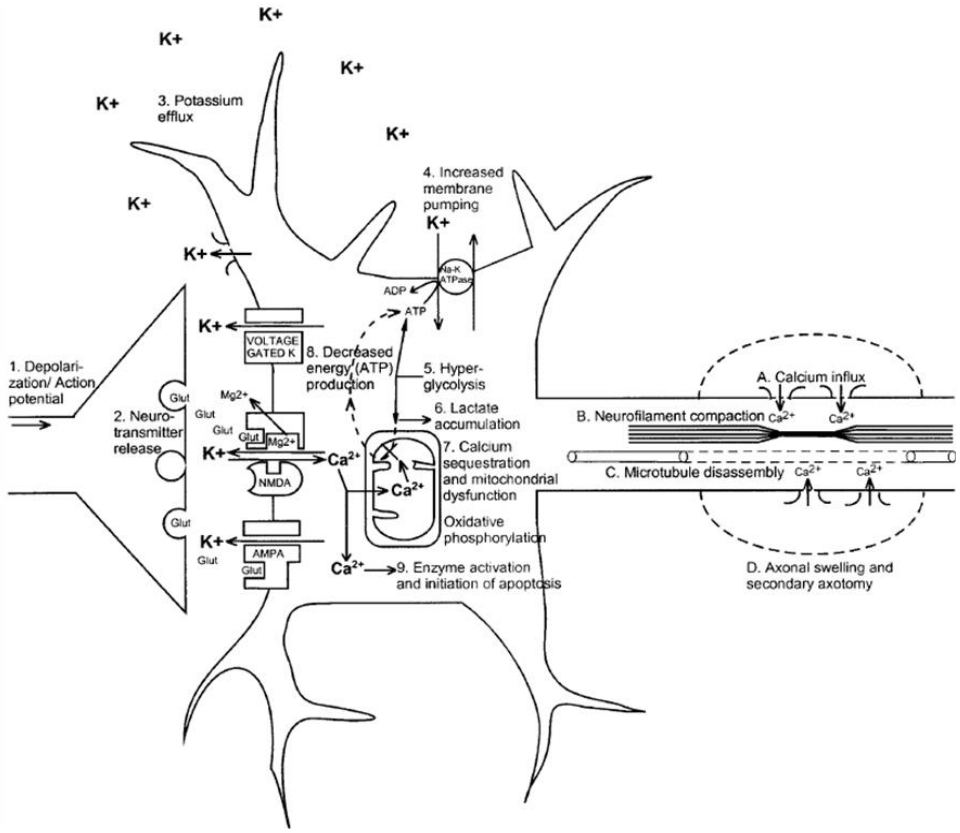

Figure 1.3 Diagram of potential metabolic and axonal consequences of mTBI (Giza and Hovda, 2001).

Diffuse axonal injury (DAI) is one of the most common pathophysiological consequences of TBI, which highlights the susceptibility of white matter to damage (Johnson et al., 2013). DAI is typically associated with axonal deterioration stemming from axolemma disruption, secondary axotomy, and Wallerian degeneration. Researchers originally assumed that DAI was limited to acute or sub-acute post-injury time frames. However, recent studies have shown that axonal deterioration in the human brain can also progress through a long-term, degenerative process (Chen et al., 2009). Table 1.1 provides a summary of research on axonal pathophysiology attributed to either primary mechanical damage or secondary biochemical cascades.

Table 1.1 Overview of previous studies on axonal pathophysiology after TBI.

Researcher(s)	Major Findings
• Holbourn (1943, 1945)	• Induced rotational forces in gelatin molds of human brain • Determined that head rotation produces shear and tensile strain
• Rand and Courville (1946)	• Discovered widespread pathological changes in brain in addition to focal lesions • Proposed that biomechanical forces at the time of injury leads to white matter damage
• Strich (1956, 1961)	• Proposed that shear strain is primarily responsible for white matter damage
• Rewcastle (1967) • Oppenheimer (1968)	• Determined that extent of axonal swelling correlates with injury severity
• Adams et al. (1982)	• Developed concept of “diffuse axonal injury” • Linked DAI to rapid accelerations (e.g. vehicular crashes)and direct impacts (e.g. falls)
• Gennarelli et al. (1982)	• Developed first experimental model of DAI at University of Pennsylvania • Induced DAI in nonhuman primates • Discovered that DAI led to post-traumatic coma

Table 1.1 (Continued)

• Adams et al. (1989)	• Devised DAI grading systems according to extent and distribution of pathology
• Povlishock and Becker (1985) • Christman et al. (1994) • Smith et al. (1999)	• Confirmed that deformation of fiber tracts in white matter can produce axonal swelling hours after trauma
• Christman et al. (1994)	• Proposed that immediate axonal detachment (i.e. primary axotomy) is a rare occurrence • Suggested that secondary axotomy is more frequent
• Smith and Meaney (2000)	• Determined that axons are prone to injury due to anisotropic mechanical properties • Suggested that axons are ductile but behave in a brittle manner following excessive deformation
• Smith et al. (1999)	• Discovered that dynamic stretching causes axons to experience cytoskeletal damage and reduced elasticity, thus producing undulated and misaligned fibers
• Maxwell et al. (2003)	• Observed disruptions in myelin sheath shortly after experimental stretching of guinea pig optic nerve • Suggested that demyelination occurs after TBI
• Baker et al. (2002) • Reeves et al. (2005, 2007)	• Proposed that only small number of axons experience immediate disruption in axonal transport • Determined that mTBI is sufficient to induce pathophysiological changes that eventually lead to axon degeneration
• Tang-Schomer et al. (2010)	• Determined that axonal fibers can become undulated and misaligned due to microtubule damage, thus preventing a return to the original, linear structure

1.4 Neuroimaging Modalities

X-ray computed tomography (CT) is a common neuroimaging modality that provides three-dimensional X-rays of primarily bone structures. Magnetic resonance imaging (MRI) is another common imaging technique that utilizes radiofrequency pulses

to detect changes in the spin signal of hydrogen atoms. Diffusion tensor imaging (DTI) is an advanced MRI sequence that captures the path of water diffusion through tissue microstructure. Another neuroimaging modality is magnetic resonance spectroscopy (MRS), which produces a chemical spectrum of the brain after measuring the concentrations of various chemical components. Lastly, positron emission tomography (PET) is an imaging technique that utilizes isotopes to identify brain regions in which binding or uptake occurs (Shenton et al., 2012). Table 1.2 provides an overview of the aforementioned neuroimaging techniques and their respective advantages.

Table 1.2 Summary of neuroimaging modalities and their advantages.

Imaging Technique	Advantages
CT	• Detecting skull fractures • Detecting abnormalities that require immediate surgical intervention (e.g. subdural hematomas)
MRI	• Better resolution than CT for imaging soft tissue • Differentiating between white and gray matter • Detecting subacute hemorrhages • Detecting macroscopic white matter damage
DTI	• Detecting microscopic white matter damage • Tracing fiber tracts through white matter regions (e.g. corpus callosum)
MRS	• Assessing changes in brain chemistry • Correlating chemical alterations to structural damage, neuronal integrity, and various brain functions
PET	• Assessing accumulation of specific protein or chemical in the brain • Correlating chemical concentrations to neurodegenerative disease and other brain abnormalities

1.5 Diffusion Tensor Imaging (DTI)

1.5.1 Basic Principles

DTI measures the rate and direction of water diffusion in the form of a second-order diffusion tensor, which can be decomposed into eigenvalues and eigenvectors that correlate to the magnitude and orientation of water diffusion, respectively, through each image voxel (Basser et al., 1994). Anisotropic water diffusion is typically observed in white matter because the inherent fiber tracts possess a highly linear structure. Due to the surrounding axonal microstructure, water preferentially diffuses in the axial direction under normal conditions (Correia et al., 2008).

A diffusion tensor can be reduced to scalar parameters that are useful for characterizing various aspects of diffusion. For example, the mean diffusivity (MD) describes the overall rate of diffusion and is derived from the eigenvalues of the diffusion tensor. MD is considered to be rotationally invariant since the corresponding eigenvalues are independent of the axis orientations assigned. Additional scalar parameters include volume ratio (VR), relative anisotropy (RA), and fractional anisotropy (FA), which are also invariant. Equations 1.1, 1.2, 1.3, and 1.4 for MD, VR, RA, and FA, respectively, are expressed in terms of the eigenvalues λ_1, λ_2, and λ_3 below (Vilanova et al., 2005; Zhang et al., 2012).

$$MD = \frac{\lambda_1 + \lambda_2 + \lambda_3}{3} \qquad \text{(Eq. \#1.1)}$$

$$VR = \frac{\lambda_1 \lambda_2 \lambda_3}{\left(\frac{\lambda_1 + \lambda_2 + \lambda_3}{3}\right)^3} \qquad \text{(Eq. \#1.2)}$$

$$RA = \sqrt{\frac{(\lambda_1 - \lambda_2)^2 + (\lambda_2 - \lambda_3)^2 + (\lambda_1 - \lambda_3)^2}{(\lambda_1 + \lambda_2 + \lambda_3)^2}} \quad \text{(Eq. \#1.3)}$$

$$FA = \sqrt{\frac{(\lambda_1 - \lambda_2)^2 + (\lambda_2 - \lambda_3)^2 + (\lambda_1 - \lambda_3)^2}{2(\lambda_1^2 + \lambda_2^2 + \lambda_3^2)}} \quad \text{(Eq. \#1.4)}$$

1.5.2 Anisotropy Classification

The in-house three-dimensional fiber tracking software at Mississippi State University is capable of simulating the physical arrangement of axonal fibers (Zhang et al., 2003; Zhang et al., 2004; Correia et al., 2008; Tate et al., 2010; Zhang et al., 2010). Prior to fiber generation, this software determines the linear anisotropy (c_l), planar anisotropy (c_p), and isotropy (c_s), which were previously defined by Westin et al., 1997. Equations 1.5, 1.6, and 1.7 for c_l, c_p, and c_s, respectively, are expressed in terms of the eigenvalues λ_1, λ_2, and λ_3 below, and Equation 1.8 demonstrates their complementary relationship.

$$c_l = \frac{\lambda_1 - \lambda_2}{\lambda_1 + \lambda_2 + \lambda_3} \quad \text{(Eq. \#1.5)}$$

$$c_p = \frac{2(\lambda_2 - \lambda_3)}{\lambda_1 + \lambda_2 + \lambda_3} \quad \text{(Eq. \#1.6)}$$

$$c_s = \frac{3\lambda_3}{\lambda_1 + \lambda_2 + \lambda_3} \quad \text{(Eq. \#1.7)}$$

$$c_l + c_p + c_s = 1 \quad \text{(Eq. \#1.8)}$$

A large c_l corresponds to a diffusion tensor with one eigenvalue that is significantly larger than the other two. This type of diffusion tensor is typically associated with white matter due to the linearly anisotropic structure of the inherent fiber tracts. A large c_p indicates a diffusion tensor in which an eigenvalue is significantly smaller than the other two. This type of diffusion tensor usually represents tissue structures that are organized into sheets or possess interweaving fiber tracts, which have planar anisotropic features. A large c_s occurs when all three eigenvalues are approximately the same. This type of diffusion tensor is normally seen in gray matter due its isotropic mechanical properties (Zhang et al., 2003).

1.5.3 Streamtube Generation

The MSU fiber tracking software utilizes "streamtubes" to characterize brain regions that are highly anisotropic (i.e. white matter) because they "naturally represent the underlying linear structures, can carry additional information provided by the diffusion tensors, and have the potential to reduce visual clutter (Zhang et al., 2003)." The visual representation of a streamtube is analogous to a hyperstreamline. A streamtube is generated from a trajectory, which corresponds to the eigenvector for λ_1 (i.e. major eigenvector), and a series of cross-sectional ellipses that are connected at different points. The relative shape of the ellipse corresponds to λ_2 and λ_3, and its orientation is defined by the corresponding eigenvectors (i.e. intermediate and minor eigenvectors, respectively). Regions of streamtubes exhibit a redder shading to indicate increasing linear anisotropy and a whiter shading to indicate decreasing linear anisotropy. Figure 1.4 shows the basic process of streamtube generation.

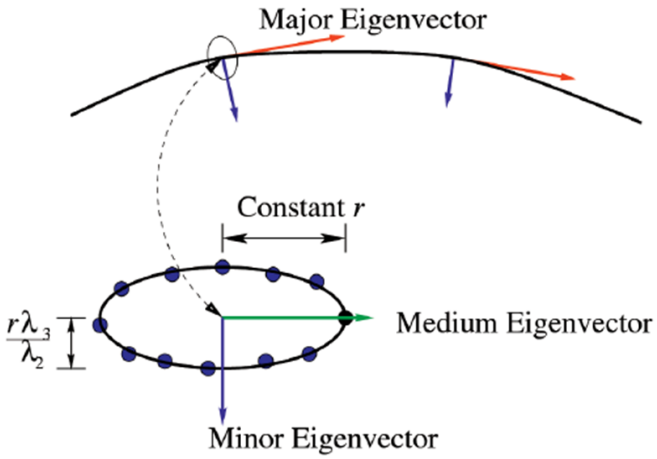

Figure 1.4 Diagram illustrating how streamtubes are produced.

Notes: Generation of a streamtube with a trajectory and an elliptical cross-section.

Generating a representative set of streamtubes can be summarized into three steps: (1) seeding, (2) determining trajectories, and (3) culling. Seed points are assigned to regions identified as highly anisotropic. The number and locations of seed points are not limited to the sample points in the image volume. Streamtubes initially form at a seed point and extend bidirectionally relative to the major eigenvector field. The MSU fiber tracking software utilizes second-order Runge-Kutta integration to determine streamtube trajectories, which are only limited to regions that are highly anisotropic. The software also employs a culling algorithm to reduce the initially dense array of streamtubes in order to produce a realistic representation of streamtubes that correspond to axonal fibers. The culling algorithm removes streamtubes based on trajectory characteristics such as length, linear anisotropy, and degree of separation. The MSU fiber tracking software assesses the similarities between two trajectories by using Equation 1.9. The variable s parameterizes the arc length of the shorter trajectory while s_0 and s_1 represent the endpoints of s. Dist(s) is defined as the shortest distance from a

point on the shorter trajectory to the longer trajectory. As shown in Figure 1.5, the variable T_t determines which sections of the two trajectories should have the separation distance averaged (Zhang et al., 2003; Correia et al., 2008).

$$D_t = \frac{\int_{s_0}^{s_1} \max\left(\text{dist}\left(s\right) - T_t, 0\right) ds}{\int_{s_0}^{s_1} \max\left(\frac{\text{dist}(s) - T_t}{|\text{dist}(s) - T_t|}, 0\right) ds} \qquad \text{(Eq. \#1.9)}$$

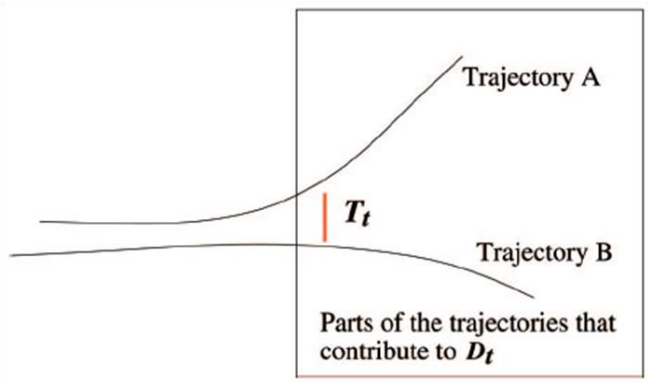

Figure 1.5 Diagram showing relationship between T_t and D_t.

1.6 Dissertation Overview

Three separate studies were completed to contribute toward mechanical characterization of the brain. In Study 1, mild levels of blunt and blast trauma were induced in Sprague-Dawley rats with a custom test device, and in-house diffusion tensor imaging (DTI) software was used to create 3-D reconstructions of axonal fibers both before and after injury (1, 4, and 7 days). Quantitative measures for comparisons included fiber count, fiber length, and fractional anisotropy (FA). Following injury and excision, image analysis was performed on coronal brain sections stained with

Hematoxylin and Eosin (H&E) by using a graphical user interface (GUI) that could quantify microstructural defects through parameters such as area fraction and nearest neighbor distance. In Study 2, experimental conditions were simulated using ABAQUS/Explicit 6.10. Two pressure profiles were incorporated into FE simulations of blast trauma with the first profile corresponding to experimental results and the second profile having a cumulative impulse that was equivalent to the cumulative impulse measured from blunt trauma experiments. The head model comprised four regions that represented the scalp/muscle, skull, cerebrospinal fluid (CSF), and brain. The von Mises stress, pressure, and maximum principal strain were tracked at four locations, which include the skull, cerebral cortex, corpus callosum, and hypothalamus. For study 3, structure-property relationships were determined for porcine brain after completion of interruption compression, tension, and shear experiments at a strain rate of 0.1 s^{-1}. For each stress state, in-house image analysis software was utilized to quantify the variations in brain microstructure at strains of 0.15, 0.30, and 0.40.

1.7 References

Barkhoudarian, G., D.A. Hovda, and C.C. Giza (2011). "The Molecular Pathophysiology of Concussive Brain Injury." *Clincal Journal of Sports Medicine* 30: 33-48.

Basser, P.J., J. Mattiello, and D. LeBihan (1994). "MR Diffusion Tensor Spectroscopy and Imaging." *Biophysical Journal* 66(1): 259-267.

Bigler, E.D. and W.L. Maxwell (2012). "Neuropathology of Mild Traumatic Brain Injury: Relationship to Neuroimaging Findings." *Brain Imaging and Behavior*. DOI: 10.1007/s11682-011-9145-0.

Chen, X.H., V.E. Johnson, K. Uryu, J.Q. Trojanowski, and D.H. Smith (2009). "A Lack of Amyloid Beta Plaques Despite Persistent Accumulation of Amyloid Beta in Axons of Long-Term Survivors of Traumatic Brain Injury." *Brain Pathology* 19: 214-223.

Correia, S., S.Y. Lee, T. Voorn, D.F. Tate, R.H. Paul, S. Zhang, S.P. Salloway, P.F. Malloy, and D.H. Laidlaw (2008). "Quantitative Tractography Metrics of White Matter Integrity in Diffusion-Tensor MRI." *NeuroImage* 42: 568-581.

Giza, C.C. and D.A. Hovda (2001). "The Neurometabolic Cascade of Concussion." *Journal of Athletic Training* 36(3): 228-235.

Johnson, V.E., W. Stewart, and D.H. Smith (2013). "Axonal Pathology in Traumatic Brain Injury." *Experimental Neurology* 246: 35-43.

McCrory, P., W. Meeuwisse, K. Johnston, J. Dvorak, M. Aubry, M. Molloy, and R. Cantu (2009). "Consensus Statement on Concussion in Sport – The 3rd International Conference on Concussion in Sport held in Zurich, November 2008." *Journal of Clinical Neuroscience* 16(6): 755-763.

Melvin, J.W. and J.W. Lighthall (2002). "Brain-Injury Biomechanics." *Accidental Injury: Biomechanics and Prevention*. (Eds.) A.M. Nahum and J.W. Melvin. New York: Springer**,** 277-302.

Shenton, M.E., H.M. Hamoda, J.S. Schneiderman, S. Bouix, O. Pasternak, Y. Rathi, M.A. Vu, M.P. Purohit, K. Helmer, I. Koerte, A.P. Lin, C.F. Westing, R. Kikinis, M. Kubicki, R.A. Stern, and R. Zafonte (2012). "A Review of Magnetic Resonance Imaging and Diffusion Tensor Imaging Findings in Mild Traumatic Brain Injury." *Brain Imaging and Behavior* 6: 137-192.

Tate, D.F., J. Conley, R.H. Paul, K. Coop, S. Zhang, W. Zhou, D.H. Laidlaw, L.E. Taylor, T. Flanigan, B. Navia, R. Cohen, and K. Tashima (2010). "Quantitative Diffusion Tensor Imaging Tractography Metrics are Associated with Cognitive Performance Among HIV-Infected Patients." *Brain Imaging and Behavior* 4: 68-79.

Vilanova, A., S. Zhang, G. Kindlmann, and D.H. Laidlaw (2005). "An Introduction to Visualization of Diffusion Tensor Imaging and Its Applications." *Visualization and Image Processing of Tensor Fields*. (Eds.) J. Weickert and H. Hagen. Netherlands: Springer-Verlag**,** 121-154.

Zhang, J., M. Aggarwal, and S. Mori (2012). "Structural Insights into the Rodent CNS Via Diffusion Tensor Imaging." *Trends in Neuroscience* 35, 412-421.

Zhang, S., J.A. Crow, X. Yang, J. Chen, A. Borazjani, K.B. Mullins, W. Chen, R.C. Cooper, R.M. McLaughlin, and J. Liao (2010). "The Correlation of 3D DT-MRI Fiber Disruption with Structural and Mechanical Degeneration in Porcine Myocardium." *Annals of Biomedical Engineering* 38(10): 3084-3095.

Zhang, S., C. Demiralp, and D.H. Laidlaw (2003). "Visualizing Diffusion Tensor MR Images Using Streamtubes and Streamsurfaces." *IEEE Transactions on Visualization and Computer Graphics* 9(4): 454-462.

Zhang, S., G. Kindlmann, and G.H. Laidlaw (2004). "Diffusion Tensor MRI Visualization." *Visualization Handbook*. (Eds.) C.D. Hansen and C.R. Johnson. Oxford: Academic Press**,** 327-340.

CHAPTER II

DIFFUSION TENSOR IMAGING AND MICROSTRUCTURAL ANALYSIS OF RAT BRAIN AFTER MILD BLUNT AND BLAST TRAUMA

2.1 Introduction

In the United States alone, over 1.7 million individuals sustain a traumatic brain injury (TBI) each year. TBI is a major factor in nearly one-third (30.5%) of all injury-related deaths (Faul et al., 2010) and has resulted in medical costs estimated to be over $60 billion (Finkelstein et al., 2006). Although the severity of TBI can vary, cases of mild TBI (mTBI) are far more common (Bigler and Maxwell, 2012). Military personnel have become increasingly vulnerable to TBI from exposure to improvised explosive devices (IEDs) (Appelboom et al., 2012). During Operation Iraqi Freedom and Operation Enduring Freedom, 59% of U.S. service members suffered from TBI with 44% of those individuals experiencing mTBI (Okie, 2005). Diagnosis of mTBI is challenging since clinical signs can be physical, behavioral, cognitive, or emotional (McCrory et al., 2009). Furthermore, it is difficult to identify the predominant biomechanical factors involved in mTBI because soldiers can experience blast trauma from the IED pressure wave and blunt trauma from subsequent head impacts. When military personnel experience mTBI, they often return to full duty status immediately after clinical signs begin to disappear, but returning prematurely can increase the risk for repeat injury and other long-term consequences (MacGregor et al., 2011). Previous studies have shown

that mTBI patients may experience further complications from post-concussive syndrome (PCS) (Schneiderman et al., 2008; Belanger et al., 2010; Bryant et al., 2010) or exhibit symptoms similar to post-traumatic stress disorder (PTSD) (Hoge et al., 2008; Carlson et al., 2010; Levin et al., 2010; Carlson et al., 2011). Some patients might experience deteriorating brain function after mTBI while others will exhibit full recovery. The underlying mechanisms of these unpredictable patient outcomes warrant further investigation and have significant clinical implications (Budde et al., 2011).

Accurate diagnosis of mTBI is challenging because histological and immunohistochemical techniques are invasive (Li et al., 2011). In addition, TBI is not always detectable through standard magnetic resonance imaging (MRI) or computerized tomography (CT) (Arfanakis et al., 2002; Huisman et al., 2004). Diffusion tensor imaging (DTI) offers researchers a viable alternative since this advanced MRI technique provides enhanced visualization of tissue microstructure (Sundgren et al., 2004). DTI has been performed on various tissues including the spinal cord (Ducreaux et al., 2007; Ozanne et al., 2007), myocardium (Wu et al., 2007; Zhang et al., 2010), and skeletal muscle (Heemskerk et al., 2007; Lansdown et al., 2007). DTI has also been utilized in the brain to assess the integrity of white matter due to the anisotropic properties of its fiber tracts (MacDonald et al., 2007). According to a review by Margulies and Hicks (2009), animal models of closed-head injuries (i.e. blunt trauma) exhibited pathological features that were also found in cases of blast TBI (i.e. blast trauma) (Margulies and Hicks, 2009). Some researchers argue that blunt and blast trauma differ based on the respective temporal, spatial, and recurrent pathological features (Ling et al., 2009). However, other investigators suggest that these two sources of injury are comparable

since they both lead to similar cognitive consequences (Belanger et al., 2009). Although the distinctions between blunt and blast trauma remain unclear (Elder and Cristian, 2009; Cernak and Noble-Haeusslein, 2010; Hicks et al., 2010), effective comparisons can be achieved by examining the brain microstructure through both DTI and image analysis.

In the present study, we induced mild levels of blunt and blast trauma in Sprague-Dawley rats with a custom test device. We also employed DTI to track injury progression after 1, 4, and 7 days using quantitative measures including fiber count, fiber length, and fractional anisotropy (FA). TBI consists of two injury phases with primary injury occurring immediately after the initial trauma and secondary injury manifesting hours or days afterward (O'Connor et al., 2011). The post-injury times in this study are based on previous mTBI research (Barkhoudarian et al., 2011; Bigler and Maxwell, 2012) and were chosen since DTI is capable of detecting subtle brain damage linked to secondary injury (Shenton et al., 2012). Following injury and excision, we performed image analysis on coronal brain sections stained with Hematoxylin and Eosin (H&E) by using a graphical user interface (GUI) that could quantify microstructural defects through parameters such as object area and nearest neighbor distance. Although there are numerous studies involving animal models of TBI, few have utilized DTI and quantitative analysis of histological images to differentiate between the underlying effects of blunt and blast trauma on the brain microstructure within the milder regime of injury. Thus, our goals are to determine not only if, but also why the brain responds uniquely to these two sources of injury. This study will provide further insight into whether blunt trauma or blast trauma plays a more significant role in the progression of mTBI in patients exposed to both events. A clearer understanding of this distinction could

ultimately lead to more biofidelic constitutive models of the brain, more accurate diagnoses of mTBI patients, and pharmaceutical treatments designed to target specific secondary injury cascades.

2.2 Methods

2.2.1 Animals

A total of 28 male Sprague-Dawley rats (300-325 g, Harlan Laboratories) were used in this study. Animals were housed in cages under a 12 hour dark/light cycle with access to food pellets and water ad libitum and were given 3-7 days to acclimate before testing. All procedures were approved by the MSU Institutional Animal Care and Use Committee (IACUC). Animals were assigned to one of seven groups (n=4). The controls were assigned to Group 1 while Groups 2, 3, and 4 were exposed to blunt trauma and then scanned at recovery times of 1, 4, and 7 days, respectively. Groups 5, 6, and 7 were exposed to blast trauma and then scanned at recovery times of 1, 4, and 7 days, respectively.

2.2.2 Experimental Setup

The test device utilized compressed nitrogen and its main components included a pressure vessel (Buckeye Fabricating Co., Springboro, OH), a pneumatic actuator (Valtorc International, Kennesaw, GA), and an LTV-35 control valve with a flip toggle switch (Mead Fluid Dynamics, Chicago, IL). The experimental setup for blunt trauma featured an air cylinder with a 1.9 cm (3/4 in.) bore diameter and 7.6 cm (3 in.) stroke Figure 2.1. The air cylinder was fitted with a custom impactor tip and an A401 FlexiForce sensor (Tekscan, Boston, MA), which was connected to a multifunction DAQ

device (NI USB-6351, National Instruments, Austin, TX) capable of acquiring 1.25 x 10^6 samples per second. Groups 2-4 were exposed to an impact depth of 1 mm at an impact velocity of approximately 2.2 m/s. In blast trauma experiments, the pressure was set to 689 kPa (100 psi) and animals were positioned 2.5 (1 in.) cm away from the nozzle Figure 2.1. For calibration purposes, cadaver experiments were performed and resistors were changed accordingly in order to indicate the pressure impacting the surface of the animal's skull. After experiments were complete, rats were administered atipamezole (0.5-1.0 mg/kg, IM) and then buprenorphine (0.01 mg/kg, SQ) during recovery.

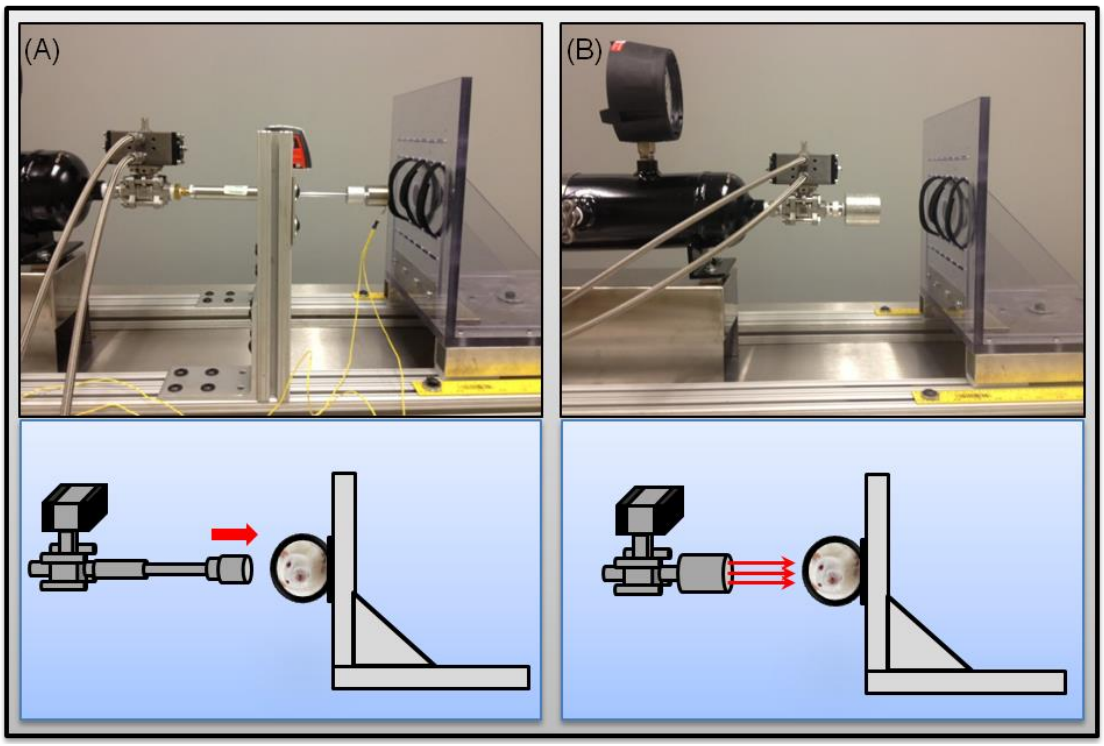

Figure 2.1 Diagram of test device and schematic representation for inducing (A) blunt trauma and (B) blast trauma.

2.2.3 Image Acquisition

Scans were acquired with a 3.0T MRI full body scanner (Signa HDx, General Electric Medical Systems, Milwaukee, WI) using a wrist coil (Mayo Wrist Coil, Part No. 13G5614). Standard pulse sequences were optimized for the tissues scanned and with a localizer to facilitate the initial setup. Table 2.1 provides a summary of the pulse sequences utilized for imaging: 3-D Fast Spoiled Gradient Recall (3D FSPGR), T2 Fast Spin Echo (T2 FSE), T2 Fluid Attenuated Inversion Recovery (FLAIR), T2 Fast Gradient Recall Echo (T2* or FGRE), Diffusion Weighted Imaging (DWI), Diffusion Tensor Imaging (DTI), and T1 fast spin echo (T1 FSE). The b values for the DWI and DTI scans were 0 and 800, respectively, with the DTI scan utilizing 21 gradient directions. Parameters including the flip angle, echo train length, and field of view (FOV) varied depending on the pulse sequence selected. The flip angle was 20° for the 3D FSPGR sequence and 25° for the FGRE sequence. The echo train length was 4 for the T1 FSE sequence and 24 for the T2 FSE sequence. Furthermore, the FOV for the T2 Flair, DWI, DTI, and T1 FSE sequences was 8 x 8 cm while the FOV for the 3D FSPGR, T2 FSE, and FGRE sequences was 8 x 7.2 cm. All sequences were acquired with no spacing except for the 3D FSPGR sequence, which had a 0.5 mm overlap. Due to time constraints, scans were obtained in the axial direction only and were optimized with different TR values to accommodate the variations in slice number. Each animal was scanned before injury and 1, 4, or 7 days afterward with each scan completed within approximately 30 minutes.

Table 2.1 Summary of pulse sequences and corresponding parameters included in the scanning protocol.

Sequence	Median TR	Effective TE	Bandwidth	Slice Thickness (mm)	Matrix (Frequency x Phase)	NEX	Resolution
3D FSPGR	10.9	$\leq$ 5.6	19.23	1	288 x 224	2	0.27 x 0.32
T2 FSE	4750	85	31.25	1.6	288 x 224	4	0.27 x 0.32
T2 Flair	7500	120	31.25	1.6	288 x 224	2	0.27 x 0.36
FGRE	150	$\leq$ 5.6	25	1.6	288 x 224	3	0.27 x 0.32
DWI	12000	N/A	N/A	2.4	160 x 160	4	0.5 x 0.5
DTI	15000	N/A	N/A	2.4	160 x 160	2	0.5 x 0.5
T1 FSE	525	$\leq$ 8.4	20.83	2.4	160 x 160	2	0.5 x 0.5

List of acronyms: 3-D Fast Spoiled Gradient Recall (3D FSPGR), T2 Fast Spin Echo (T2 FSE), T2 Fluid Attenuated Inversion Recovery (FLAIR), T2 Fast Gradient Recall Echo (T2* or FGRE), Diffusion Weighted Imaging (DWI), Diffusion Tensor Imaging (DTI), and T1 fast spin echo (T1 FSE).

2.2.4 DTI Analysis

An in-house three-dimensional fiber tracking model was used to simulate the physical arrangement of axonal fibers (Zhang et al., 2003; Zhang et al., 2004; Correia et al., 2008; Tate et al., 2010; Zhang et al., 2010). The major eigenvector field of the diffusion tensor field produced a set of integral curves (Basser et al., 2000) that solved Equation 2.1, where p(r) is the generated streamline, r is the arc length of the generated streamline, and the vector v is the vector field generated from the major eigenvector of the diffusion tensor.

$$p(r) = \int_0^r \vec{\nu}(p(s))\, ds \qquad \text{(Eq. \#2.1)}$$

Minimum anisotropy, minimum length, and maximum curvature were the predefined constraints used to remove inaccurate curves that generated from noise, partial volume effects, or other imaging artifacts (Zhang et al., 2003). Fiber tracts were integrated in the major eigenvector field integration and stopped if: (1) linear anisotropy was too low, (2) signal-to-noise ratio was too low, (3) or directional change was too high. Fiber tracts were densely seeded throughout the volume, and a culling algorithm selected fibers based on the minimum distance between any two fibers in the model, or culling distance threshold. This culling process produced 3-D reconstructions of fiber that reduced visual clutter and improved interactivity (Zhang et al., 2003). Fiber tracts were generated with the linear anisotropy threshold set to 0.1, initial seeds spaced at 1 mm3 per seed, and the culling distance threshold set to 0.25 mm. The color mapping along the fiber tracts indicated the level of linear anisotropy. Fiber tract regions were white to indicate lower linear anisotropy and red to indicate higher linear anisotropy.

2.2.5 Histological Processing

Rats were euthanized via transcardial perfusion within 2-3 hours after scanning was complete. Rats were anesthetized using dexmedetomidine (0.05-0.1 mg/kg, IP) and fentanyl (0.1 mg/kg, IP) followed by propofol (100 mg/kg, IP). A peristaltic pump (Cole-Parmer, Vernon Hills, IL) set at 20 mL/min was used to perfuse the animal with a 50 mL prewash of phosphate buffered saline (pH 7.4; Sigma-Aldrich, St. Louis, MO), followed by 250 mL of 10% neutral buffered formalin (Surgipath Medical Industries, Richmond, IL). A stereotaxic atlas was used for obtaining coronal sections from the brain region comprising the corpus callosum (Paxinos and Watson, 2007). A Leica RM2255 rotary microtome (Leica Microsystems Inc., Buffalo Grove, IL) was used to cut 5 µm paraffin

embedded sections, which were placed in a water bath at 39°C and mounted onto charge plus slides. Prior to H&E staining, slides were deparaffinized in Xylene for 10 minutes and rehydrated using a graded ethanol series. Slides were stained with Hematoxylin for 8 minutes, rinsed sequentially in acid alcohol, distilled water, and ammonia water, and then stained with Eosin for 2-3 minutes. Slides were subsequently dehydrated in a graded ethanol series and suspended in Xylene to be cover-slipped.

2.2.6 Image Analysis

All images were acquired with a LEICA DM2500 microscope at an objective magnification of 20X (Leica Microsystems Inc., Buffalo Grove, IL). The total analysis area for each region-of-interest (ROI) within the corpus callosum was 2.0137 x 105 μm2. Our in-house image analysis software (ImageAnalyzer Ver. 2.2-0) was utilized for this study. This GUI provides analysis parameters that are designed for integration with a constitutive, or material, model that can be modified to include specific damage criteria. The area fraction and nearest neighbor distance (μm) were the quantitative parameters used to characterize the voids that we believed were the by-products of altered water diffusion in axons after they entered an injured state. The area fraction is defined as the area of voids detected divided by the total image area. The nearest neighbor distance quantified the space separating the centroids of each void detected. After converting images from RGB to grayscale intensity, the GUI analyzed images based on the minimum object area and threshold range. Figure 2.2 shows image analysis results including the (A) original ROI and (B) voids detected by the GUI.

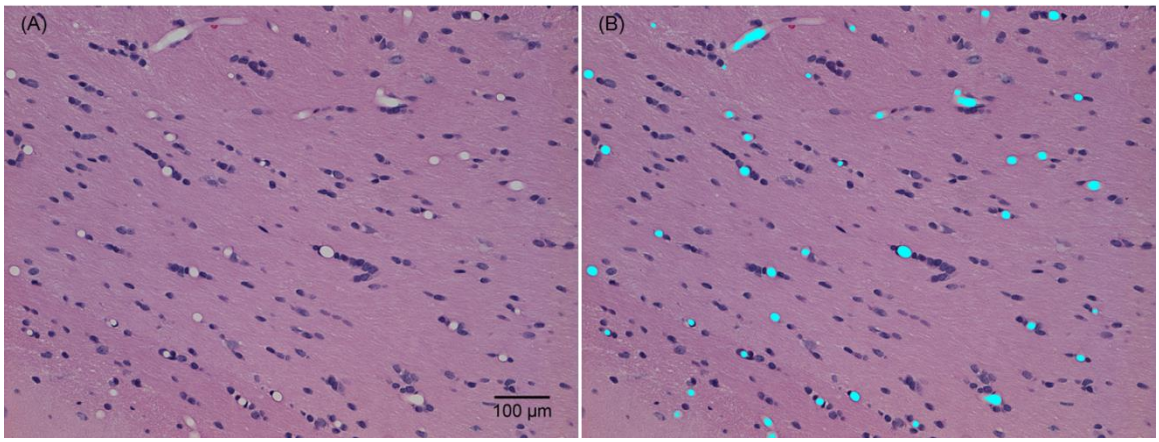

Figure 2.2 H&E brain images (A) before and (B) after image analysis.

Notes: Pre- and post-processing results from ImageAnalyzer Ver. 2.2-0, which shows the (A) original ROI and (B) voids identified by the GUI (shaded in cyan).

2.2.7 Statistical Analysis

All data were plotted as mean ± standard error of the mean (SEM). Statistical analysis was performed using IBM SPSS Statistics Ver. 20 (IBM Corp., Armonk, NY). One-way ANOVA was performed on each parameter with Tukey's HSD test selected for post-hoc comparisons. A p-value of less than 0.05 was considered to be statistically significant for pairwise comparisons between injury cases at each recovery time and for comparisons between injured animals (Groups 2-7, respectively) and healthy animals (Group 1).

2.3 Results

Any given diffusion tensor can be visualized as an ellipsoid with its axis lengths and orientations corresponding to the eigenvalues and eigenvectors of that tensor, respectively. As shown in Equation 2.2, fractional anisotropy (FA) is calculated from the eigenvalues (λ_1, λ_2, and λ_3) of the diffusion tensor (Zhang et al., 2012).

$$FA = \sqrt{\frac{(\lambda_1 - \lambda_2)^2 + (\lambda_2 - \lambda_3)^2 + (\lambda_1 - \lambda_3)^2}{2(\lambda_1^2 + \lambda_2^2 + \lambda_3^2)}} \quad \text{(Eq. \#2.2)}$$

FA was analyzed for this study since it is one of the most common DTI measures used for assessing variations in the paths of water diffusion through white matter fiber tracts (Bigler, 2012). Our in-house DTI fiber tracking software also measured fiber count and fiber length, which were both used to characterize the structural integrity of fiber tracts. In addition to DTI measures, we selected two parameters provided by our image analysis GUI. Both the area fraction and nearest neighbor distance were used to track water diffusing from axonal fibers to the extracellular matrix. Results from DTI and image analysis are summarized in Table 2.2.

Table 2.2 Summary of DTI measures and image analysis parameters based on injury case and recovery time.

11	Recovery Time (Days)	Fiber Count	Fiber Length (mm)	Fractional Anisotropy	Area Fraction (%)	Nearest Neighbor Distance (μm)
Control	N/A	2343 ± 271	7.48 ± 0.21	0.107 ± 0.003	0.75 ± 0.04	41.41 ± 2.38
Blunt	1	973 ± 150	7.30 ± 0.19	0.073 ± 0.013	3.11 ± 0.52	9.52 ± 0.71
Blunt	4	960 ± 66	7.02 ± 0.10	0.098 ± 0.017	4.30 ± 0.43	9.53 ± 0.84
Blunt	7	1007 ± 102	6.98 ± 0.14	0.074 ± 0.010	2.39 ± 0.41	12.19 ± 1.32
Blast	1	954 ± 109	7.17 ± 0.11	0.091 ± 0.010	1.47 ± 0.19	19.85 ± 2.46
Blast	4	858 ± 56	7.16 ± 0.17	0.128 ± 0.009	2.67 ± 0.24	18.40 ± 2.85
Blast	7	1025 ± 85	7.29 ± 0.10	0.125 ± 0.011	1.67 ± 0.16	20.26 ± 2.20

All data are shown as Mean ± SEM.

Figure 2.3 and Figure 2.4 illustrate the approximate location of 3-D DTI fibers generated after blunt and blast trauma, respectively. This brain region primarily comprised the corpus callosum. Figure 2.5 and Figure 2.6 exhibit the arrangement of 3-D DTI fibers following blunt and blast trauma, respectively, which demonstrated a more disorganized alignment compared to the controls. Furthermore, the 3-D DTI fiber models generated after blunt and blast injury, respectively, appeared more asymmetrical compared to the 3-D DTI fiber models of the controls.

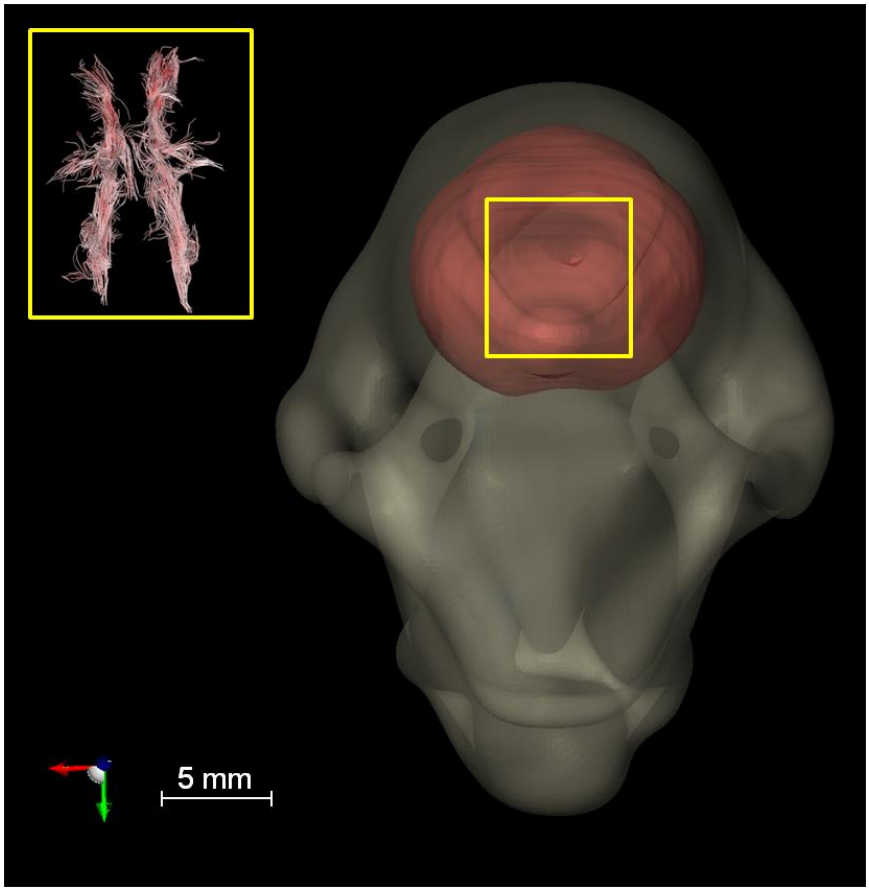

Figure 2.3 Coronal view of the brain region where 3-D DTI fibers were primarily generated, which mainly comprises the corpus callosum.

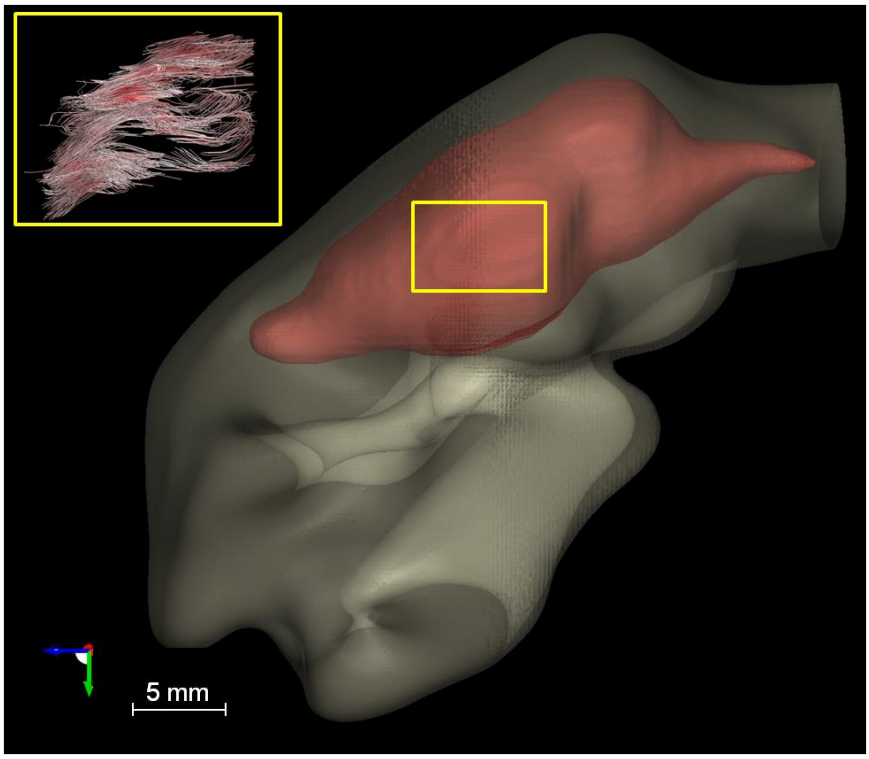

Figure 2.4 Sagittal view of the brain region where 3-D DTI fibers were primarily generated, which mainly comprises the corpus callosum

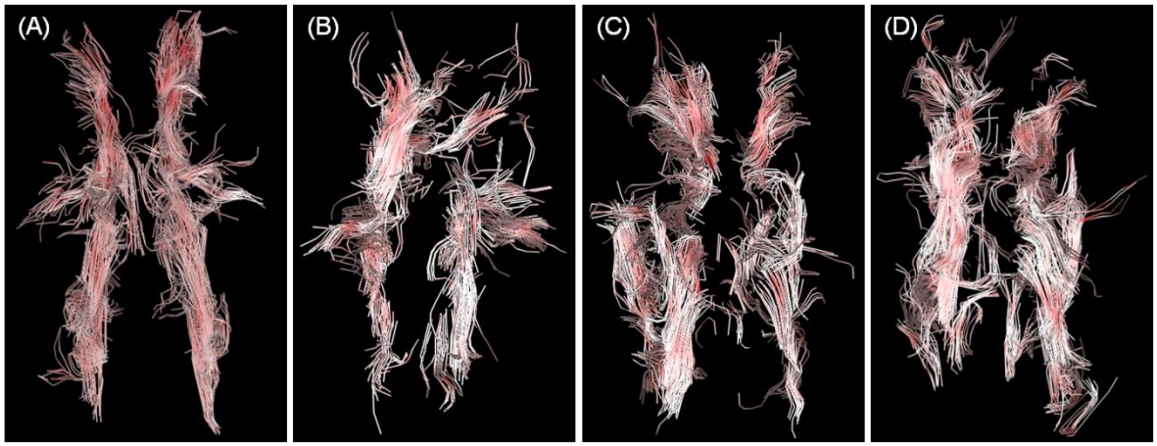

Figure 2.5 Coronal view of 3-D DTI fibers for the (A) control group and blunt trauma groups at (B) Day 1, (C) Day 4, and (D) Day 7.

Notes: Fiber tract regions are shaded white to indicate lower linear anisotropy and shaded red to indicate higher linear anisotropy.

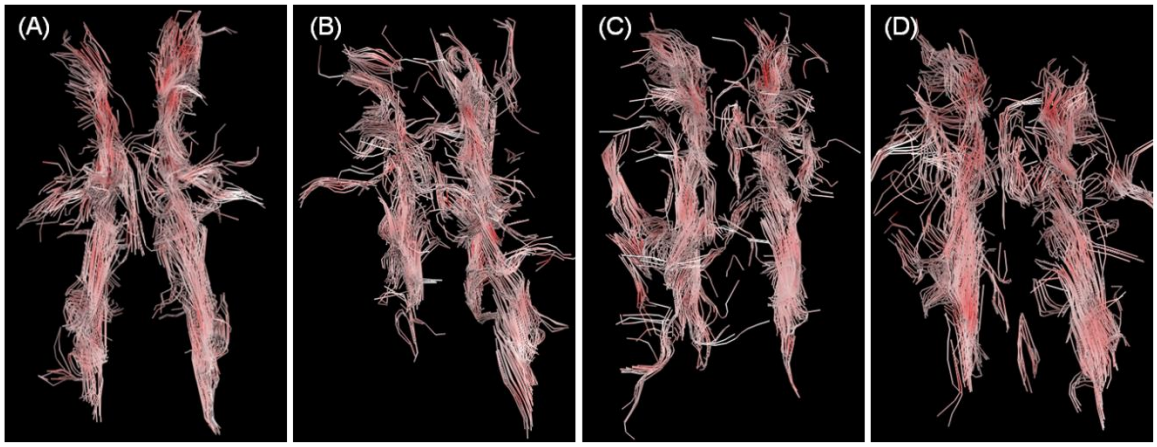

Figure 2.6 Coronal view of 3-D DTI fibers for the (A) control group and blast trauma groups at (B) Day 1, (C) Day 4, and (D) Day 7.

Notes: Fiber tract regions are shaded white to indicate lower linear anisotropy and shaded red to indicate higher linear anisotropy.

Post-hoc analysis confirmed that both blunt and blast trauma produced significantly lower fiber counts on Days 1, 4, and 7 compared to Day 0 (Figure 2.7). Further analysis of the fiber count per volume followed a similar trend (Figure 2.8). However, there were no significant changes in fiber length after either blunt or blast trauma from Day 0 to Day 7 (Figure 2.9). Pairwise comparison at each recovery time revealed a significant difference in the FA between injury cases ($p=0.02$) on Day 7 but not on Days 1 or 4 (Figure 2.10). More importantly, blunt trauma produced a lower FA on Day 7 (0.074 ± 0.010) compared to the control group (0.107 ± 0.003) while blast trauma produced a higher FA (0.125 ± 0.011).

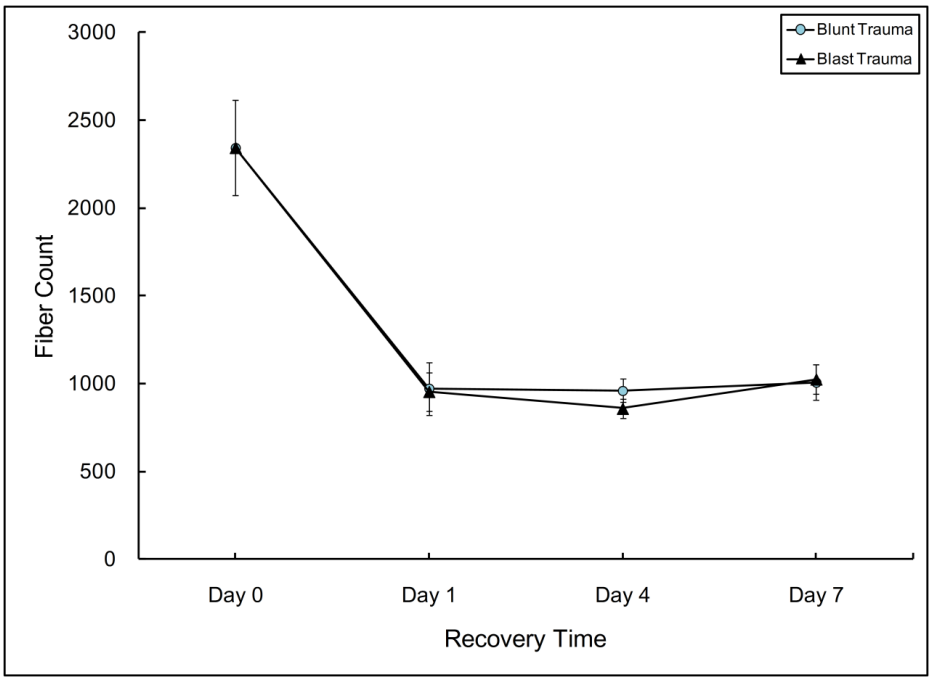

Figure 2.7 Comparison of fiber counts (Mean ± SEM) between blunt and blast groups at recovery times of 1, 4, and 7 days.

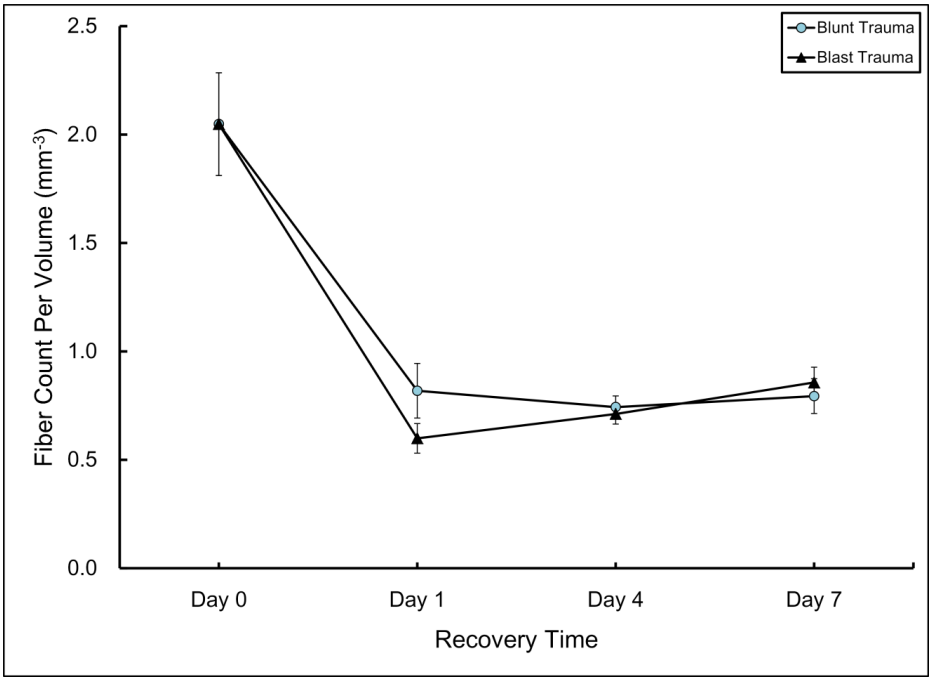

Figure 2.8 Comparison of fiber count per volume (Mean ± SEM) between blunt and blast groups at recovery times of 1, 4, and 7 days.

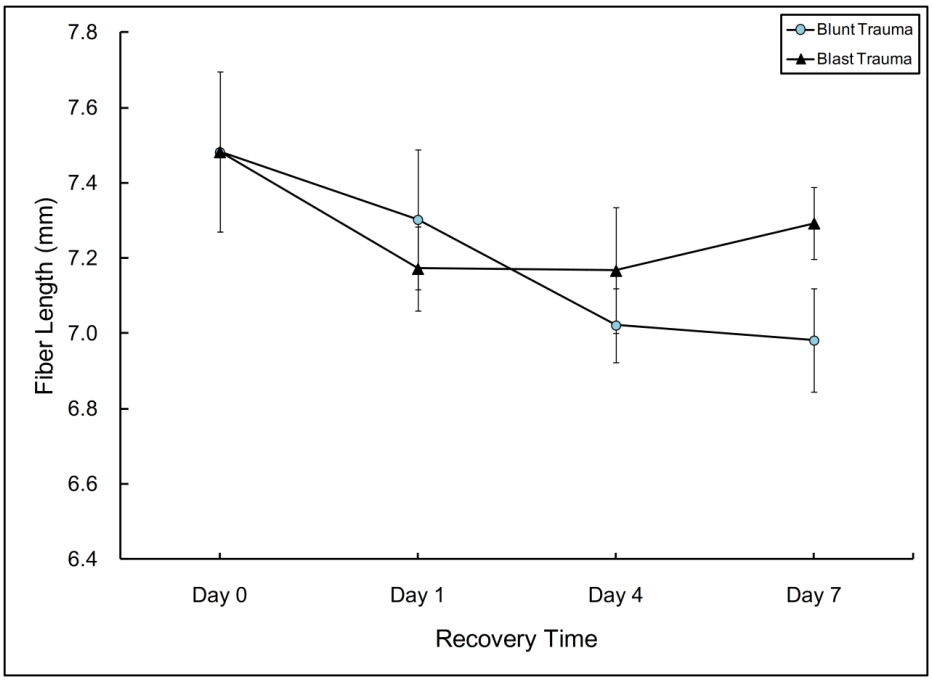

Figure 2.9 Comparison of fiber lengths (Mean ± SEM) between blunt and blast groups at recover times of 1, 4, and 7 days.

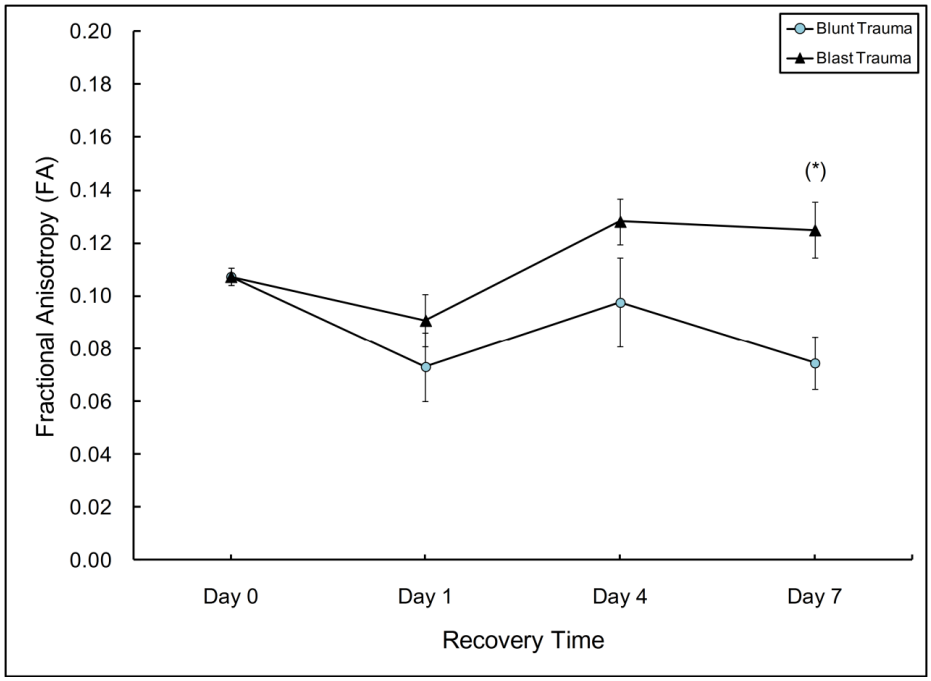

Figure 2.10 Comparison of fractional anisotropy (Mean ± SEM) between blunt and blast groups at recover times of 1, 4, and 7 days.

A higher frequency of voids were detected in the extracellular matrix after blunt (Figure 2.11) and blast trauma (Figure 2.12) in contrast to controls. Blunt injury produced significant increases in area fraction on Days 1 through 7 while blast injury produced a significant increase only on Day 4. Furthermore, post-hoc comparisons revealed that area fractions were significantly different between injury cases on Days 1 and 4, but not on Day 7 (Figure 2.13). Both blunt and blast injuries led to comparable increases in the number density (Figure 2.14) but significantly lower values for the nearest neighbor distance on Days 1 through 7. In addition, post-hoc analysis revealed that the nearest neighbor distance was significantly different between injury cases on Day 1, but not on Days 4 or 7 (Figure 2.15). Similar trends were also observed in the nearest neighbor distance per volume (Figure 2.16).

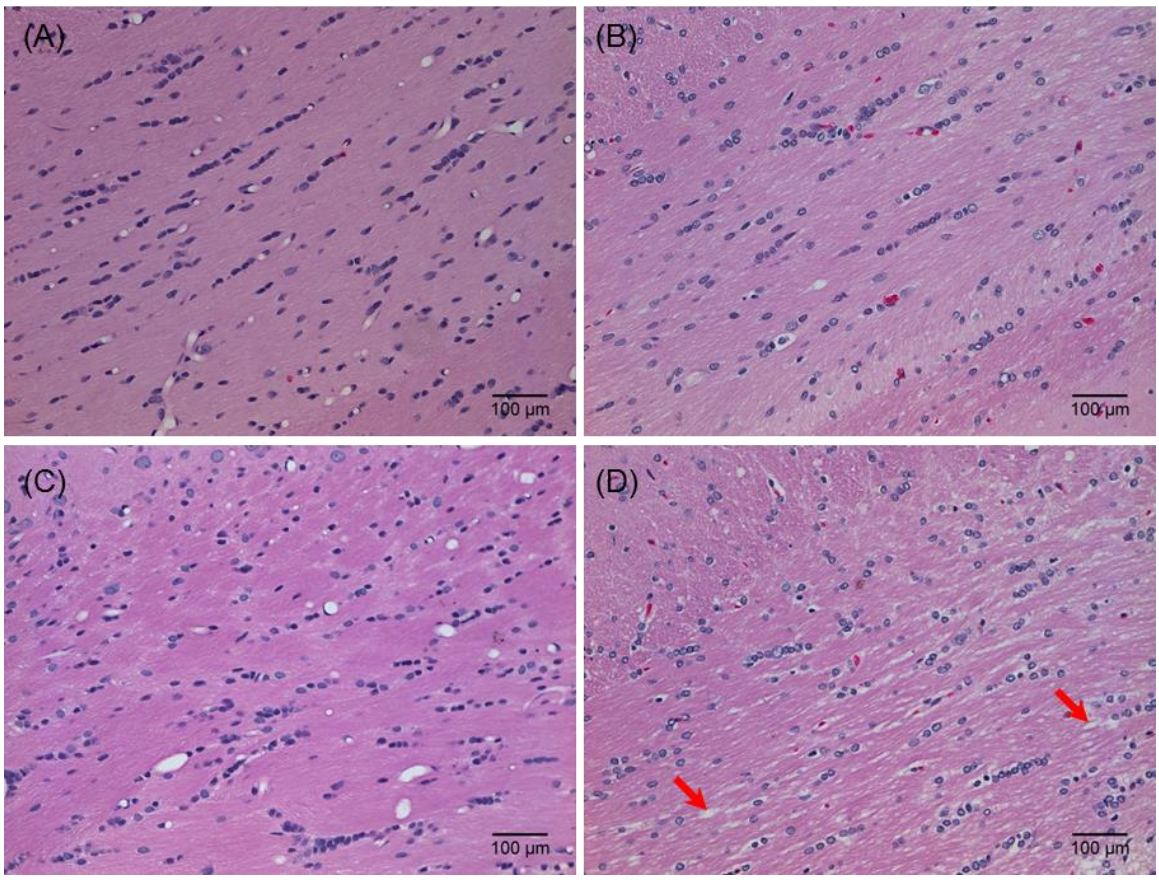

Figure 2.11 Representative H&E sections showing the variations in brain microstructure for the (A) control group and blunt trauma groups at (B) Day 1, (C) Day 4, and (D) Day 7.

Notes: Red arrows indicate voids detected by the GUI.

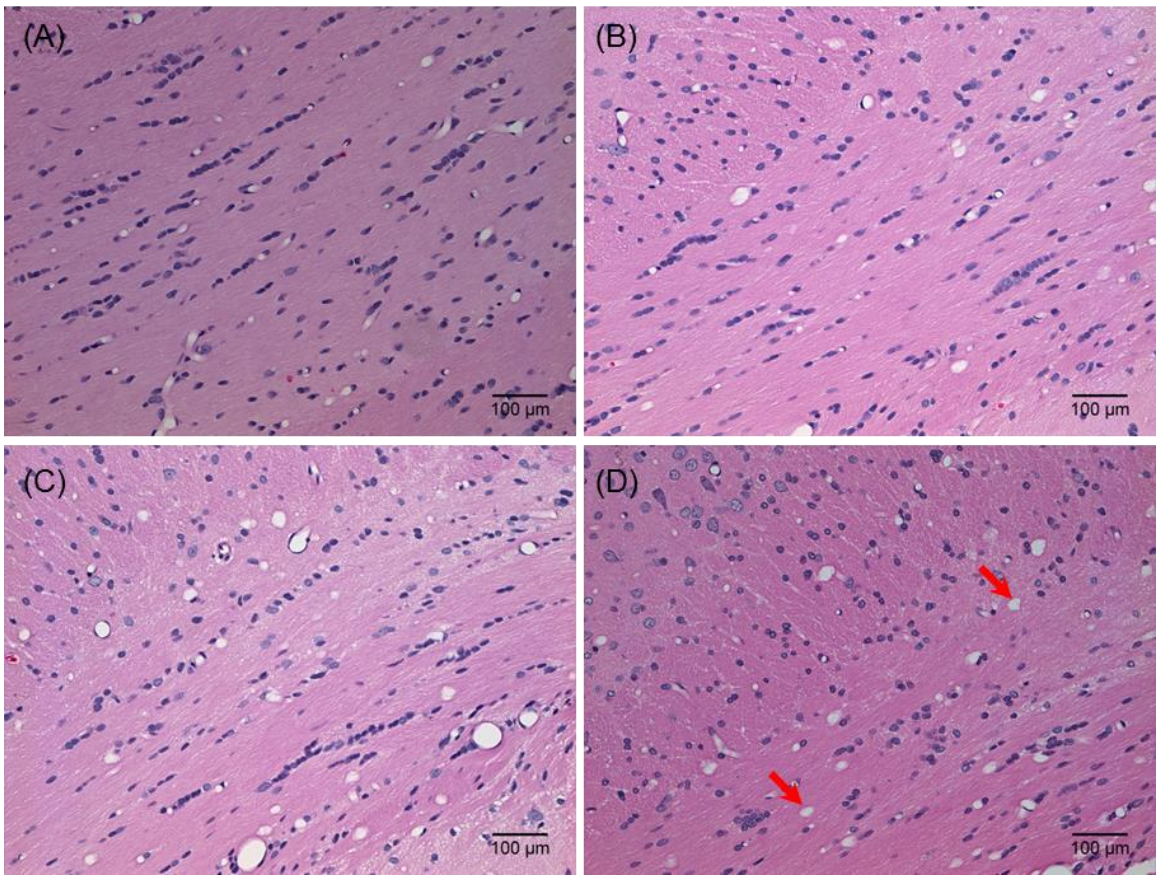

Figure 2.12 Representative H&E sections showing the variations in brain microstructure for the (A) control group and blast trauma groups at (B) Day 1, (C) Day 4, and (D) Day 7.

Notes: Red arrows indicate voids detected by the GUI.

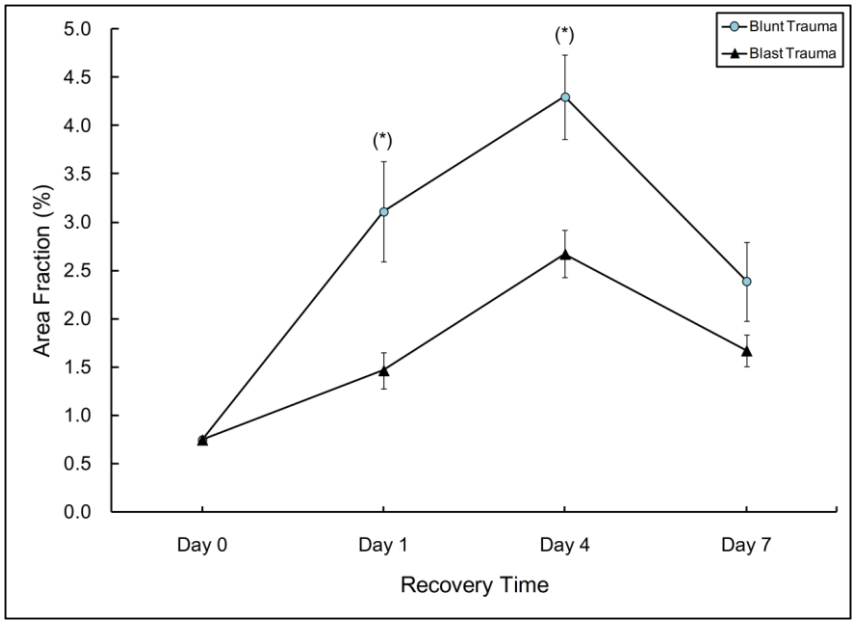

Figure 2.13 Comparison of area fractions (Mean ± SEM) between blunt and blast groups at recovery times of 1, 4, and 7 days.

Notes: The area fraction is the ratio of the total void area to the total image area. (*) denotes a significant difference between injury cases (p<0.05).

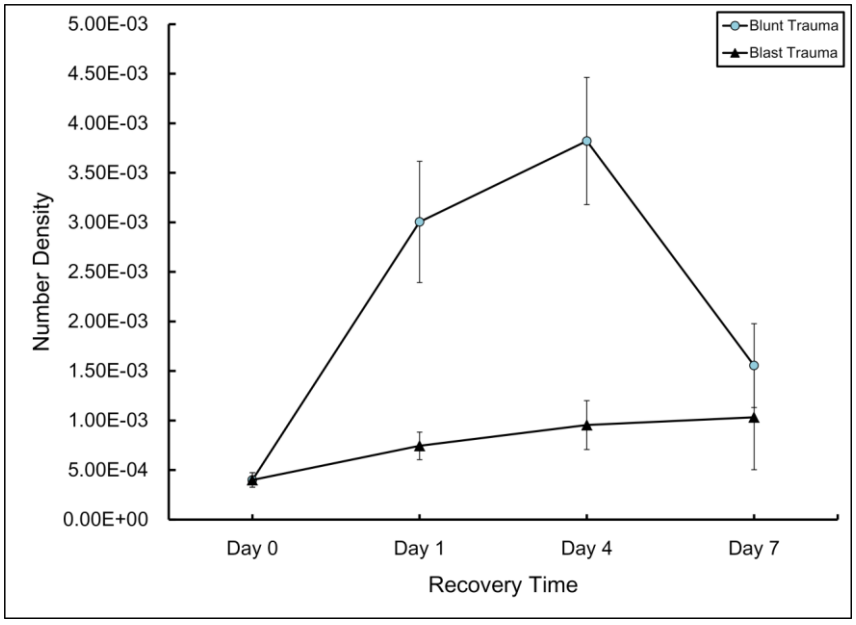

Figure 2.14 Comparison of number densities (Mean ± SEM) between blunt and blast groups at recovery times of 1, 4, and 7 days.

Notes: The number density is the total number of voids divided by the total image area.

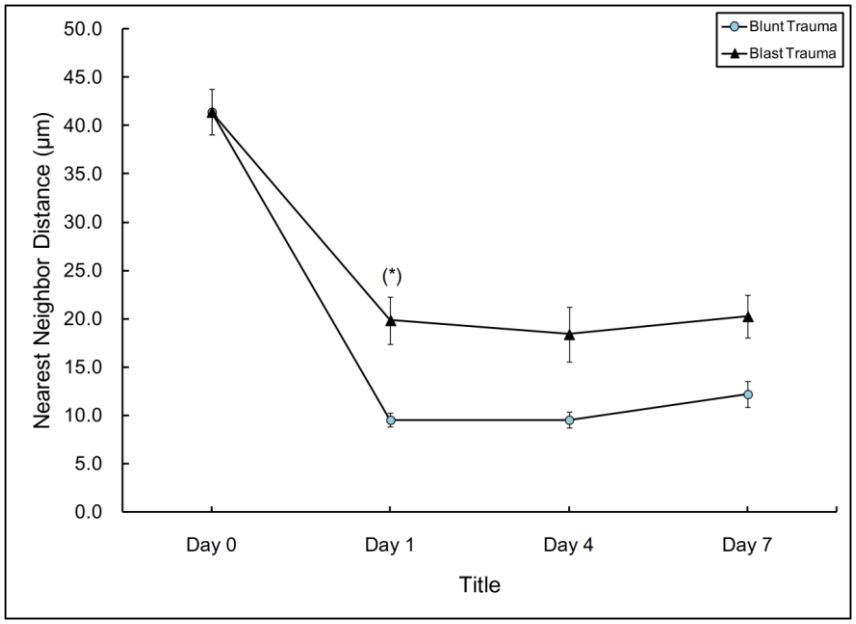

Figure 2.15 Comparison of nearest neighbor distance (Mean ± SEM) between blunt and blast groups at recovery times of 1, 4, and 7 days.

Notes: The nearest neighbor distance is the length of separation between the centroids of each void detected by the image analysis GUI. (*) denotes a significant difference between injury cases ($p<0.05$).

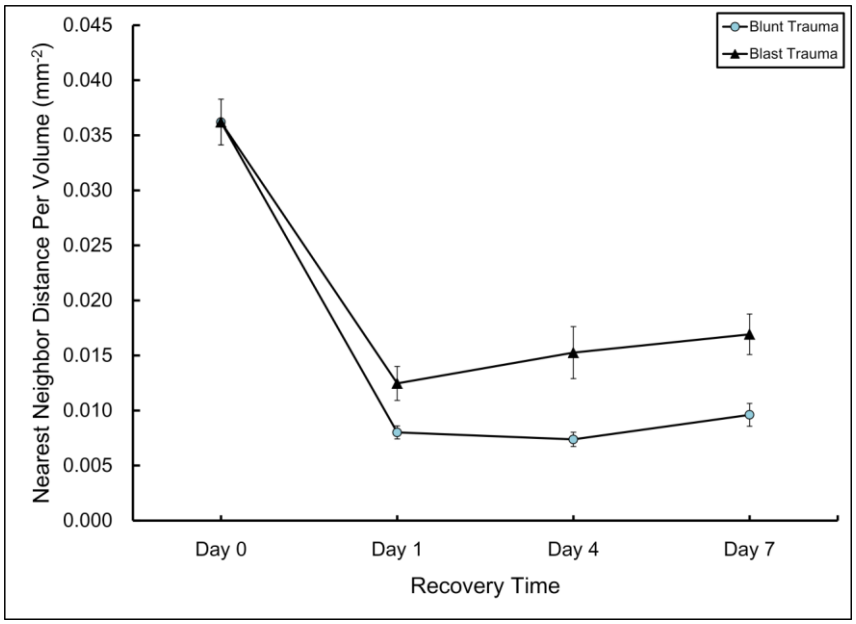

Figure 2.16 Comparison of nearest neighbor distance per volume (Mean ± SEM) between blunt and blast groups at recovery times of 1, 4, and 7 days.

Based on DTI and image analysis results, both injury led to physiological modifications in axonal microstructure. Significant changes in the fiber count, FA, area fraction, and nearest neighbor distance all provided evidence of altered axonal diffusion. These phenomena suggest that axonal impairment may occur differently based on the injury conditions applied.

2.4 Discussion and Conclusions

DTI results indicated that mild levels of blunt and blast possibly altered axonal diffusion (Figures 2.7-2.9). Damage to the axonal microstructure was expected since the corpus callosum is prone to injury regardless of the biomechanical factors involved (Ling et al., 2012). Both blunt and blast injuries most likely produced biochemical alterations that led to disrupted axonal transport and water diffusion, which resulted in significantly lower fiber (Figure 2.7). Although the fiber count significantly decreased, there were no significant changes in the fiber length (Figure 2.9). This finding could be explained by an increased permeability of the axonal membrane, which would divert water diffusion in a direction perpendicular to the primary fiber orientation. This phenomenon occurs during mild trauma because the axonal membrane becomes more porous, thus increasing water diffusion from the intracellular compartments of impaired axons to the extracellular matrix (MacDonald et al., 2007; Budde et al., 2008).

Blunt trauma produced lower FA values on Days 1, 4, and 7 compared to controls (Figure 2.10), which may correspond to an early onset of diffuse axonal injury (DAI). Blunt trauma often leads to DAI, which involves white matter damage characterized by disrupted axonal transport, axonal swelling, and secondary axotomy (i.e. axonal detachment) (Johnson et al., 2013). Conversely, blast trauma produced higher FA values

on Days 4 and 7 compared to controls (Figure 2.10). Increased FA has been observed in other studies of mTBI with researchers attributing this phenomenon to edema (Bazarian et al., 2007; Chu et al., 2010; Mayer et al., 2010; Henry et al., 2011). Researchers have also suggested that FA increases may be linked to neuroplasticity or a reparative response to mTBI (Lipton et al., 2009). In a recent DTI study on 17 patients examined one year after suffering mTBI, investigators discovered higher FA readings in the mTBI patients compared to 40 controls. Researchers subsequently determined that higher FA may be a suitable predictor for not only a decrease in post-concussion symptoms, but also an improved health-related quality of life (HRQoL) (Rosenbaum et al., 2012). Another possible mechanism for increased FA could be that blast injury disrupted biochemical processes (e.g. failure of ion pumps), which would lead to increased water retention that would be evidenced by cellular swelling. Since the underlying causes of increased FA are not yet completely understood, more DTI-based research is needed to further investigate this phenomenon and its correlation with mTBI. Based on the observed changes in this study's DTI measures, we believe that mild levels of blast trauma and blunt trauma were sufficient to elicit distinctive effects on the diffusion properties of the axonal fibers in the corpus callosum.

Previous studies have captured the microstructural history effects in alloys during deformation (Horstemeyer et al., 2000), and similar approaches have been applied to soft biological tissues toward the development of biofidelic constitutive models for finite element (FE) simulations (Begonia et al., 2010; Prabhu et al., 2011; Weed et al., 2012). Variations in brain microstructure were captured through image analysis parameters including area fraction and nearest neighbor distance. In comparisons between healthy

and injured brain tissue, statistically significant changes in these parameters correlated with the development of voids in the extracellular matrix.

Higher area fractions corresponded to an increased number of voids that formed due to fluid accumulation, which often occurs in white matter since it possesses more extracellular space than gray matter. Blunt and blast trauma most likely impaired axon physiology (e.g. increased membrane permeability, delamination of myelin sheath), subsequently causing progressive water diffusion toward the extracellular matrix (Vandevelde et al., 2012). In addition, blunt trauma produced higher area fractions than blast trauma on Days 1 through 7 (Fig. 12), which may be further linked to either primary or secondary injury. Immediate mechanical damage (i.e. primary injury) may be more dominant in blunt trauma since tearing or shearing of axonal fibers would cause more fluid to leak directly into extracellular space, thus producing a higher area fraction and a subsequently lower FA compared to controls. Conversely, delayed damage (i.e. secondary injury) may be more dominant in blast trauma since axonal fibers could possibly remain more structurally intact despite experiencing disrupted biochemical processes (Johnson et al., 2013). As a result, less fluid would diffuse into the extracellular matrix, which would explain the lower area fraction and higher FA. Decreases in nearest neighbor distance were also observed after blunt and blast trauma, and they corresponded to an increased frequency of voids. This trend was expected since it coincided with lower fluid retention in axonal fibers that were in an injured state. Based on image analysis findings, mild levels of blunt and blast subsequently diverted water diffusion from the axonal fibers to the extracellular space in white matter.

Other experimental models of TBI such as fluid percussion injury and controlled cortical impact recreate unrealistic biomechanical conditions (O'Connor et al., 2011) while others (e.g. weight drop model) generate high mortality rates (Marmarou et al., 1994) and are thus not well-suited for studying mTBI. Although the FA is one of the most commonly used DTI measures, a universally standard value has not currently been established as a predictor for injury (Chanraud et al., 2010; Zhu et al., 2011). Furthermore, direct comparison of FA among studies is challenging due to the variability in scanning parameters including magnet strength, scan time, spatial resolution, and signal-to-noise ratio (Van De Looij et al., 2011). For this study, we induced mild blunt and blast injuries in a reproducible manner to recreate conditions consistent with mTBI. We also determined the FA in a control group to establish a baseline for comparison with various injury groups. Additional DTI measures were not utilized, but their correlations to FA have been documented previously. Mean diffusivity (MD) is another common DTI measure that is inversely proportional to FA. Highly anisotropic diffusion within fiber tracts leads to a lower MD and subsequently produces a higher FA (McAllister et al., 2012).

Our study shows that mild levels of blunt and blast trauma can produce defects in the brain microstructure. We employed an analytical approach that coupled DTI with image analysis in order to quantify these microstructural alterations. Reductions in the fiber count, object area, and nearest neighbor distance were expected. However, a consistent fiber length and differential changes in FA were not anticipated and could have been influenced by biochemical processes that were disrupted under injurious conditions. Future studies could employ similar testing protocols but also include amyloid precursor

protein (APP) immunohistochemistry to further distinguish axonal pathology from edema. Information from this study can lead to improved mTBI diagnoses, targeted drug therapies, and a multiscale brain model that accounts for loading history effects (e.g. fatigue).

2.5 References

Appelboom, G., J. Han, S. Bruce, C. Szpalski, and E.S. Connolly (2012). "Clinical Relevance of Blast-Related Traumatic Brain Injury." *Acta Neurochirurgica* 154: 131-134.

Arfanakis, K., V.M. Haughton, J.D. Carew, B.P. Rogers, R.J. Dempsey, and M.E. Meyerand (2002). "Diffusion Tensor MR Imaging in Diffuse Axonal Injury." *American Journal of Neuroradiology* 23: 794–802.

Barkhoudarian, G., D.A. Hovda, and C.C. Giza (2011). "The Molecular Pathophysiology of Concussive Brain Injury." *Clinics in Sports Medicine* 30(1): 33-48.

Basser, P.J., S. Pajevic, C. Pierpaoli, J. Duda, and A. Aldroubi (2000). "In Vivo Fiber Tractography Using DT-MRI Data." *Magnetic Resonance in Medicine* 44: 625-632.

Bazarian, J.J., J. Zhong, B. Blyth, T. Zhu, V. Kavcic, and D. Peterson (2007). "Diffusion Tensor Imaging Detects Clinically Important Axonal Damage after Mild Traumatic Brain Injury: A Pilot Study." *Journal of Neurotrauma* 24(9): 1447-1459.

Begonia, M.T., R. Prabhu, J. Liao, M.F. Horstemeyer, and L.N. Williams (2010). "The Influence of Strain Rate Dependency on the Structure-Property Relations of Porcine Brain." *Annals of Biomedical Engineering* 38(10): 3043-3057.

Belanger, H.G., T. Kretzmer, R.D. Vanderploeg, and L.M. French (2010). "Symptom Complaints Following Combat-Related Traumatic Brain Injury: Relationship to Traumatic Brain Injury Severity and Posttraumatic Stress Disorder." *Journal of the International Neuropsychological Society* 16: 194-199.

Belanger, H.G., T. Kretzmer, R. Yoash-Gantz, T. Pickett, and L.A. Tupler (2009). "Cognitive Sequelae of Blast-Related Versus Other Mechanisms of Brain Trauma." *Journal of the International Neuropsychological Society* 15(1): 1-8.

Bigler, E.D. (2012). "Mild Traumatic Brain Injury: The Elusive Timing of "Recovery"." *Neuroscience Letters* 509, 1-4.

Bigler, E.D. and W.L. Maxwell (2012). "Understanding Mild Traumatic Brain Injury: Neuropatholgy and Neuroimaging." *PTSD and Mild Traumatic Brain Injury*. (Eds.) J. Vasterling, R. Bryant, and T. Keane. New York: Guilford Press.

Bryant, R., M. O'Donnell, and M. Creamer (2010). "The Psychiatric Sequelae of Traumatic Injury." *American Journal of Psychiatry* 167: 312-320.

Budde, M.D., L. Janes, E. Gold, L.C. Turtzo, and J.A. Frank (2011). "The Contribution of Gliosis to Diffusion Tensor Anisotropy and Tractography Following Traumatic Brain Injury: Validation in the Rat Using Fourier Analysis of Stained Tissue Sections." *Brain* 134: 2248-2260.

Budde, M.D., J.H. Kim, H.F. Liang, J.H. Russell, A.H. Cross, and S.K. Song (2008). "Axonal Injury Detected by In Vivo Diffusion Tensor Imaging Correlates with Neurological Disability in a Mouse Model of Multiple Sclerosis." *NMR in Biomedicine* 21: 589-597.

Carlson, K.F., S.M. Kehle, L.A. Meis, N. Greer, R. MacDonald, I. Rutks, N.A. Sayer, S.K. Dobscha, and T.J. Wilt (2011). "Prevalence, Assessment, and Treatment of Mild Traumatic Brain Injury and Posttraumatic Stress Disorder: A Systematic Review of the Evidence." *Journal of Head Trauma Rehabilitation* 26(2): 103-115.

Carlson, K.F., D. Nelson, R.J. Orazem, S. Nugent, D.X. Cifu, and N.A. Sayer (2010). "Psychiatric Diagnoses Among Iraq and Afghanistan War Veterans Screened for Deployment-Related Traumatic Brain Injury." *Journal of Traumatic Stress* 23: 17-24.

Cernak, I. and L.J. Noble-Haeusslein (2010). "Traumatic Brain Injury: An Overview of Pathobiology with Emphasis on Military Populations." *Journal of Cerebral Blood Flow & Metabolism* 30, 255-266.

Chanraud, S., N. Zahr, E.V. Sullivan, and A. Pfefferbaum (2010). "MR Diffusion Tensor Imaging: A Window into White Matter Integrity of the Working Brain." *Neuropsychology Review* 20, 209-225.

Chu, Z., E.A. Wilde, J.V. Hunter, S.R. McCauley, E.D. Bigler, M. Troyanskaya, R. Yallampali, J.M. Chia, and H.S. Levin (2010). "Voxel-Based Analysis of Diffusion Tensor Imaging in Mild Traumatic Brain Injury in Adolescents." *American Journal of Neuroradiology* 31: 340-346.

Correia, S., S.Y. Lee, T. Voorn, D.F. Tate, R.H. Paul, S. Zhang, S.P. Salloway, P.F. Malloy, and D.H. Laidlaw (2008). "Quantitative Tractography Metrics of White Matter Integrity in Diffusion-Tensor MRI." *NeuroImage* 42: 568-581.

Ducreaux, D., P. Fillard, D. Facon, A. Ozanne, J.F. Lepeintre, J. Renoux, M. Tadie, and P. Lasjaunias (2007). "Diffusion Tensor Magnetic Resonance Imaging and Fiber Tracking in Spinal Cord Lesions." *Neuroimaging Clinics of North America* 17(1): 137-147.

Elder, G.A. and A. Cristian (2009). "Blast-Related Mild Traumatic Brain Injury: Mechanisms of Injury and Impact on Clinical Care." *Mount Sinai Journal of Medicine* 76: 111-118.

Faul, M., L. Xu, M.M. Wald, and V.G. Coronado (2010). Traumatic Brain Injury in the United States: Emergency Department Visits, Hospitalizations, and Deaths. Centers for Disease Control and Prevention; National Center for Injury Prevention and Control. Atlanta, GA.

Finkelstein, E., P. Corso, T. Miller, I. Fiebelkorn, and E. Zaloshnja (2006). "The Incidence and Economic Burden of Injuries in the United States." *Injury Prevention* 12, 212-218. DOI: 10.1136/ip.2005.010983.

Heemskerk, A.M., G.J. Strijkers, M.R. Drost, G.S. Van Bochove, and K. Nicolay (2007). "Skeletal Muscle Degeneration and Regeneration After Femoral Artery Ligation in Mice: Monitoring with Diffusion MR Imaging." *Radiology* 243(2): 413-421.

Henry, L.C., J. Tremblay, S. Tremblay, A. Lee, C. Brun, N. Lepore, H. Theoret, D. Ellemberg, and M. Lassonde (2011). "Acute and Chronic Changes in Diffusivity Measures after Sports Concussion." *Journal of Neurotrauma* 28(10): 2049-2059.

Hicks, R.R., S.J. Fertig, R.E. Desrocher, W.J. Koroshetz, and J.J. Pancrazio (2010). "Neurological Effects of Blast Injury." *Journal of Trauma and Acute Care Surgery* 68(5): 1257-1263.

Hoge, C.W., D. McGurk, J.L. Thomas, A.L. Cox, C.C. Engel, and C.A. Castro (2008). "Mild Traumatic Brain Injury in U.S. Soldiers Returning from Iraq." *New England Journal of Medicine* 358: 453-463.

Horstemeyer, M.F., J. Lathrop, A.M. Gokhale, and M. Dighe (2000). "Modeling Stress State Dependent Damage Evolution in a Cast Al-Si-Mg Aluminum Alloy." *Theoretical and Applied Fracture Mechanics* 33: 31-47.

Huisman, T., L.H. Schwamm, P.W. Schaefer, W.J. Koroshetz, N. Shetty-Alva, Y. Ozsunar, O. Wu, and A.G. Sorensen (2004). "Diffusion Tensor Imaging as Potential Biomarker of White Matter Injury in Diffuse Axonal Injury." *American Journal of Neuroradiology* 25: 370-376.

Johnson, V.E., W. Stewart, and D.H. Smith (2013). "Axonal Pathology in Traumatic Brain Injury." *Experimental Neurology* 246: 35-43.

Lansdown, D.A., Z. Ding, M. Wadington, J.L. Hornberger, and B.M. Damon (2007). "Quantitative Diffusion Tensor MRI-Based Fiber Tracking of Human Skeletal Muscle." *Journal of Applied Physiology* 103(2): 673-681.

Levin, H.S., E. Wilde, M. Troyanskaya, N.J. Peterson, R. Scheibel, M. Newsome, M. Radaideh, T. Wu, R. Yallampalli, Z. Chu, and X. Li (2010). "Diffusion Tensor Imaging of Mild to Moderate Blast-Related Traumatic Brain Injury and Its Sequelae." *Journal of Neurotrauma* 27(4): 683-694.

Li, J., X. Li, D. Feng, and L. Gu (2011). "Quantitative Evaluation of Microscopic Injury with Diffusion Tensor Imagin in a Rat Model of Diffuse Axonal Injury." *European Journal of Neuroscience* 33: 933-945.

Ling, G., F. Bandak, R. Armonda, G. Grant, and J. Ecklund (2009). "Explosive Blast Neurotrauma." *Journal of Neurotrauma* 26: 815-825.

Ling, J.M., A. Pena, R.A. Yeo, F.L. Merideth, S. Klimaj, C. Gasparovic, and A.R. Mayer (2012). "Biomarkers of Increased Diffusion Anisotropy in Semi-Acute Mild Traumatic Brain Injury: A Longitudinal Perspective." *Brain* 135: 1281-1292.

Lipton, M.L., E. Gulko, M.E. Zimmerman, B.W. Friedman, M. Kim, E. Gellella, T. Gold, K. Shifteh, B.A. Ardekani, and C.A. Branch (2009). "Diffusion Tensor Imaging Implicates Prefrontal Axonal Injury in Executive Function Impairment Following Very Mild Traumatic Brain Injury." *Radiology* 252(3): 816-824.

MacDonald, C.L., K. Dikranian, P. Bayly, D. Holtzman, and D. Brody (2007). "Diffusion Tensor Imaging Reliably Detects Experimental Traumatic Axonal Injury and Indicates Approximate Time of Injury." *Journal of Neuroscience* 27: 11869-11876.

MacDonald, C.L., K. Dikranian, S.K. Song, P.V. Bayly, D.M. Holtzman, and D.L. Brody (2007). "Detection of Traumatic Axonal Injury with Diffusion Tensor Imaging in a Mouse Model of Traumatic Brain Injury." *Experimental Neurology* 205: 116-131.

MacGregor, A.J., A.L. Dougherty, R.H. Morrison, K.H. Quinn, and M.R. Galarneau (2011). "Repeated Concussion Among U.S. Military Personnel During Operation Iraqi Freedom." *Journal of Rehabilitation Research & Development* 48(10): 1269-1278.

Margulies, S. and R. Hicks (2009). "Combination Therapies for Traumatic Brain Injury: Prospective Considerations." *Journal of Neurotrauma* 26, 925-939.

Marmarou, A., M.A. Foda, W. van den Brink, J. Campbell, H. Kita, and K. Demetriadou (1994). "A New Model of Diffuse Brain Injury in Rats - Part I: Pathophysiology and Biomechanics." *Journal of Neurosurgery* 80(2): 291-300.

Mayer, A.R., J. Ling, M.V. Mannell, C. Gasparovic, J.P. Phillips, D. Doezema, R. Reichard, and R.A. Yeo (2010). "A Prospective Diffusion Tensor Imaging Study in Mild Traumatic Brain Injury." 74, 643-650.

McAllister, T.W., J.C. Ford, S. Ji, J.G. Beckwith, L.A. Flashman, K. Paulsen, and R.M. Greenwald (2012). "Maximum Principal Strain and Strain Rate Associated with Concussion Diagnosis Correlates with Changes in Corpus Callosum White Matter Indices." *Annals of Biomedical Engineering* 40(1): 127-140.

McCrory, P., W. Meeuwisse, K. Johnston, J. Dvorak, M. Aubry, M. Molloy, and R. Cantu (2009). "Consensus Statement on Concussion in Sport – The 3rd International Conference on Concussion in Sport held in Zurich, November 2008." *Journal of Clinical Neuroscience* 16(6): 755-763.

O'Connor, W.T., A. Smyth, and M.D. Gilchrist (2011). "Animal Models of Traumatic Brain Injury: A Critical Evaluation." *Pharmacology & Therapeutics* 130: 106-113.

Okie, S. (2005). "Traumatic Brain Injury in the War Zone." *New England Journal of Medicine* 352(20): 2043-2047.

Ozanne, A., T. Krings, D. Facon, P. Fillard, J.L. Dumas, H. Alvarez, D. Ducreaux, and P. Lasjaunias (2007). "MR Diffusion Tensor Imaging and Fiber Tracking in Spinal Cord Arteriovenous Malformations: A Preliminary Study." *American Journal of Neuroradiology* 28(7): 1271-1279.

Prabhu, R., M.F. Horstemeyer, M.T. Tucker, E.B. Marin, J.L. Bouvard, J.A. Sherburn, J. Liao, and L.N. Williams (2011). "Coupled Experiment/Finite Element Analysis on the Mechanical Response of Porcine Brain under High Strain Rates." *Journal of the Mechanical Behavior of Biomedical Materials* 4: 1067-1080.

Schneiderman, A., E. Braver, and H. Kang (2008). "Understanding Sequelae of Injury Mechanisms and Mild Traumatic Brain Injury Incurred During the Conflicts in Iraq and Afghanistan: Persistent Postconcussive Symptoms and Post-Traumatic Stress Disorder." *American Journal of Epidemiology* 167: 1446-1452.

Shenton, M.E., H.M. Hamoda, J.S. Schneiderman, S. Bouix, O. Pasternak, Y. Rathi, M.A. Vu, M.P. Purohit, K. Helmer, I. Koerte, A.P. Lin, C.F. Westing, R. Kikinis, M. Kubicki, R.A. Stern, and R. Zafonte (2012). "A Review of Magnetic Resonance Imaging and Diffusion Tensor Imaging Findings in Mild Traumatic Brain Injury." *Brain Imaging and Behavior* 6: 137-192.

Sundgren, P.C., Q. Dong, D. Gomez-Hassan, S.K. Mukherji, P. Maly, and R. Welsh (2004). "Diffusion Tensor Imaging of the Brain: Review of Clinical Applications." *Neuroradiology* 46: 339-350.

Tate, D.F., J. Conley, R.H. Paul, K. Coop, S. Zhang, W. Zhou, D.H. Laidlaw, L.E. Taylor, T. Flanigan, B. Navia, R. Cohen, and K. Tashima (2010). "Quantitative Diffusion Tensor Imaging Tractography Metrics are Associated with Cognitive Performance Among HIV-Infected Patients." *Brain Imaging and Behavior* 4: 68-79.

Van De Looij, Y., F. Mauconduit, M. Beaumont, S. Valable, R. Farion, G. Francony, J. Payen, and H. Lahrech (2011). "Diffusion Tensor Imaging of Diffuse Axonal Injury in a Rat Brain Trauma Model." *NMR in Biomedicine* 25: 93-103.

Vandevelde, M., R.J. Higgins, and A. Oevermann (2012). *Veterinary Neuropathology: Essentials of Theory and Practice*. Ames, IA, John Wiley & Sons, Ltd.

Weed, B.C., A. Borazjani, S.S. Patnaik, R. Prabhu, M.F. Horstemeyer, P.L. Ryan, T. Franz, L.N. Williams, and J. Liao (2012). "Stress State and Strain Rate Dependence of the Human Placenta." *Annals of Biomedical Engineering* 40(10): 2255-2265.

Wu, E.X., Y. Wu, H. Tang, J. Wang, J. Yang, M.C. Ng, E.S. Yang, C.W. Chan, S. Zhu, C.P. Lau, and H.F. Tse (2007). "Study of Myocardial Fiber Pathway Using Magnetic Resonance Diffusion Tensor Imaging." *Magnetic Resonance Imaging* 25(7): 1048-1057.

Zhang, J., M. Aggarwal, and S. Mori (2012). "Structural Insights into the Rodent CNS Via Diffusion Tensor Imaging." *Trends in Neuroscience* 35, 412-421.

Zhang, S., J.A. Crow, X. Yang, J. Chen, A. Borazjani, K.B. Mullins, W. Chen, R.C. Cooper, R.M. McLaughlin, and J. Liao (2010). "The Correlation of 3D DT-MRI Fiber Disruption with Structural and Mechanical Degeneration in Porcine Myocardium." *Annals of Biomedical Engineering* 38(10): 3084-3095.

Zhang, S., C. Demiralp, and D.H. Laidlaw (2003). "Visualizing Diffusion Tensor MR Images Using Streamtubes and Streamsurfaces." *IEEE Transactions on Visualization and Computer Graphics* 9(4): 454-462.

Zhang, S., G. Kindlmann, and G.H. Laidlaw (2004). "Diffusion Tensor MRI Visualization." *Visualization Handbook*. (Eds.) C.D. Hansen and C.R. Johnson. Oxford: Academic Press**,** 327-340.

Zhu, T., R. Hu, X. Qiu, M. Taylor, Y. Tso, C. Yiannoutsos, B. Navia, S. Mori, S. Ekholm, G. Schifitto, and J. Zhong (2011). "Quantification of Accuracy and Precision of Multi-Center DTI Measurements: A Diffusion Phantom and Human Brain Study." *NeuroImage* 56(3): 1398-1411.

CHAPTER III

DEVELOPMENT OF FINITE ELEMENT MODEL FOR SIMULATING MILD BLUNT AND BLAST TRAUMA

3.1 Introduction

When military personnel experience mTBI, they often return to full duty status immediately after clinical signs begin to disappear. However, returning prematurely can increase the risk for repeat injury and other long-term consequences (MacGregor et al., 2011). Physicians often face challenges in diagnosing mTBI because the clinical signs can be physical, behavioral, cognitive, or emotional (McCrory et al., 2009). Previous studies have also shown that mTBI patients exhibit symptoms that are similar to those found in post-traumatic stress disorder (PTSD) (Hoge et al., 2008; Carlson et al., 2010; Levin et al., 2010; Carlson et al., 2011) and post-concussive syndrome (PCS) (Schneiderman et al., 2008; Belanger et al., 2010; Bryant et al., 2010). Some patients suffering from mTBI will endure deteriorating brain function while other individuals experience full mental recovery. Understanding the mechanisms of these unpredictable patient outcomes poses a major challenge for researchers but also has significant clinical implications (Budde et al., 2011). One potential benefit of this knowledge is that physicians can more accurately diagnose patients with symptoms common to both mTBI and PTSD. Another advantage is that pharmaceutical companies can utilize this information to develop more effective drug treatments, which could directly alleviate

specific secondary injury cascades that would otherwise exacerbate the overall injury progression.

Researchers have not reached a full consensus on how blunt trauma and blast trauma contribute to the progression of mTBI, respectively. This research is needed because soldiers often experience blast trauma from IED pressure waves as well as blunt trauma from ensuing head impacts. A review on animal models of close-head injuries (i.e. blunt trauma) revealed that the early pathological features observed were also found in models of blast injury (Margulies and Hicks, 2009). Some researchers argue that blast trauma produces temporal, spatial, and recurrent pathological changes, which are different from those generated by blunt trauma (Ling et al., 2009). Other investigators insist that there is insufficient evidence to support this claim and subsequently believe that similar cognitive impairments are found in both injury cases (Belanger et al., 2009). Because the distinctions between blunt and blast trauma remain unclear under mTBI conditions (Elder and Cristian, 2009; Cernak and Noble-Haeusslein, 2010; Hicks et al., 2010), further study is necessary to identify the underlying mechanisms specific to each injury scenario. Although traditional histological techniques are effective, they can be invasive for the study of mTBI. Furthermore, standard neuroimaging methods such as magnetic resonance imaging (MRI) and X-ray computerized (CT) often cannot detect anomalies within this lower regime of injury. Finite element (FE) simulations provide researchers with a noninvasive computational tool that can identify the differential mechanical responses of the brain when subjected to blunt and blast trauma, respectively.

In the current study, Sprague-Dawley rats were exposed to mild levels of either blunt or blast trauma, and experimental conditions were simulated using

ABAQUS/Explicit 6.10 (Simulia, 2010). Two pressure profiles were incorporated into FE simulations of blast trauma with the first profile corresponding to experimental results and the second profile having a cumulative impulse that was equivalent to the cumulative impulse measured from blunt trauma experiments. The head model comprised four regions that represented the scalp/muscle, skull, cerebrospinal fluid (CSF), and brain. The von Mises stress, pressure, and maximum principal strain were tracked at four locations, which include the skull, cerebral cortex, corpus callosum, and hypothalamus. Although various computational analyses have been employed to examine mTBI, this work aims to directly compare the differential mechanical responses in various brain regions and subsequently determine whether blunt or blast trauma event plays a more significant role in mTBI.

3.2 Methods

3.2.1 Experimental Setup

A total of 28 male Sprague-Dawley rats (300-325 g, Harlan Laboratories) were used in this study. Animals were housed in cages under a 12 hour dark/light cycle with access to food pellets and water *ad libitum* and were given 3-7 days to acclimate before testing. All procedures were approved by the Institutional Animal Care and Use Committee of Mississippi State University. Animals were assigned to three groups: controls, blunt trauma, and blast trauma. Prior to biomechanical testing, rats were anesthetized using dexmedetomidine (0.05-0.1 mg/kg, IP) and fentanyl (0.1 mg/kg, IP) followed by propofol (100 mg/kg, IP) once loss of righting reflex was observed. When rats were fully sedated (i.e. loss of toe pinch reflex), their bodies were secured onto a test stage with their heads positioned over SunMate® Soft polyurethane open-cell foam

(Dynamic Systems Inc., Leicester, North Carolina). A marker was placed halfway between the medial canthus of both eyes to identify the impact site and to facilitate the horizontal and vertical positioning of the test stage.

The experimental protocol discussed in Study 1 (i.e. Chapter II) was utilized for Study 2. Briefly, the experimental parameters for inducing blunt injury included an impact depth of 1 mm and an impact velocity of approximately 2.2 m/s. For blast injury, the tank pressure on the custom-built device was set to 689 kPa (100 psi) while the animals were positioned 2.5 cm (1 in.) away from the nozzle.

3.2.2 Head Geometry

Multiple pulse sequences were utilized during the scanning of healthy Sprague-Dawley rats (300-325 g, Harlan Laboratories). Due to its higher resolution, the DICOM image stack from the 3-D Fast Spoiled Gradient Recall (3-D FSPGR) pulse sequence was selected for segmentation in ScanIP (Simpleware Ltd, United Kingdom). The head geometry comprised four separate regions: (1) scalp/muscle, (2) skull, (3) cerebrospinal fluid (CSF), and (4) brain (Figure 3.1). The thresholding algorithm and recursive Gaussian filter were used for mask generation and smoothing, respectively. Although the original mask for the scalp/muscle included ears, they were removed to reduce the total number of elements and to ensure that simulated impacts occurred between the medial canthus of both eyes (Figure 3.2). Masks were subsequently converted to a mesh composed of both hexahedral (C3D8) and tetrahedral (C3D4) elements.

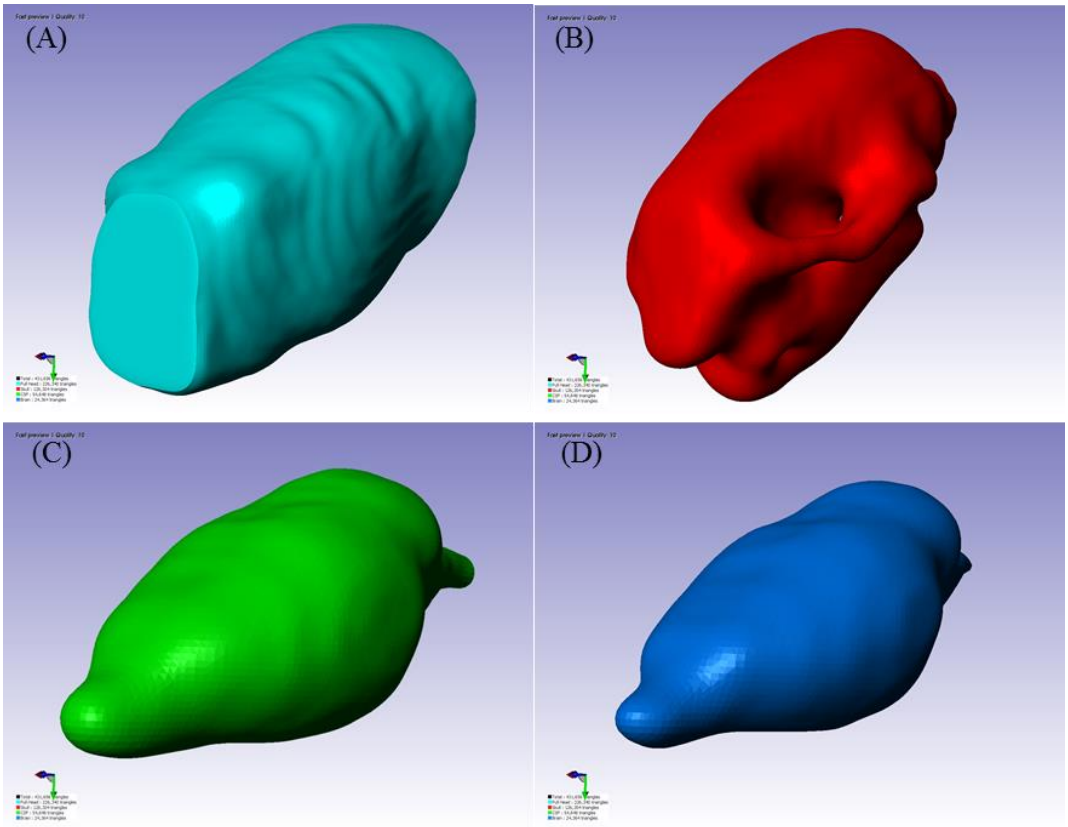

Figure 3.1 Isometric views of masks generated for the (A) scalp/muscle , (B) skull, (C) CSF, and (D) brain.

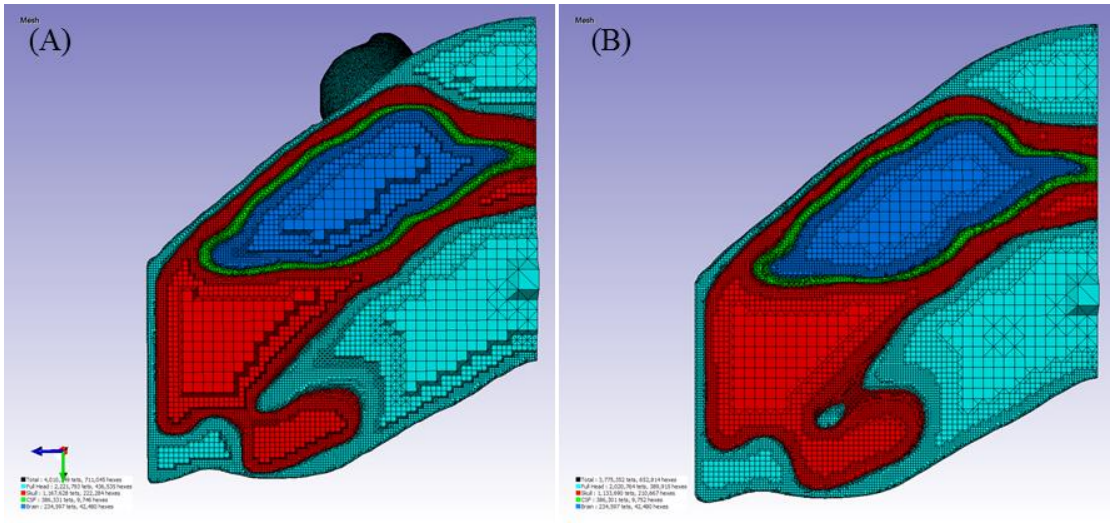

Figure 3.2 Mid-sagittal view of the (A) original head mesh and (B) modified head mesh with the ears excluded.

ScanIP is capable of generating contact pairs in order to characterize the surface interactions between masks. In addition, this option automatically produces contact surfaces in models imported into ABAQUS/Explicit 6.10 (Simulia, 2010), which facilitates the analysis of predefined element sets. The head mesh for simulating blunt trauma had four contact surfaces with three interactions defined: (1) scalp/muscle-skull, (2) skull-CSF, and (3) CSF-brain. The head mesh for simulating blast trauma required two additional features that were created in ScanIP. First, the head geometry was enclosed in a mask that represented the surrounding air (Figure 3.3). Second, a contact pair was created to depict the surface interaction between the masks corresponding to the scalp/muscle and the air. All meshes were imported into ABAQUS/Explicit 6.10 (Simulia, 2010) for further model development and finite element (FE) simulation.

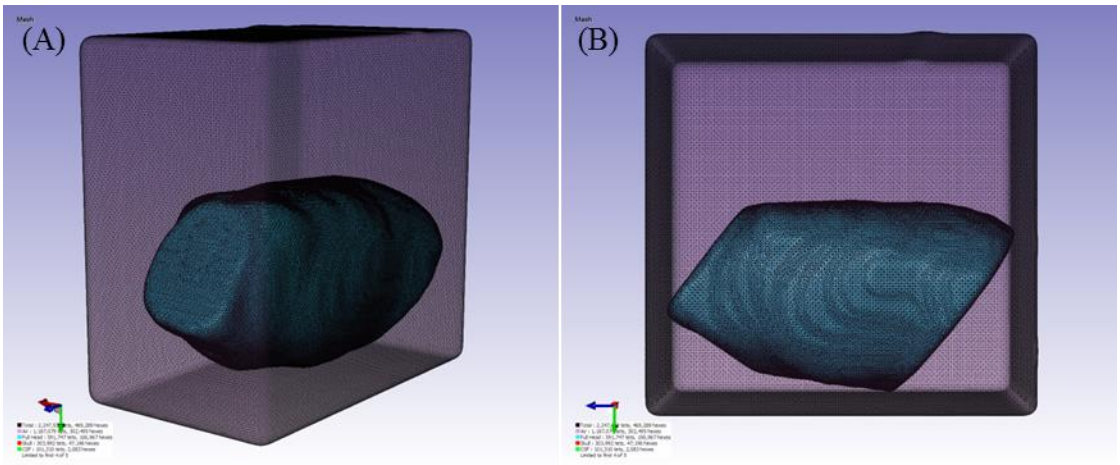

Figure 3.3 (A) Isometric view and (B) side view of the mesh used for simulating blast trauma, which shows the air (pink) in addition to the head mesh (cyan).

3.2.3 Material Properties

The scalp/muscle, skull, and CSF were assigned elastic material properties including density, Young's modulus, and Poisson's ratio (Table 3.1). The properties for the brain included the density and a user-defined material model that was developed using experimental data from high rate testing of brain tissue (Prabhu et al., 2011). This material model was originally derived to depict the mechanical behavior of polymers (Bouvard et al., 2010) but has been recently modified to characterize the brain. Furthermore, this model allows for implementation of internal state variables (ISVs) to capture the effects of the tissue microstructure and loading history (e.g. fatigue).

Table 3.1 Summary of elastic material properties assigned to each head region.

Head Region	Density (kg/m^3)	Young's Modulus (MPa)	Poisson's Ratio
Skin/Muscle	1200	16.7	0.15
Skull	2000	15000	0.22
CSF	1130	20	0.45
Brain	1040	N/A	N/A

3.2.4 Mesh Refinement Study

ScanIP initially produced a mesh totaling nearly 4.9 million elements because the original image resolution was 0.15 x 0.15 mm with a spacing of 0.5 mm. Due to computational limitations, however, this mesh was down-sampled various times in order to obtain meshes that were anatomically accurate but also computationally efficient. Table 3.2 summarizes the characteristics of three different mesh sizes selected for mesh refinement.

Table 3.2 Summary of mesh sizes selected for the mesh refinement study.

Mesh Number	Down-Sampling Factor	Hexahedral Elements	Tetrahedral Elements
#1	1.5	230k	1.9M
#2	2.0	100k	1.0M
#3	2.75	37k	485k

Each FE simulation in the mesh refinement study consisted of three parts: (1) head, (2) polyurethane foam, and (3) rigid circular impactor (Figure 3.4). The foam possessed elastic material properties such as the density, Young's modulus, and Poisson's ratio. In addition, the encastre boundary condition was applied to the bottom surface of the foam to restrict both translation and rotation. The circular impactor had the same diameter (2.54 cm) as the impactor used for blunt trauma experiments, and it did not require any material properties since it was generated as a rigid planar shell. Furthermore, the rigid impactor was assigned a predefined field that was equal to the loading velocity of 2.2 m/s. Tie constraints were also created to characterize the relative movements of nodes in neighboring contact surfaces. Three tie constraints were developed for the head model used in the mesh refinement study: (1) scalp/muscle-skull, (2) skull-CSF, and (3) CSF-brain. After FE simulations were performed for each mesh size, the resulting pressure distributions within the brain were compared.

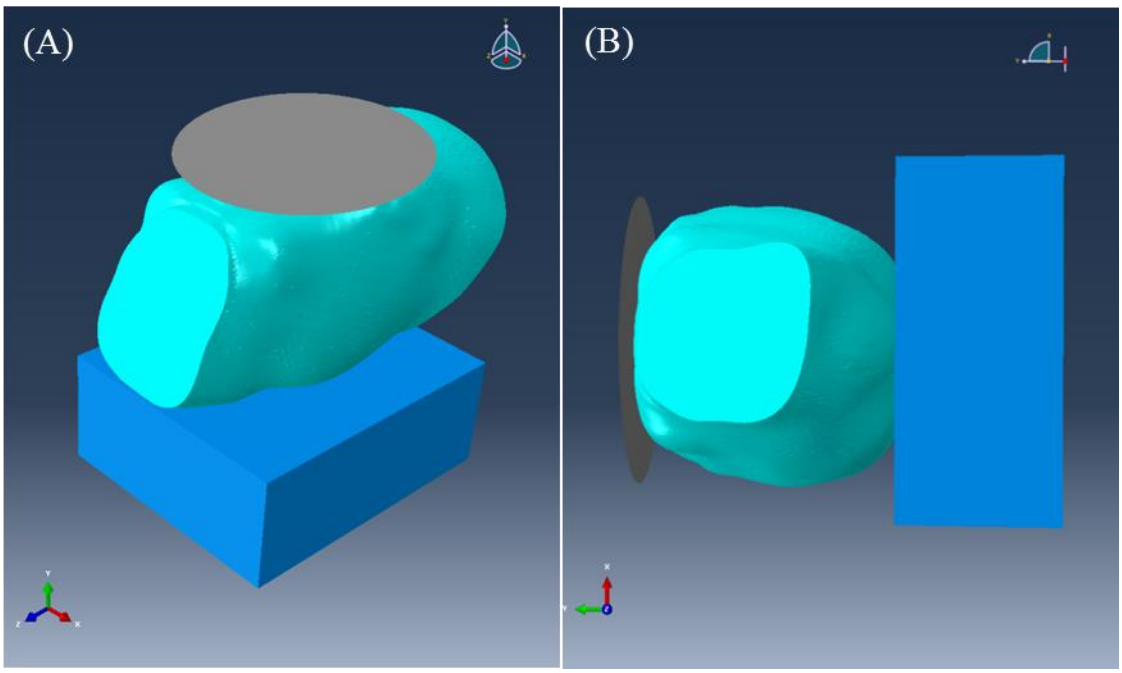

Figure 3.4 (A) Isometric view and (B) side view of the FE simulation setup for the mesh refinement study, which shows the rigid impactor (gray), head mesh (cyan), and foam (blue).

3.2.5 FE Simulations of Blunt Trauma

FE simulations of blunt trauma utilized a cylindrical impactor with dimensions identical to the actual impactor used in blunt trauma experiments (Figure 3.5). Various FE model features were identical to those used in the mesh refinement study (e.g. material properties, tie constraints, predefined velocity). However, the mass and elastic material properties for the cylindrical impactor were also assigned to allow for observation of the resulting pressure distribution through the impactor as well as the head. FE simulations of blunt trauma were performed using the coarse mesh (Mesh #3) and included field outputs such as von Mises stress, maximum principal strain, and pressure. FE results were examined at the impact site on the skull and three brain

locations, which included the cerebral cortex (i.e. *coup* site), corpus callosum, and hypothalamus (i.e. *countercoup* site) (Figure 3.6).

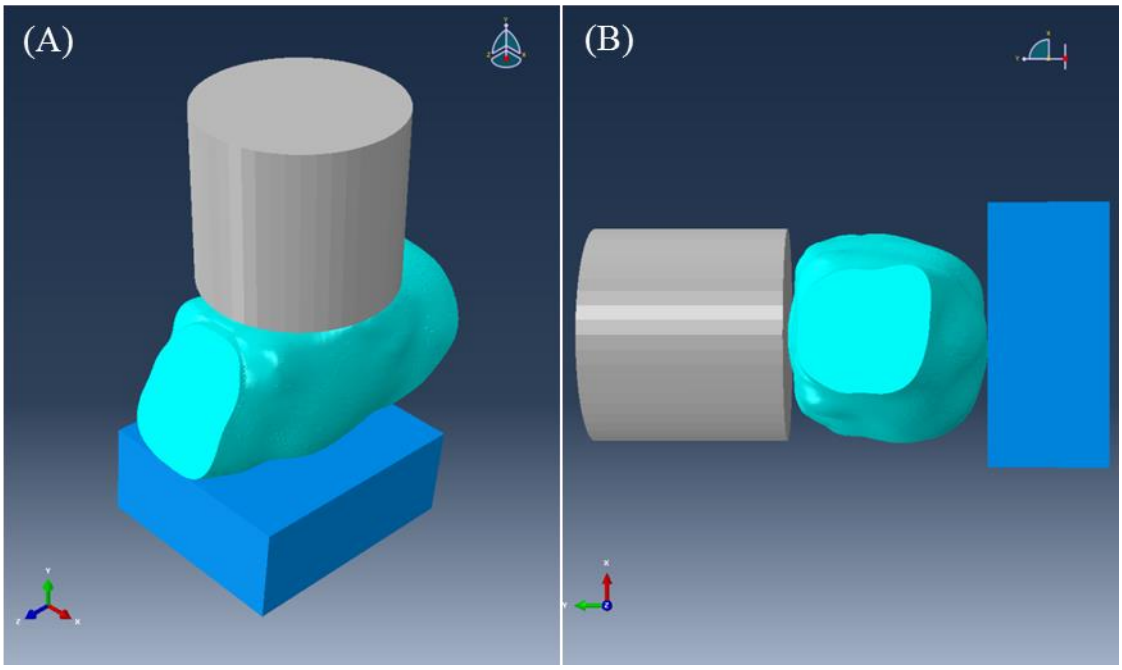

Figure 3.5 (A) Isometric view and (B) side view of the FE simulation setup for blunt trauma, which shows the cylindrical impactor (gray), head mesh (cyan), and foam (blue).

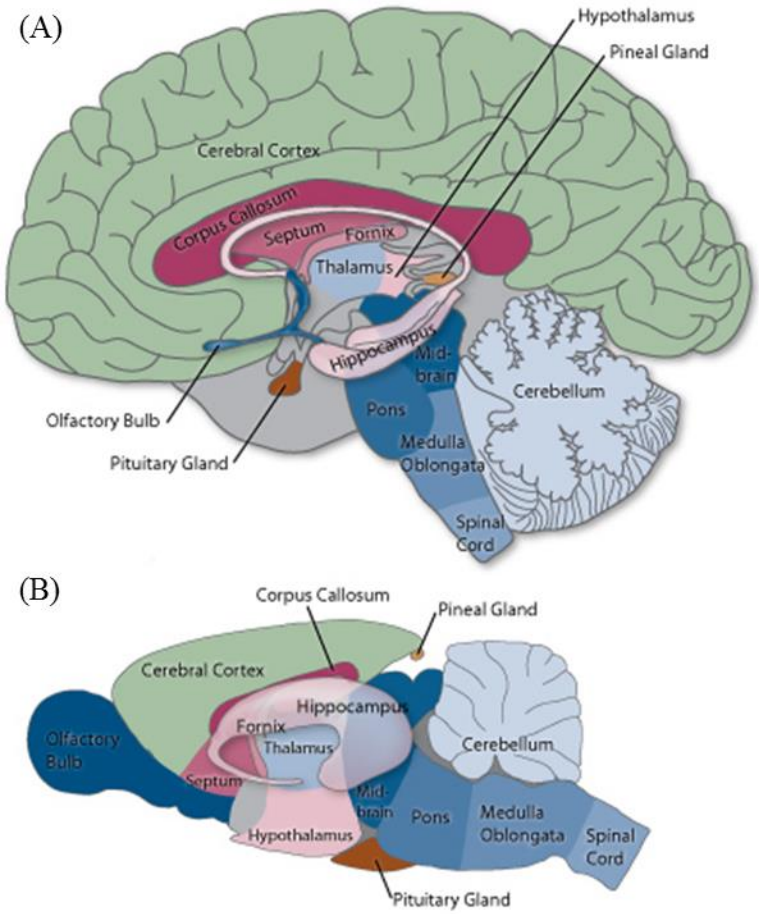

Figure 3.6 Mid-sagittal views of the (A) human brain compared to the (B) rodent brain.

Notes: FE simulation results focused on 4 regions that primarily included the skull, cerebral cortex, corpus callosum, and hypothalamus.
(Courtesy:http://learn.genetics.utah.edu/content/addiction/genetics/neurobiol.html)

3.2.6 FE simulations of Blast Trauma

FE simulations of blast trauma utilized the incident wave interaction property, which required several features to be defined. First, the locations of the source point and standoff point had to be specified. The source point was positioned centrally along the top surface of the air mesh while the standoff point was positioned approximately 2.54 cm directly below the source point on the outer surface of the scalp/muscle (Figure 3.7).

Second, properties for the air had to be assigned. These properties include the speed of sound through air (343 m/s) and density (1.2 kg/m^3). Elastic material properties such as Young's modulus and Poisson's ratio were also included. Another feature that needed to be defined was the amplitude, which corresponded to the pressure profile obtained from blast trauma experiments.

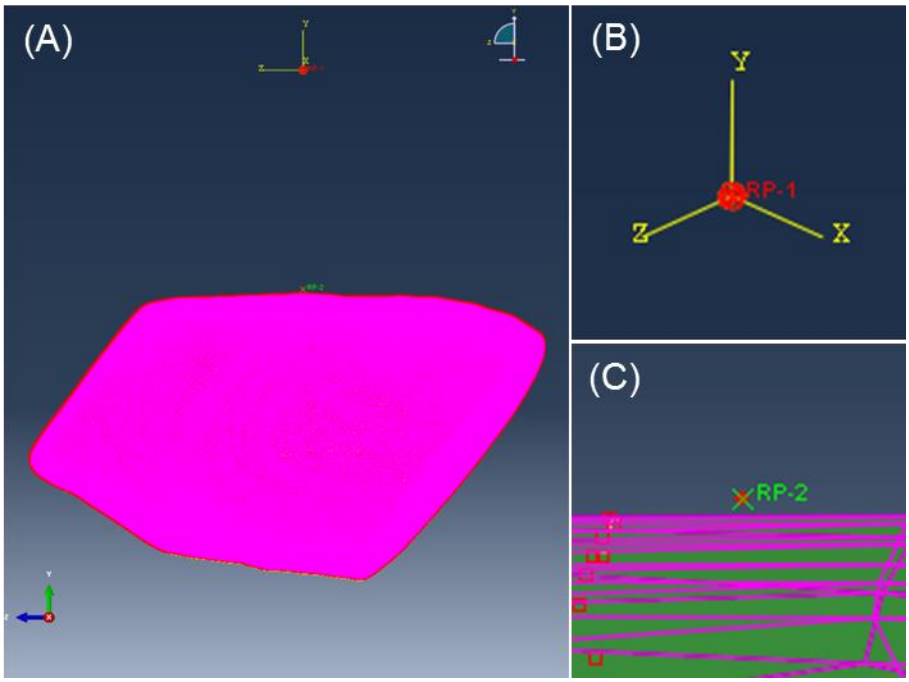

Figure 3.7 FE simulation setup for blast trauma.

Notes: (A) Sagittal view of the FE simulation setup for blast trauma. (B) RP-1 (red) represents the source point while (C) RP-2 (red) represents the standoff point. The elements comprising the air mesh have been removed to facilitate visualization of the FE setup.

The blast pressure profile selected for this study possessed a total impulse that was equal to the total impulse obtained from FE simulations of blunt trauma. The coarse mesh (Mesh #3) provided field outputs such as von Mises stress, maximum principal strain, and pressure. FE results were analyzed at the impact site on the skull, cerebral

cortex (i.e. *coup* site), corpus callosum, and hypothalamus (i.e. *countercoup* site) and subsequently compared to results from FE simulations of blunt trauma.

3.3 Results

3.3.1 Mesh Refinement

The mesh refinement study identified an appropriate mesh size that produced a reasonably accurate solution while maintaining computational efficiency. For each head mesh, the corresponding pressure distribution through the central region of the brain was used for comparison. The resulting pressures showed convergence with peak values of 0.71 MPa, 0.74 MPa, and 0.69 MPa for Mesh #1, #2, and #3, respectively (Figure 3.8).

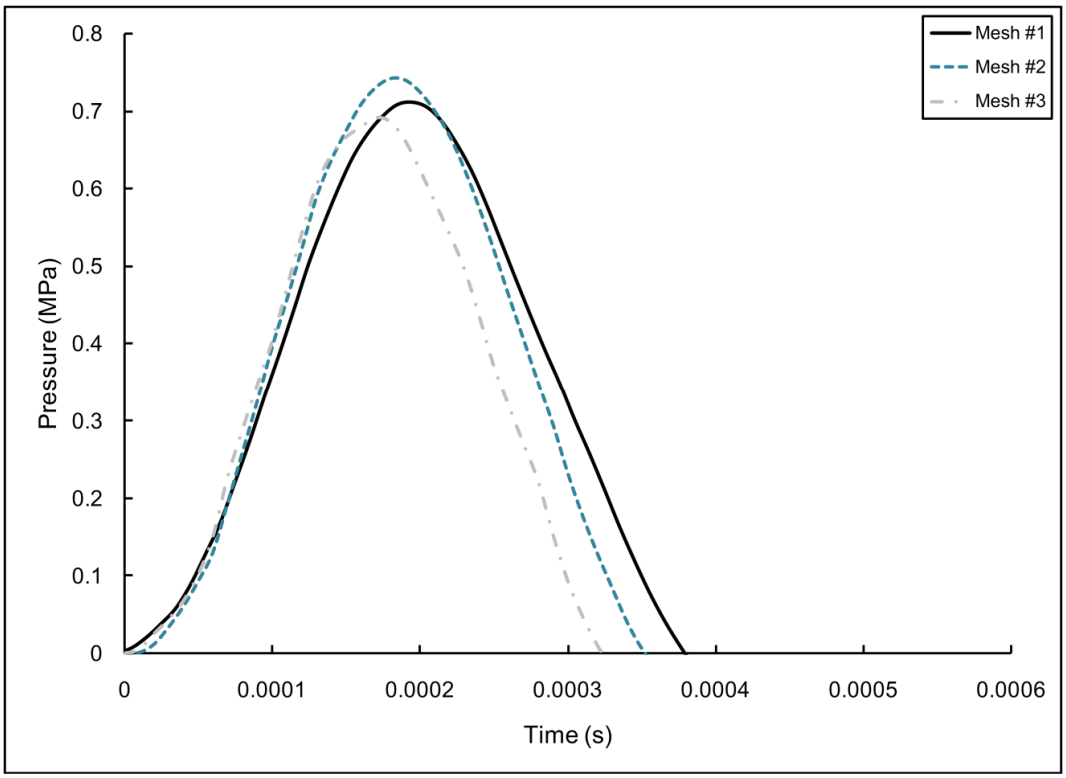

Figure 3.8 Comparison of pressure responses in the brain for various mesh sizes.

Notes: Mesh #1 and Mesh #2 comprised nearly 2.2 million and 1.1 million elements, respectively. Mesh #3 consisted of approximately 520,000 elements.

3.3.2 Validation

Validation of the head model involved a comparison between experimental data and FE simulations of blunt trauma. The pressure response from experiments was measured from data collected from the sensor mounted directly on the impactor tip. The pressure response from FE simulations was determined from analysis of the elements comprising the contact surface of the impactor, which possessed a cylindrical geometry and elastic material properties that were identical to the impactor used during experiments. The experimental and computational results exhibited similar trends in the pressure responses with a minor difference in the impact duration. Furthermore, the experimental and simulation results demonstrated good agreement with peak pressures of 4.8 MPa and 4.7 MPa, respectively (Figure 3.9).

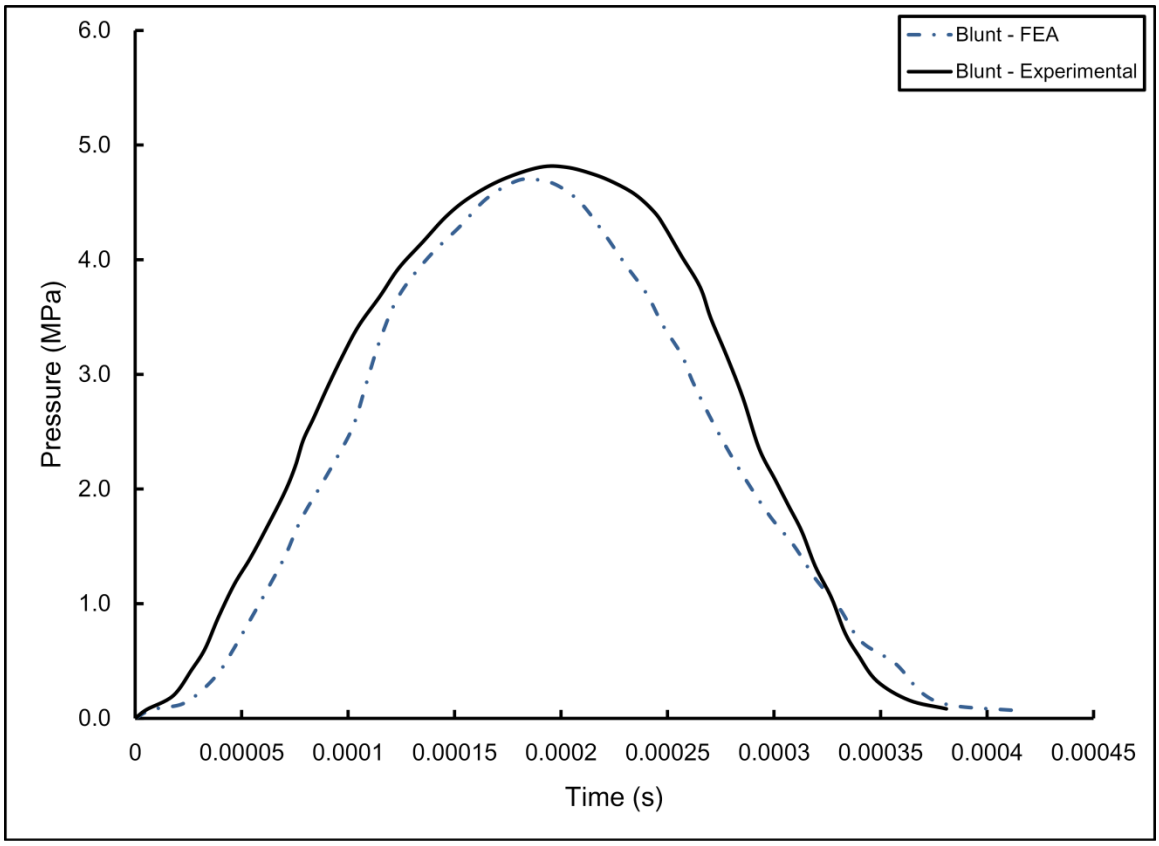

Figure 3.9 Comparison of the pressure responses obtained from experiments and FE simulations of blunt trauma.

3.3.3 FE Simulations

Figure 3.10 and Figure 3.11 show the pressure response in the entire head model at various times during FE simulations of blunt trauma. Figure 3.12 and Figure 3.13 show the corresponding pressure response during blast trauma. Computational analysis of the skull revealed that blunt trauma produced a maximum pressure of 19.8 MPa while blast trauma generated a maximum pressure of 31.7 MPa.

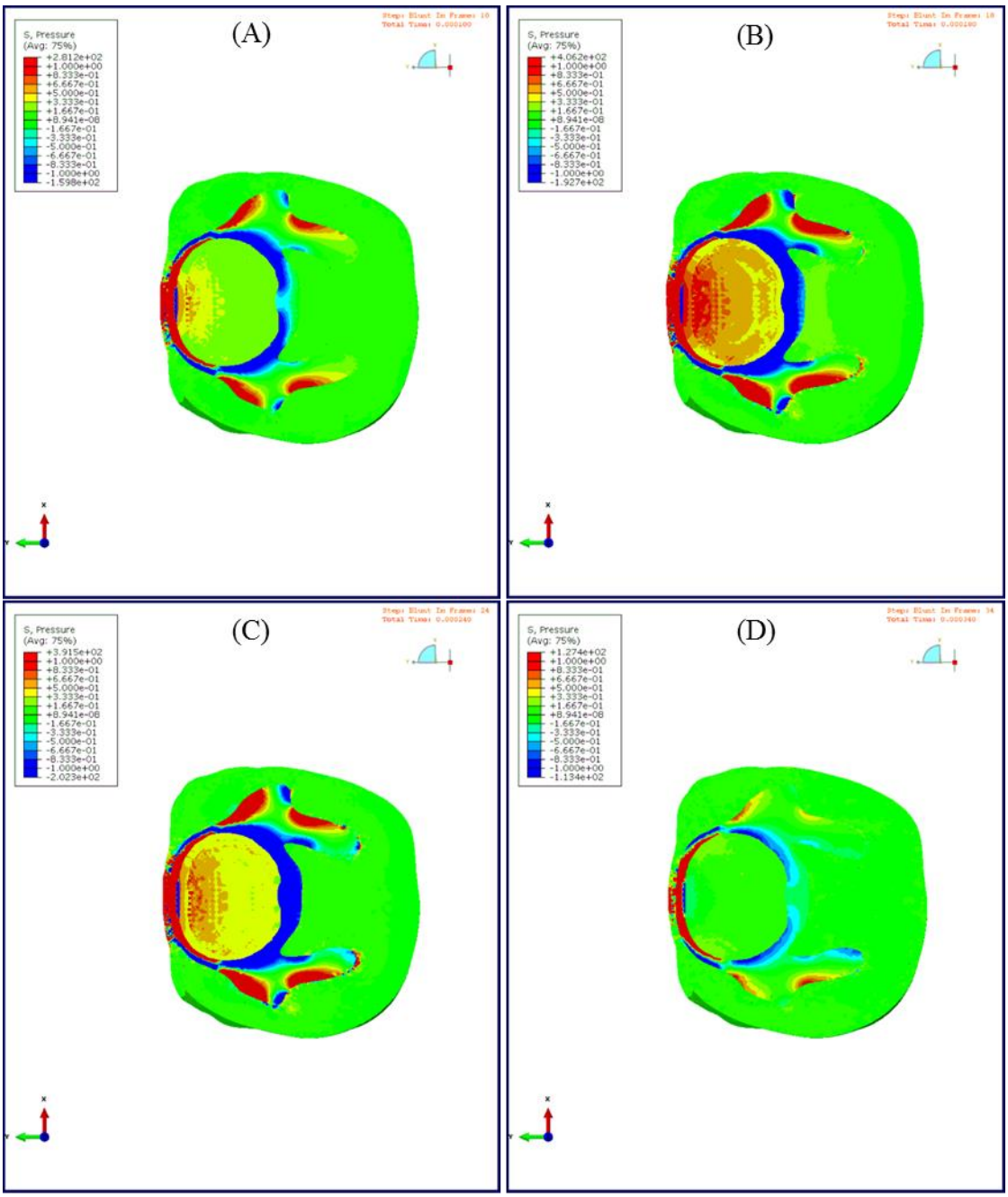

Figure 3.10 Mid-coronal views of the pressure in the entire head model during FE simulation of blunt trauma

(A) 0.00010 s, (B) 0.00018 s, (C) 0.00024 s, and (D) 0.00034 s.

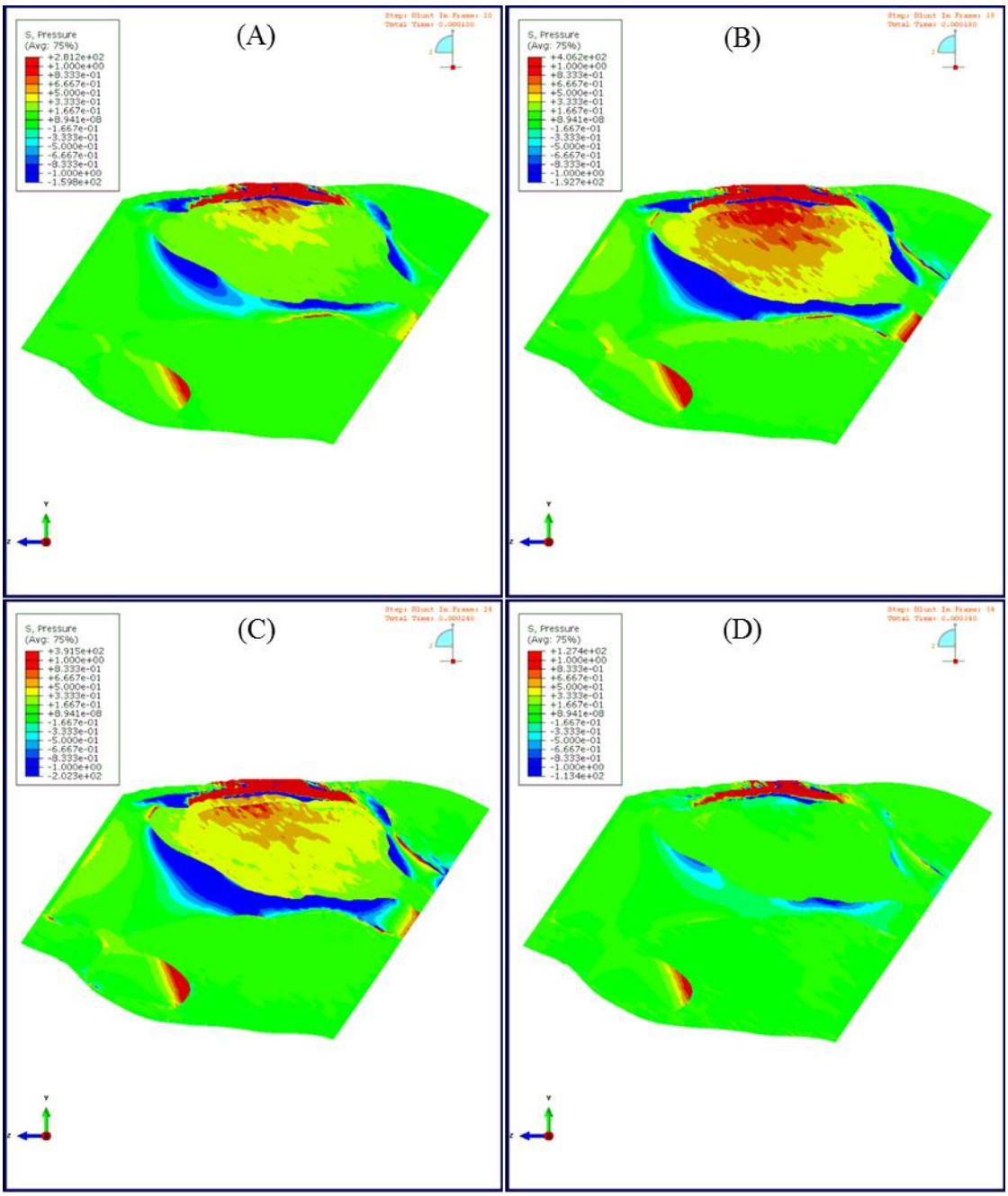

Figure 3.11 Mid-sagittal views of the pressure in the entire head model during FE simulation of blunt trauma

(A) 0.00010 s, (B) 0.00018 s, (C) 0.00024 s, and (D) 0.00034 s.

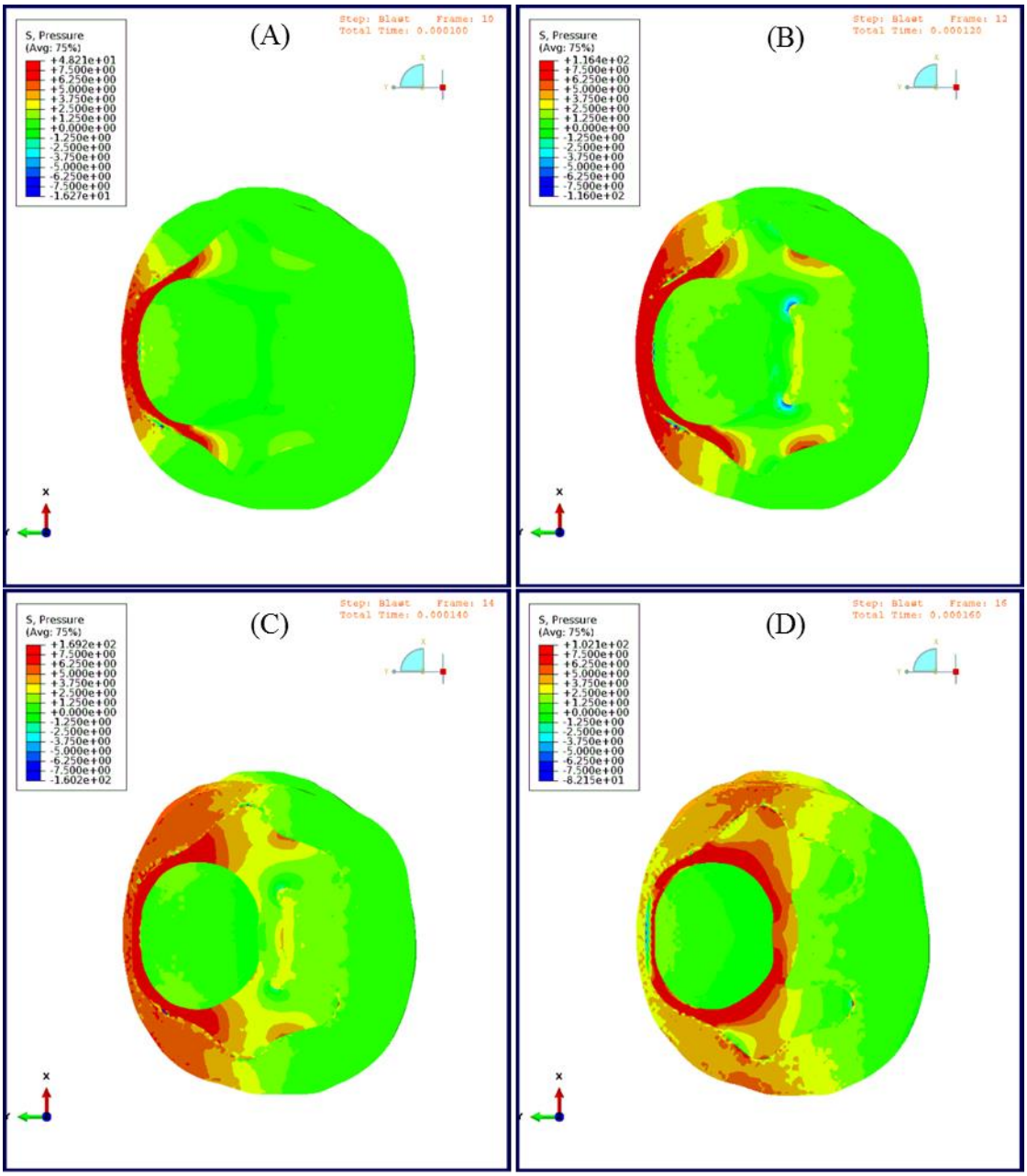

Figure 3.12 Mid-coronal views of the pressure in the entire head model during FE simulation of blast trauma

(A) 0.00010 s, (B) 0.00012 s, (C) 0.00014 s, and (D) 0.00016 s.

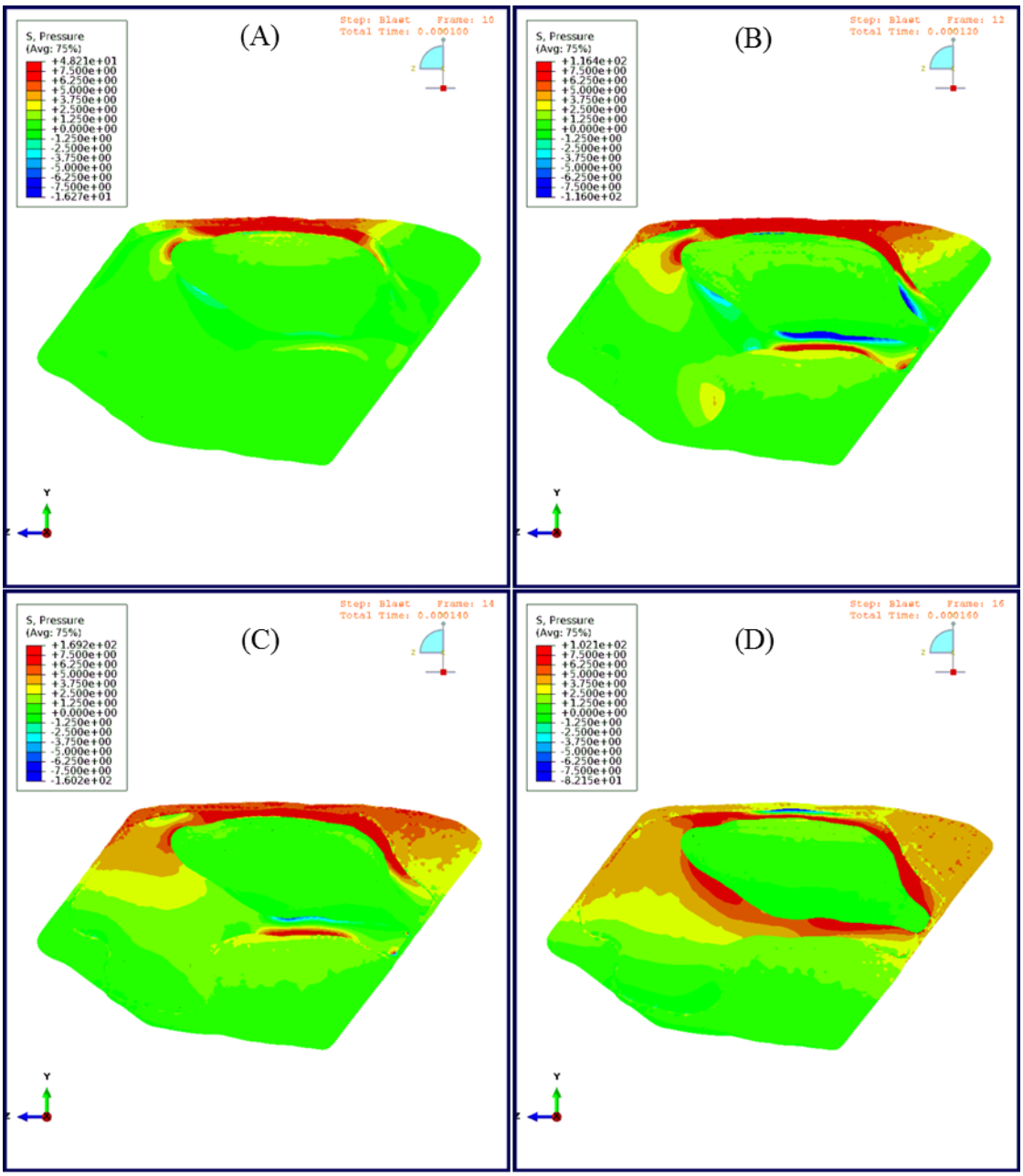

Figure 3.13 Mid-sagittal views of the pressure in the entire head model during FE simulation of blast trauma

(A) 0.00010 s, (B) 0.00012 s, (C) 0.00014 s, and (D) 0.00016 s.

Figure 3.14 and Figure 3.15 show the von Mises stress distribution for the brain in FE simulations of blunt trauma while Figure 3.16 and Figure 3.17 show the

corresponding computational results for blast trauma. Table 3.3 shows the maximum von Mises stresses at three different brain locations based on the injury induced. Computational results revealed that blast injury led to higher maximum von Mises stresses in the cerebral cortex, corpus callosum, and hypothalamus compared to blunt injury.

Table 3.3 Summary of FE simulation results according to injury type and brain location.

FE Simulation Parameter	Injury Case	Cerebral Cortex	Corpus Callosum	Hypothalamus
Von Mises Stress (MPa)	Blunt Trauma	0.27	0.27	0.09
	Blast Trauma	0.42	0.44	0.27
Pressure (MPa)	Blunt Trauma	0.82	0.67	0.49
	Blast Trauma	1.58	1.24	1.16
Maximum Principal Strain	Blunt Trauma	0.009	0.008	0.001
	Blast Trauma	0.011	0.010	0.005

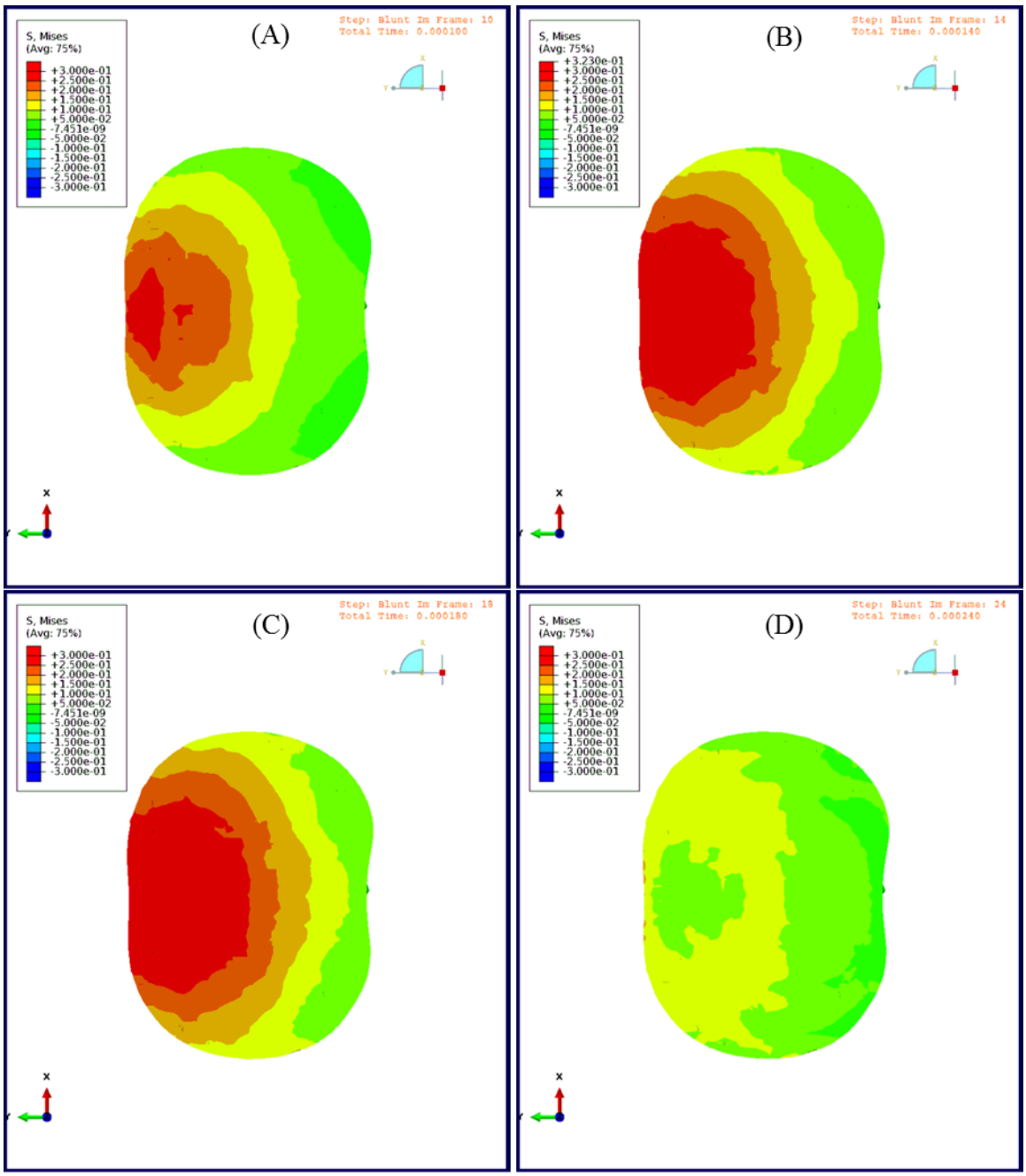

Figure 3.14 Mid-coronal views of the Von Mises stress in the brain model during FE simulation of blunt trauma

(A) 0.00010 s, (B) 0.00014 s, (C) 0.00018 s, and (D) 0.00024 s.

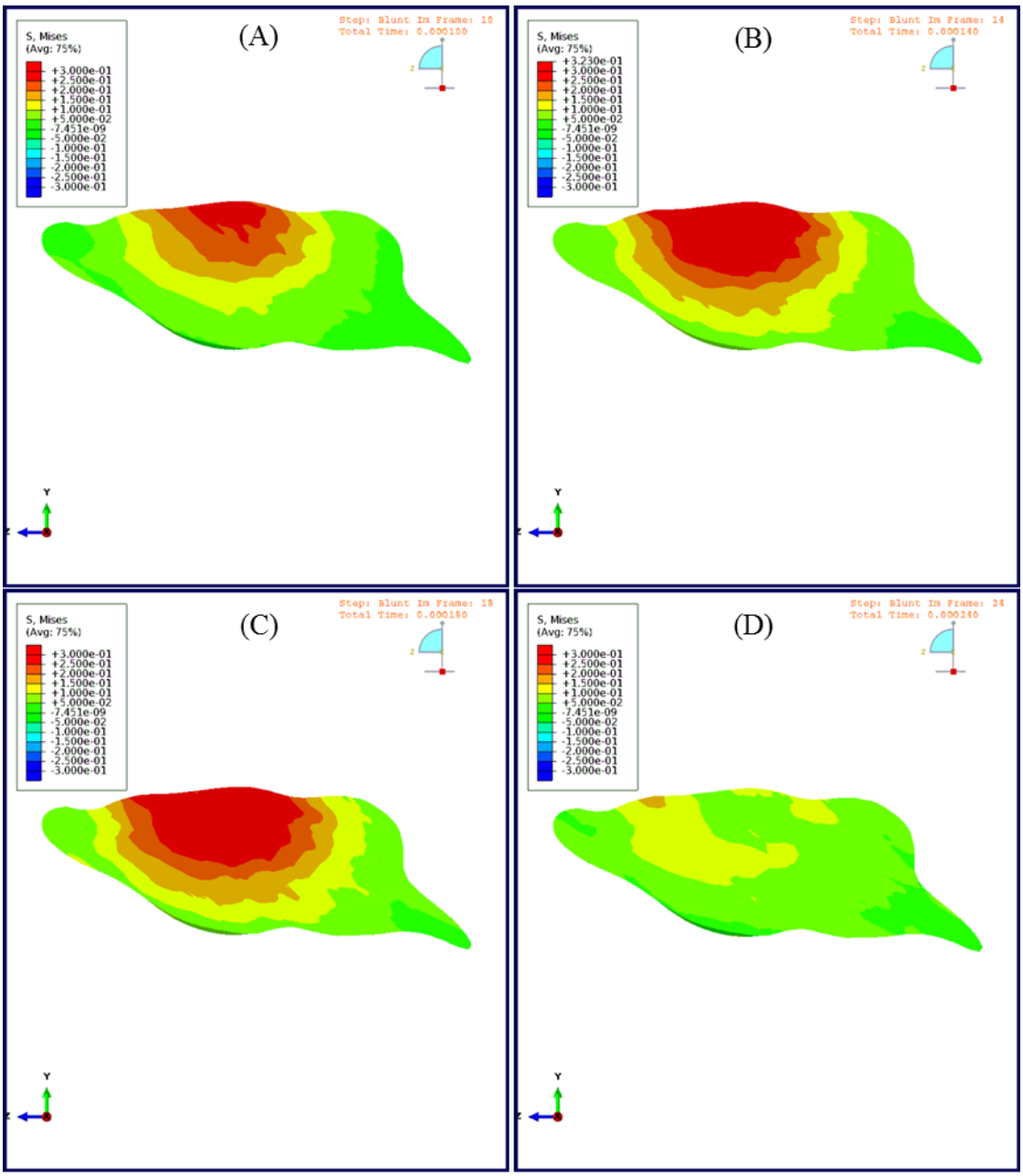

Figure 3.15 Mid-sagittal views of the Von Mises stress in the brain model during FE simulation of blunt trauma

(A) 0.00010 s, (B) 0.00014 s, (C) 0.00018 s, and (D) 0.00024 s.

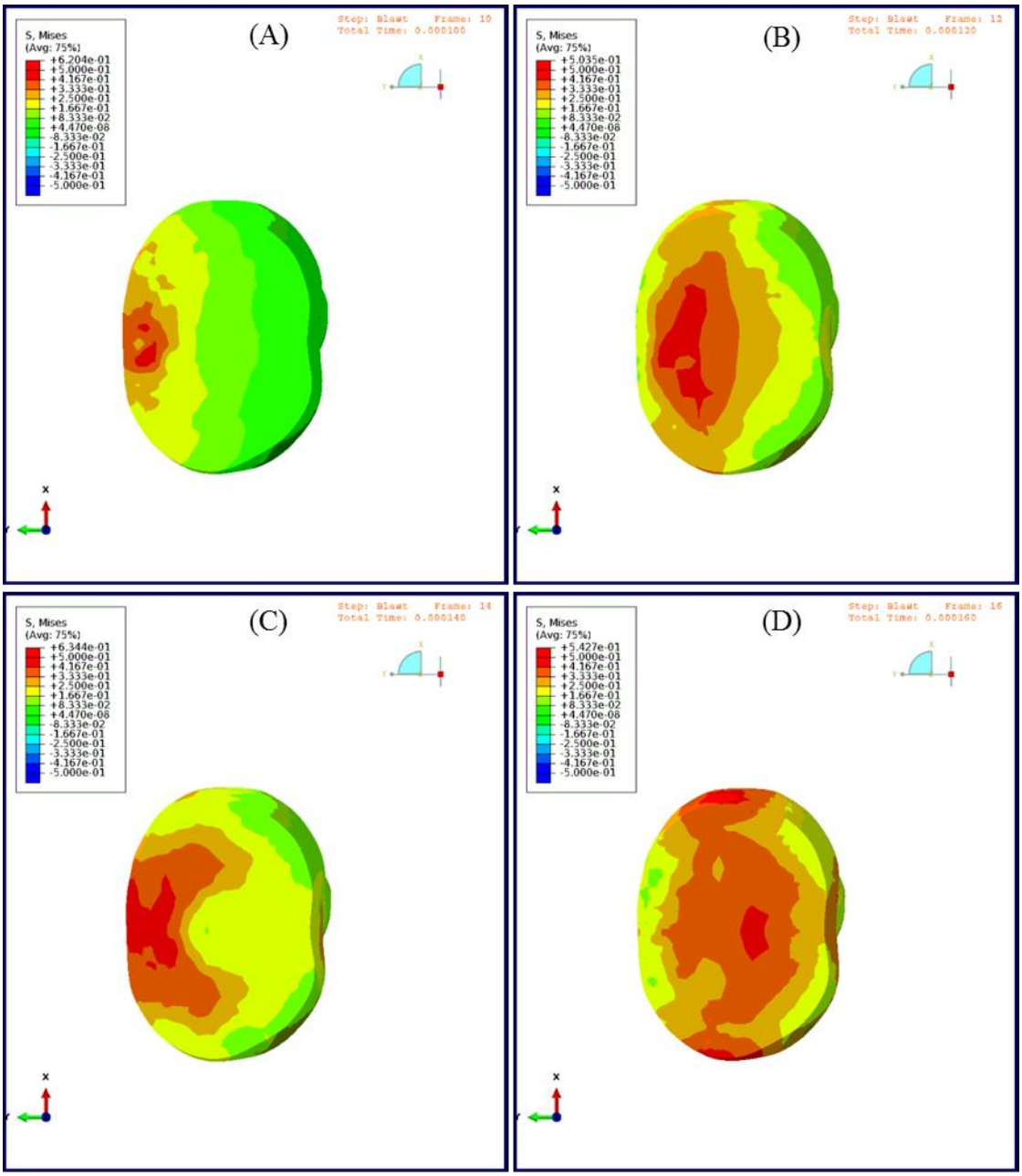

Figure 3.16 Mid-coronal views of the Von Mises stress in the brain model during FE simulation of blast trauma

(A) 0.00010 s, (B) 0.00012 s, (C) 0.00014 s, and (D) 0.00016 s.

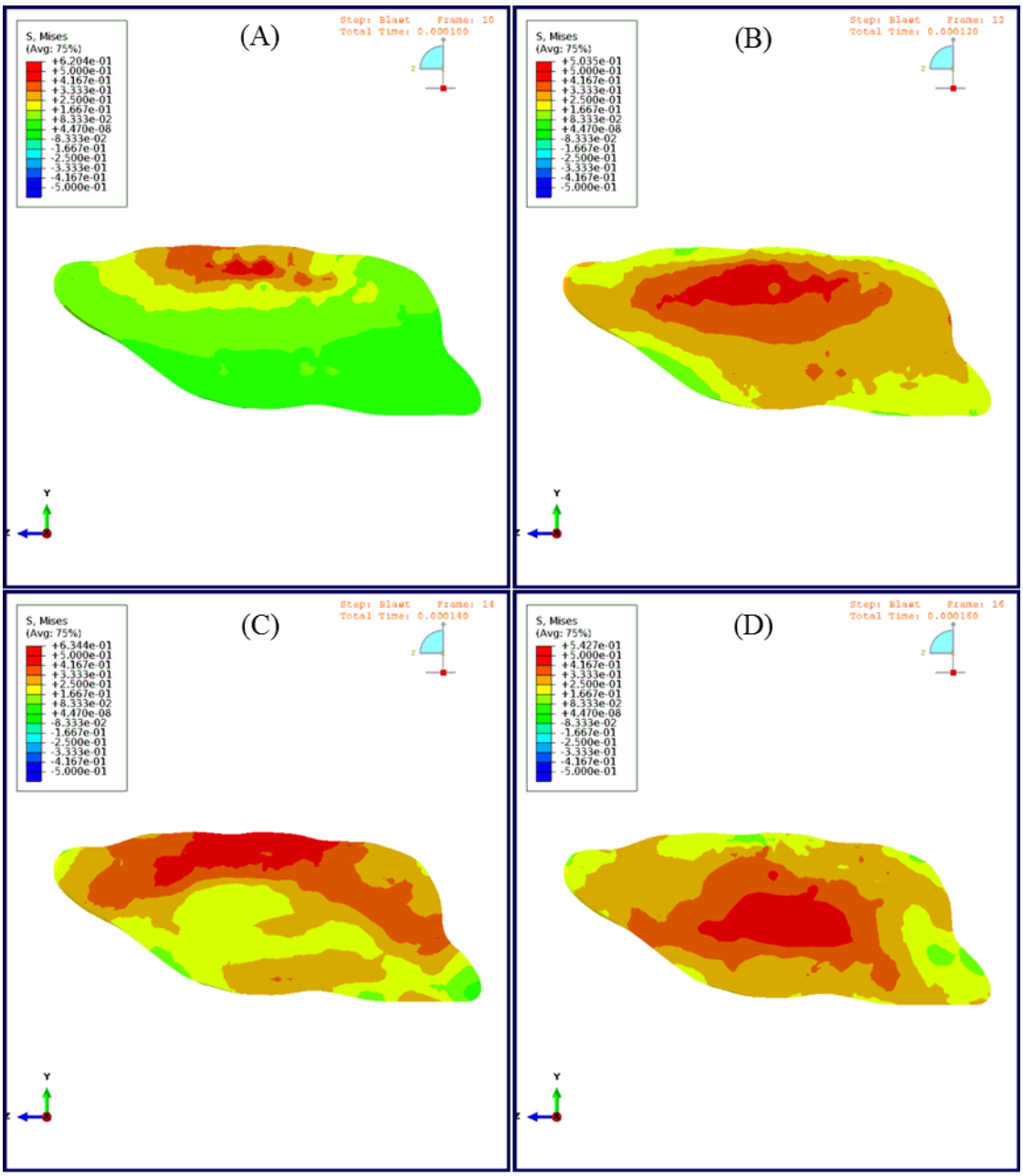

Figure 3.17 Mid-sagittal views of the Von Mises stress in the brain model during FE simulation of blast trauma

(A) 0.00010 s, (B) 0.00012 s, (C) 0.00014 s, and (D) 0.00016 s.

Figure 3.18 and Figure 3.19 illustrate the pressure response in the brain at different times following blunt trauma. Figure 3.20 and Figure 3.21 display the

corresponding pressure response during blast trauma. In both injury cases, the maximum pressure gradually decreased as the distance from the impact site increased (Table 3.3). Furthermore, blast trauma generated higher maximum pressures within all three brain locations when compared to FE blunt trauma results.

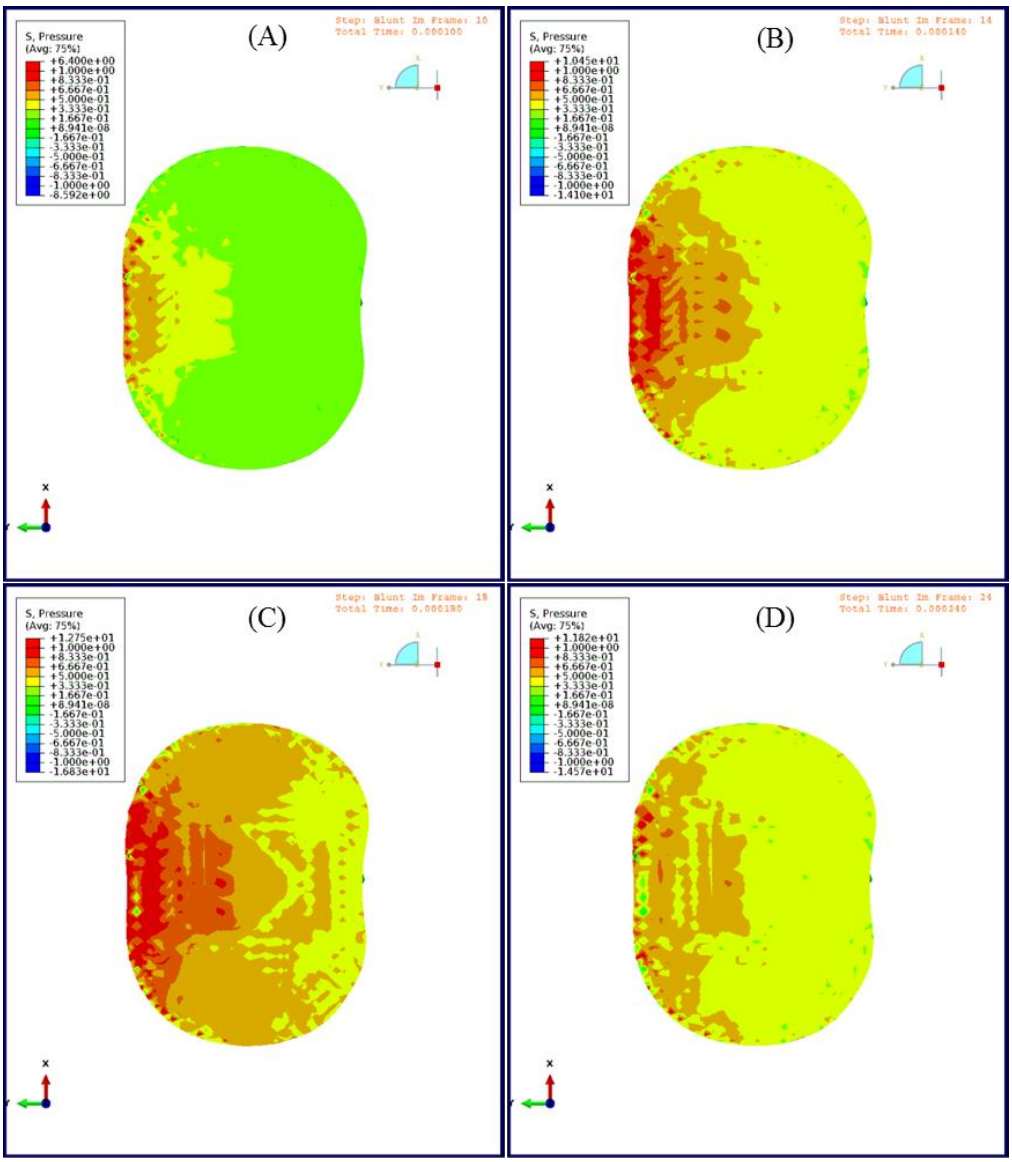

Figure 3.18 Mid-coronal views of the pressure in the brain model during FE simulation of blunt trauma

(A) 0.00010 s, (B) 0.00014 s, (C) 0.00018 s, and (D) 0.00024 s.

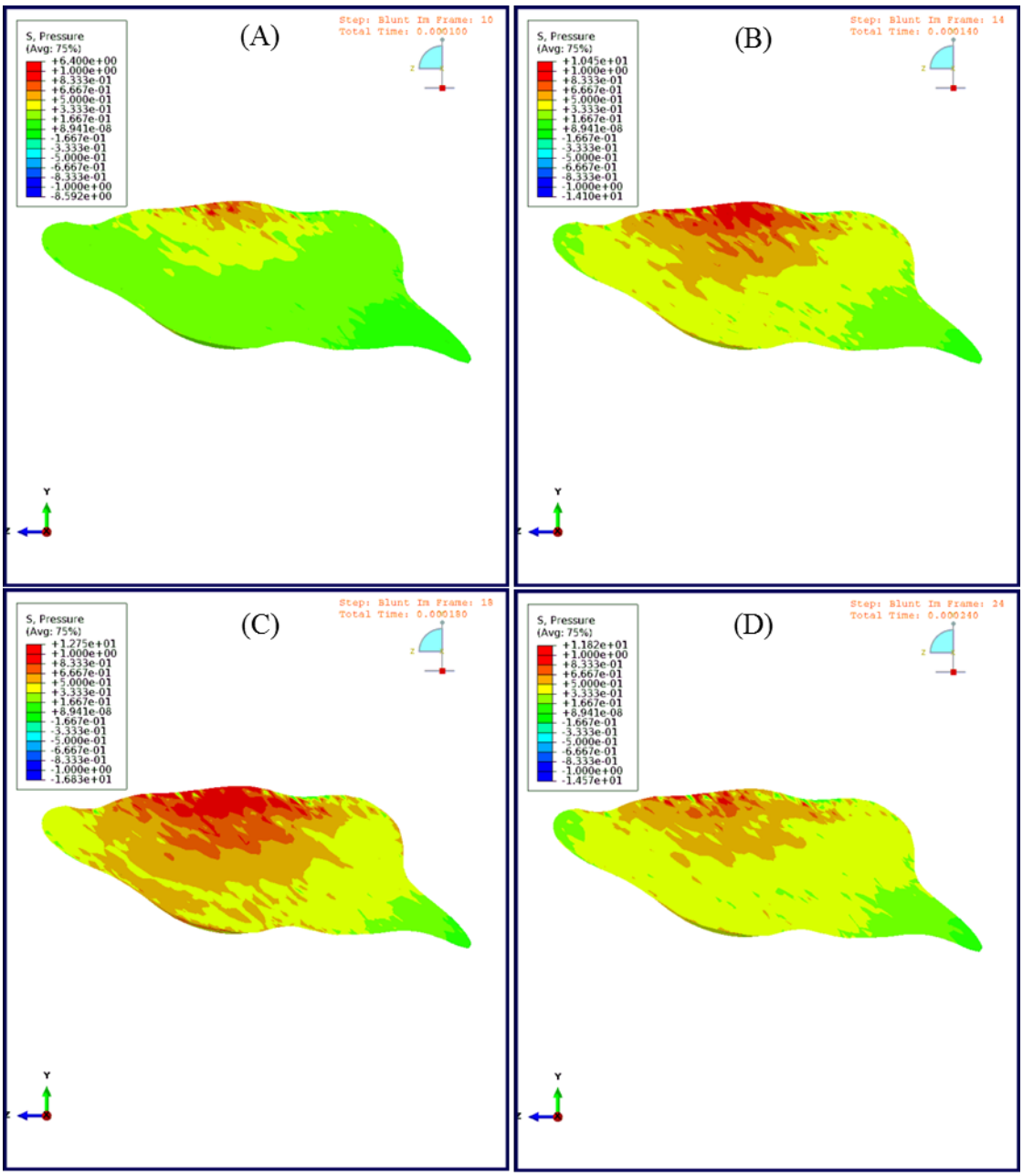

Figure 3.19 Mid-sagittal views of the pressure in the brain model during FE simulation of blunt trauma

(A) 0.00010 s, (B) 0.00014 s, (C) 0.00018 s, and (D) 0.00024 s.

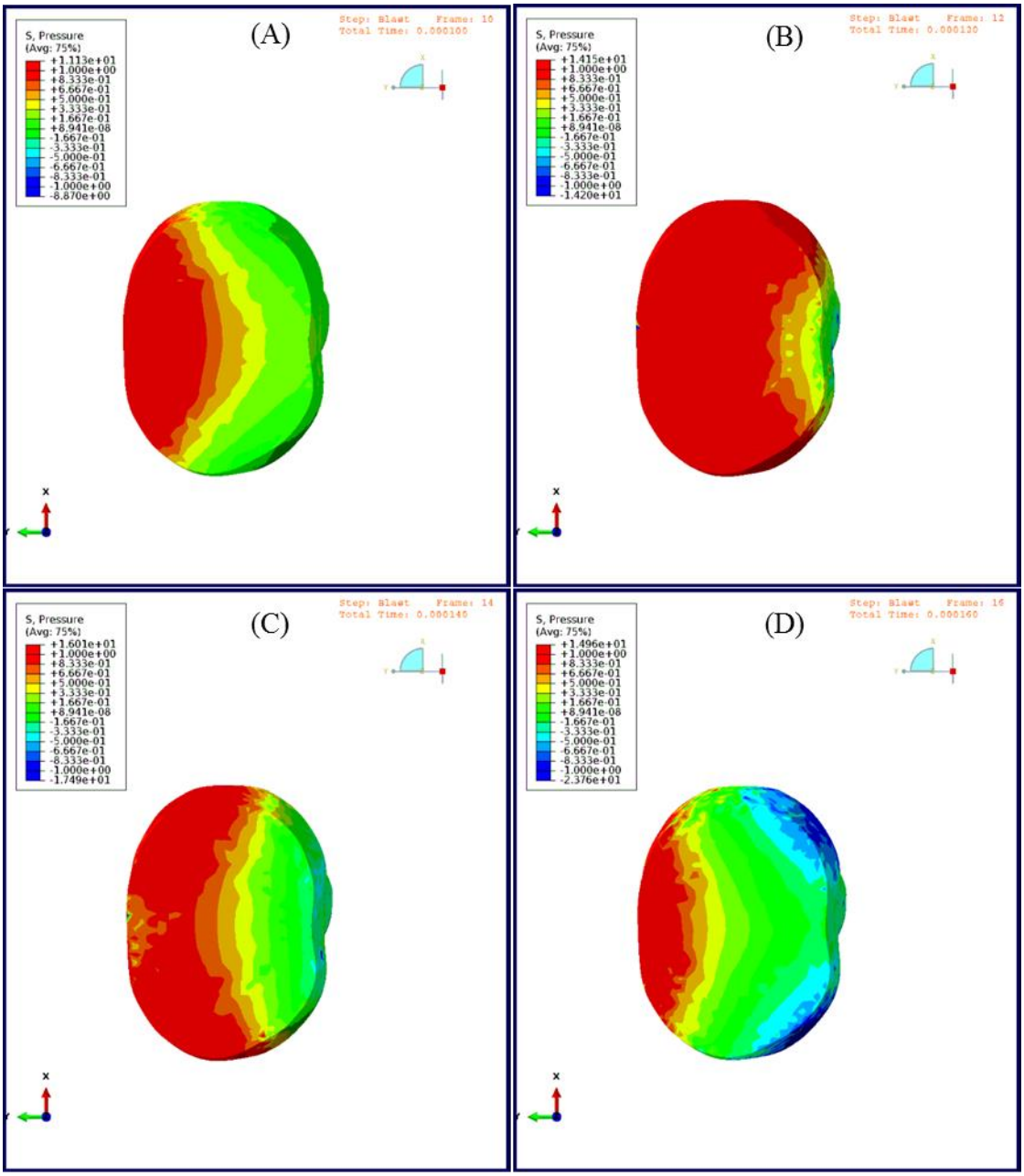

Figure 3.20 Mid-coronal views of the pressure in the brain model during FE simulation of blast trauma

(A) 0.00010 s, (B) 0.00012 s, (C) 0.00014 s, and (D) 0.00016 s.

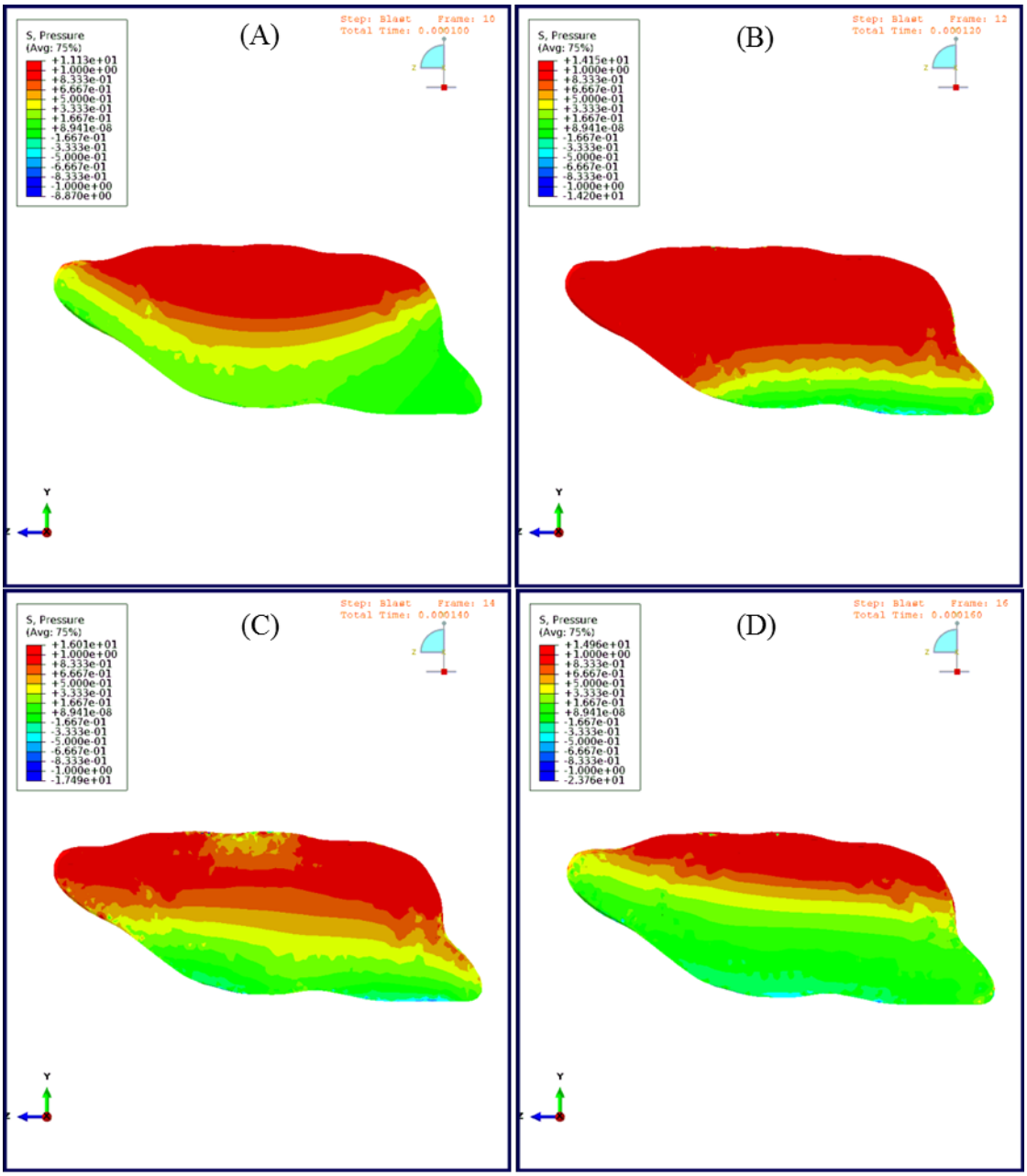

Figure 3.21 Mid-sagittal views of the pressure in the brain model during FE simulation of blast trauma

(A) 0.00010 s, (B) 0.00012 s, (C) 0.00014 s, and (D) 0.00016 s.

Figure 3.22 and Figure 3.23 exhibit the maximum principal strain throughout the brain at various times in FE simulations of blunt trauma. Figure 3.24 and Figure 3.25

show the subsequent FE results following blast trauma. Based on comparisons of the three brain locations, the maximum principal strain demonstrates a decreasing trend as the distance from the impact site increases (Table 3.3). Although the differences are relatively minor, FE blast trauma simulations led to higher maximum principal strains than the FE blunt trauma simulations.

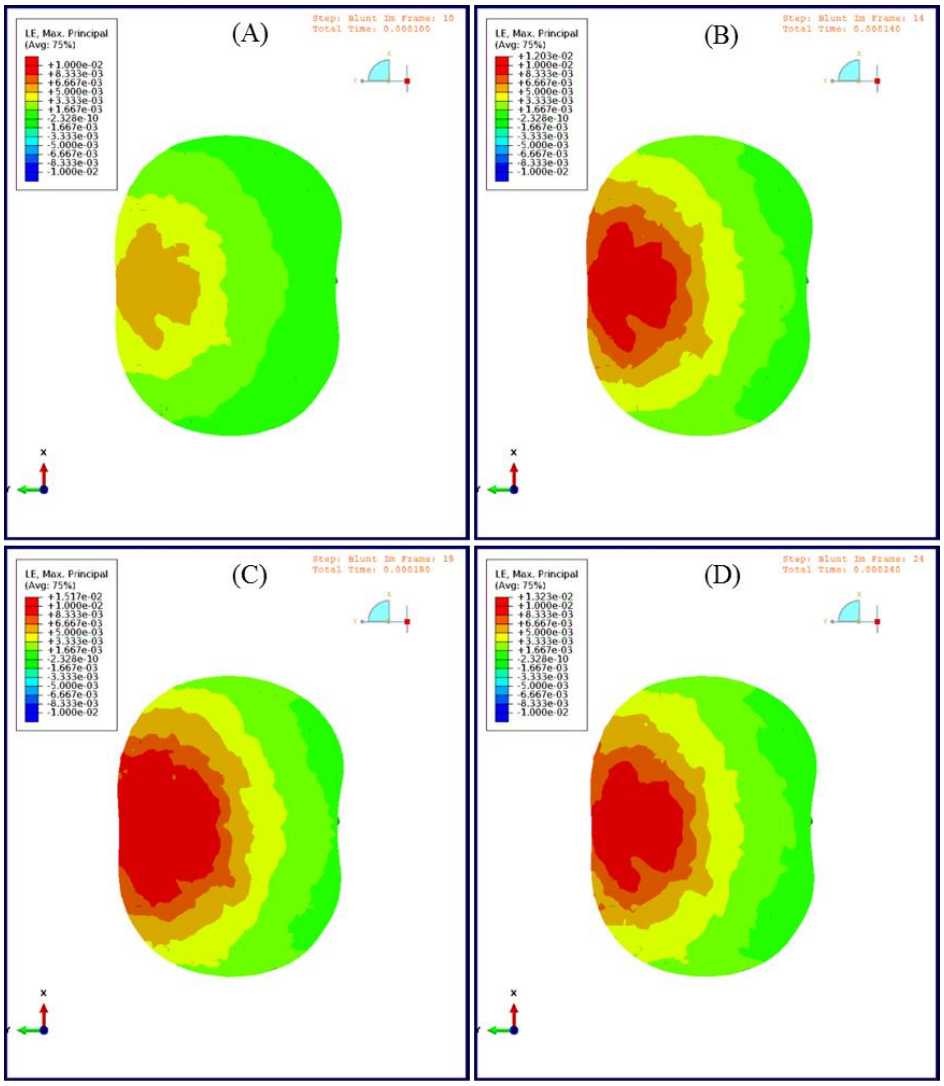

Figure 3.22 Mid-coronal views of the maximum principal strain in the brain model during FE simulation of blunt trauma

(A) 0.00010 s, (B) 0.00014 s, (C) 0.00018 s, and (D) 0.00024 s.

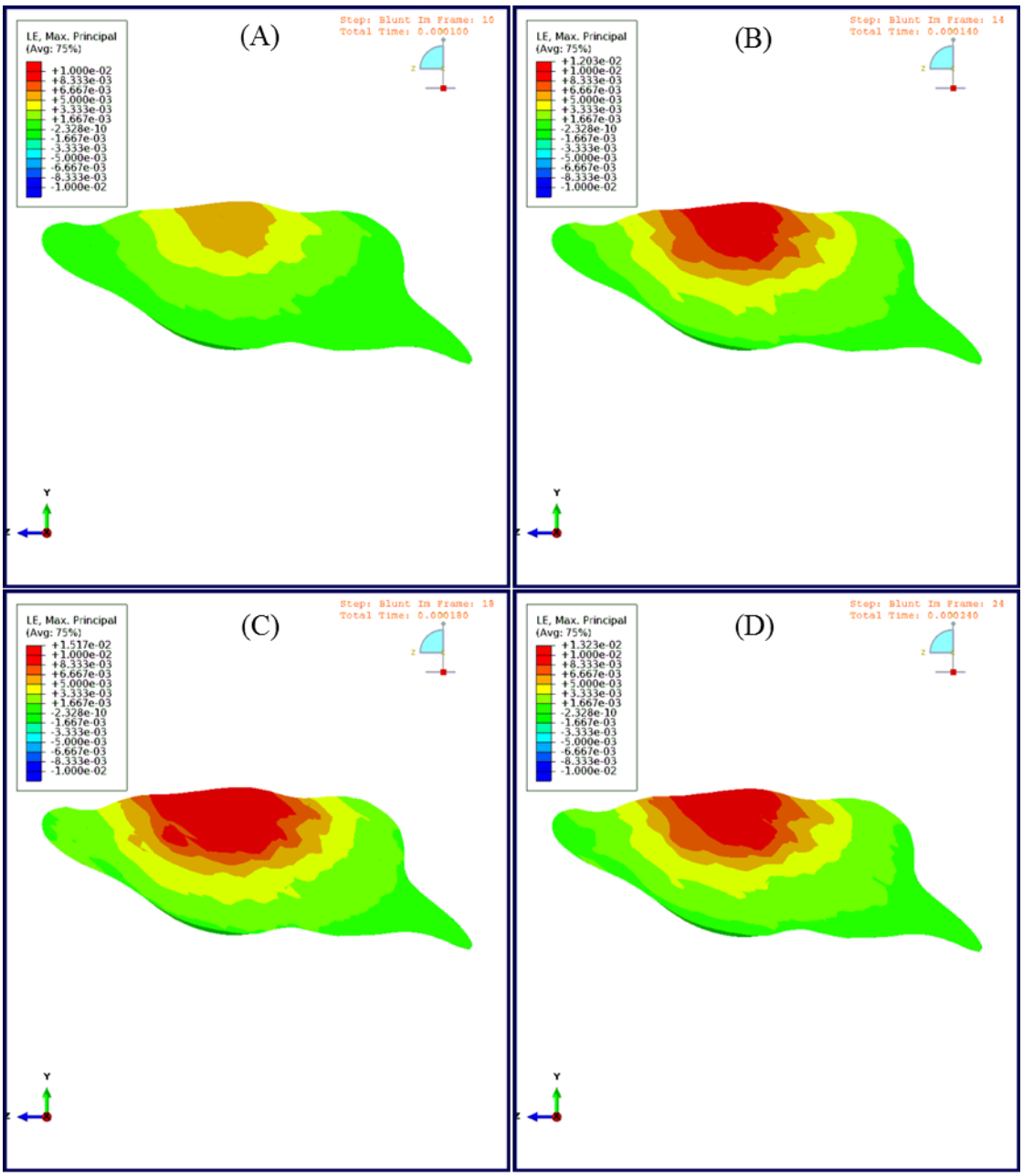

Figure 3.23 Mid-sagittal views of the maximum principal strain in the brain model during FE simulation of blunt trauma

(A) 0.00010 s, (B) 0.00014 s, (C) 0.00018 s, and (D) 0.00024 s.

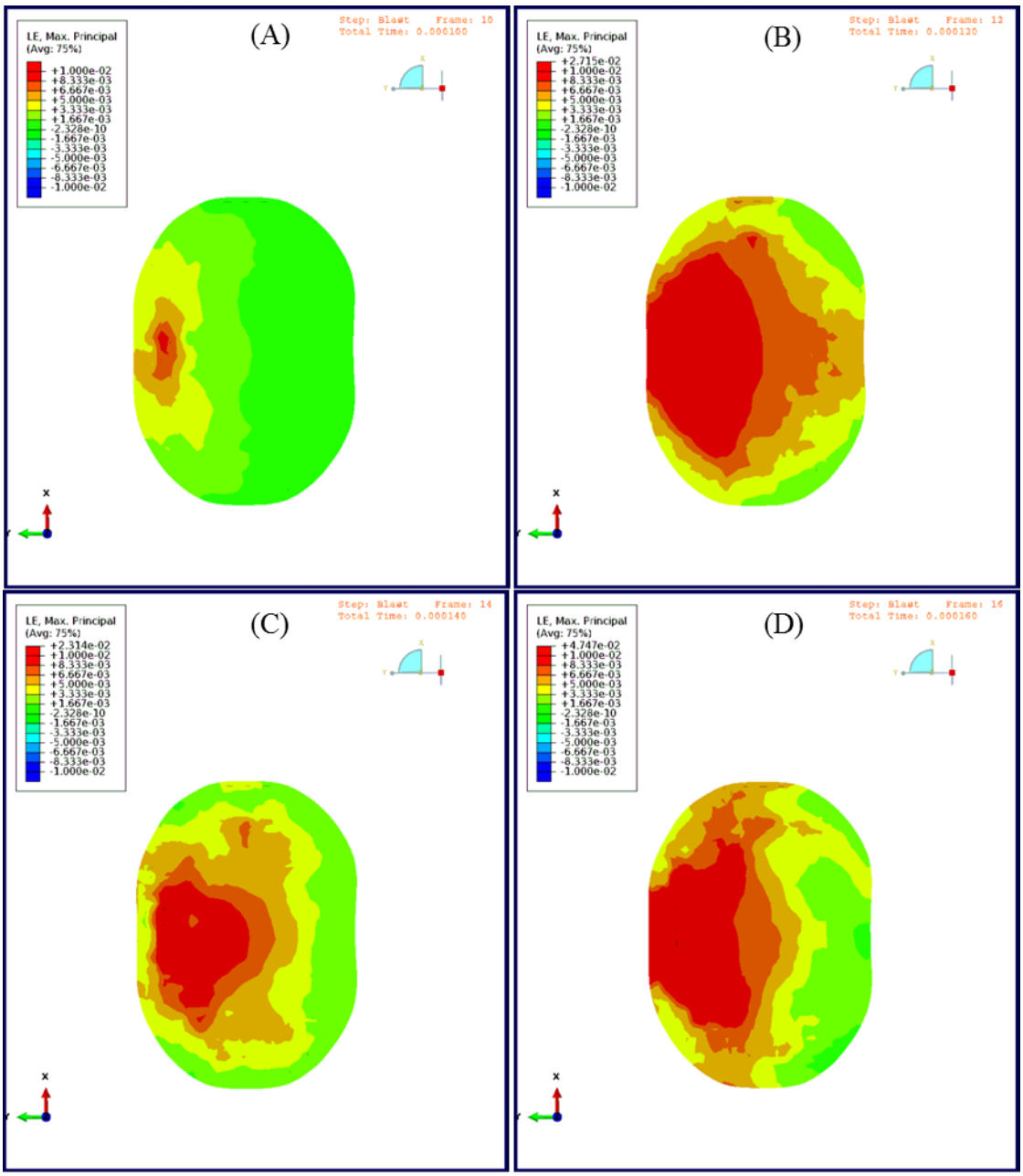

Figure 3.24 Mid-coronal views of the maximum principal strain in the brain model during FE simulation of blast trauma

(A) 0.00010 s, (B) 0.00012 s, (C) 0.00014 s, and (D) 0.00016 s.

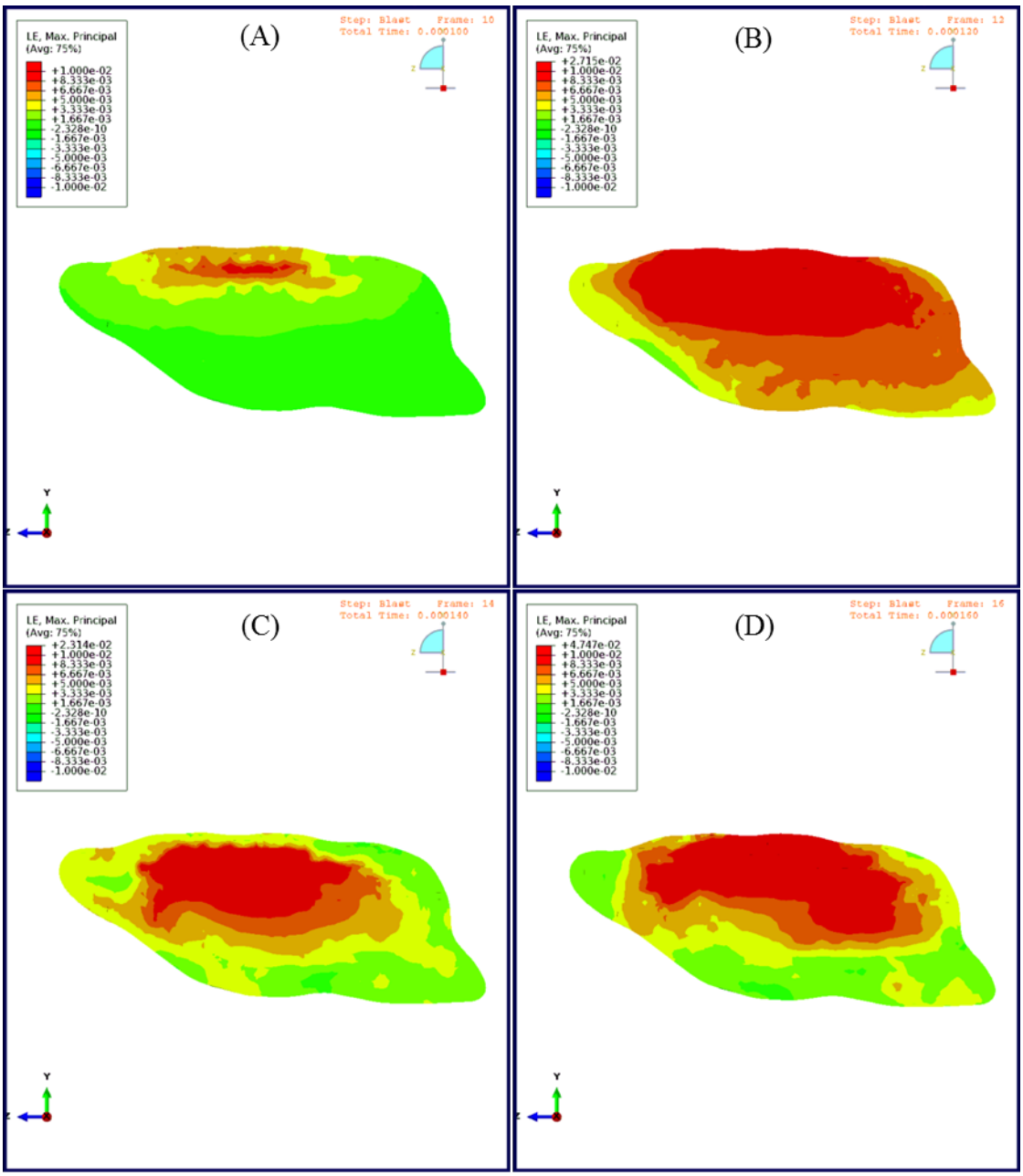

Figure 3.25 Mid-sagittal views of the maximum principal strain in the brain model during FE simulation of blast trauma

(A) 0.00010 s, (B) 0.00012 s, (C) 0.00014 s, and (D) 0.00016 s.

At four different locations, the von Mises stress distributions exhibited more oscillations following blast trauma and displayed a predominantly compressive response

following blunt trauma (Figure 3.26). For both blunt and blast injury, the von Mises stresses were higher by two orders of magnitude in the skull compared to the cerebral cortex, corpus callosum, and hypothalamus. This result is most likely attributed to the higher mechanical strength of bone, which facilitated mitigation of the initial stress wave before it propagated further into the brain.

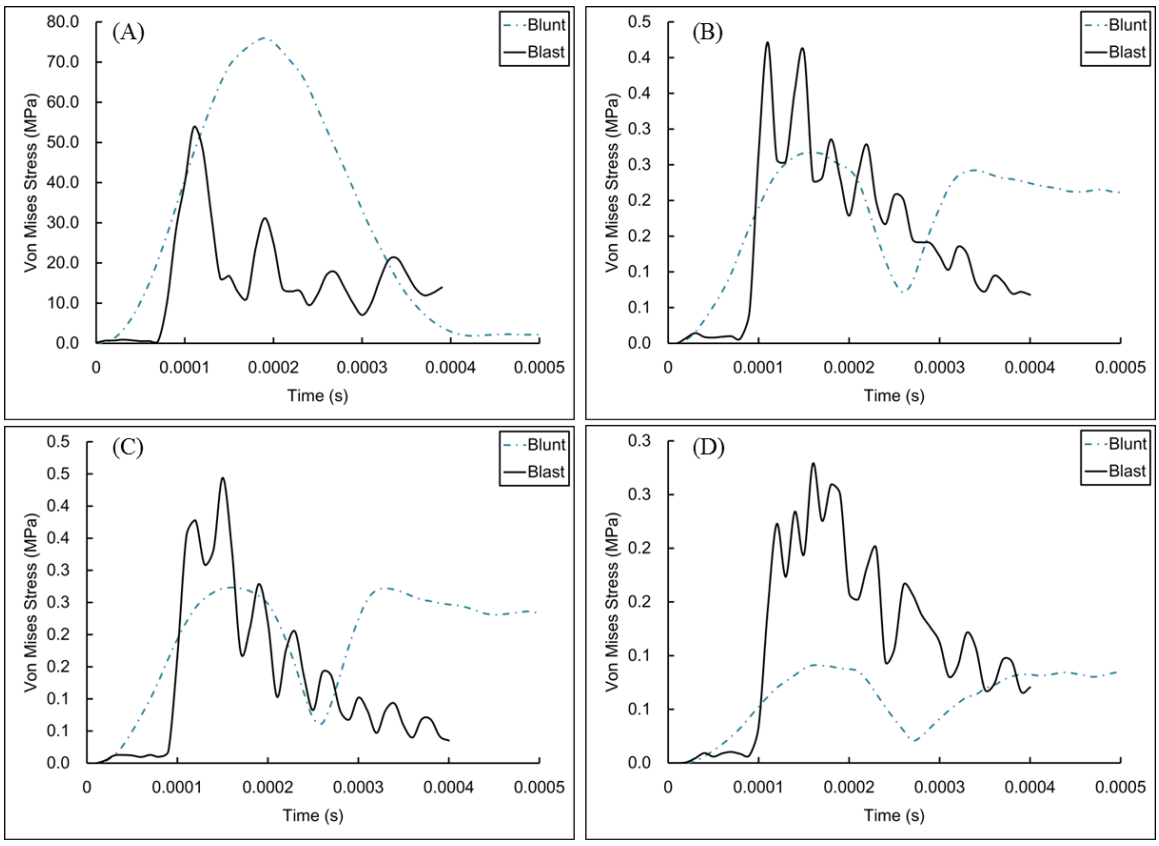

Figure 3.26 Comparison of the Von Mises stress responses from FE simulations of blunt and blast trauma, respectively.

Notes: The four locations analyzed included the (A) skull, (B) cerebral cortex, (C) corpus callosum, and (D) hypothalamus.

Different regions of the head also yielded distinct pressure responses. For blunt trauma, the corresponding pressure plots were characterized by wide compressive

responses and peak pressures at approximately 0.00018 s. Conversely, blast trauma produced pressure plots with alternating compressive and tensile responses in the skull, cerebral cortex, and corpus callosum. Furthermore, blast trauma led to overpressures that occurred at approximately 0.0001 s, which was nearly 80 microseconds sooner than with blunt trauma (Figure 3.27). Compared to other head locations, the hypothalamus exhibited an abrupt increase and ensuing decrease in blast pressure before reaching its peak at approximately 0.0002 s.

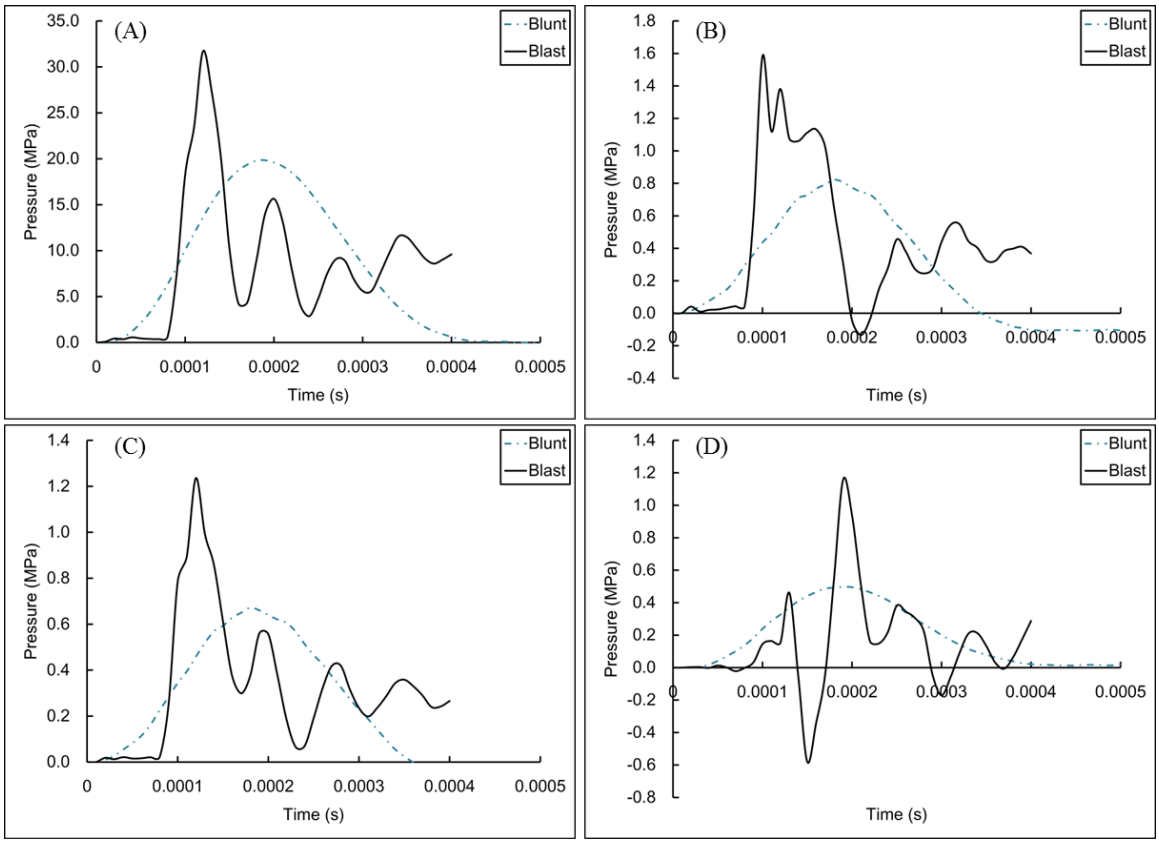

Figure 3.27 Comparison of the pressure responses from FE simulations of blunt and blast trauma, respectively.

Notes: The four locations analyzed included the (A) skull, (B) cerebral cortex, (C) corpus callosum, and (D) hypothalamus.

The corresponding impulses in the skull, cerebral cortex, corpus callosum, and hypothalamus exhibited behavior that was similar to the aforementioned pressure responses (Figure 3.28). Although the total impulse was the same in FE simulations of blunt and blast trauma, respectively, the cumulative impulses showed slight differences in each head location as time progressed (Figure 3.29). Based on comparisons of the cumulative impulses, blunt injury produced a more gradual transition than blast injury throughout all four head regions. Furthermore, the cumulative impulses were relatively close in the skull, cerebral cortex, and corpus callosum, but the hypothalamus produced a larger disparity between the two injury conditions.

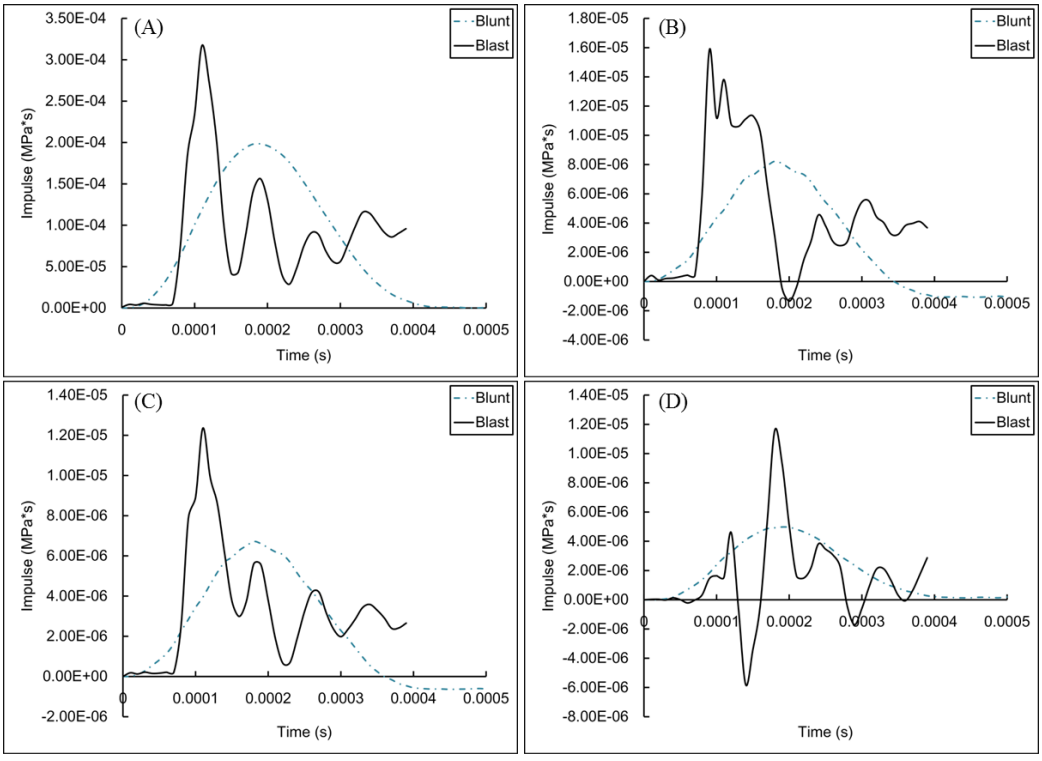

Figure 3.28 Comparison of the impulses from FE simulations of blunt and blast trauma, respectively.

Notes: The four locations analyzed included the (A) skull, (B) cerebral cortex, (C) corpus callosum, and (D) hypothalamus.

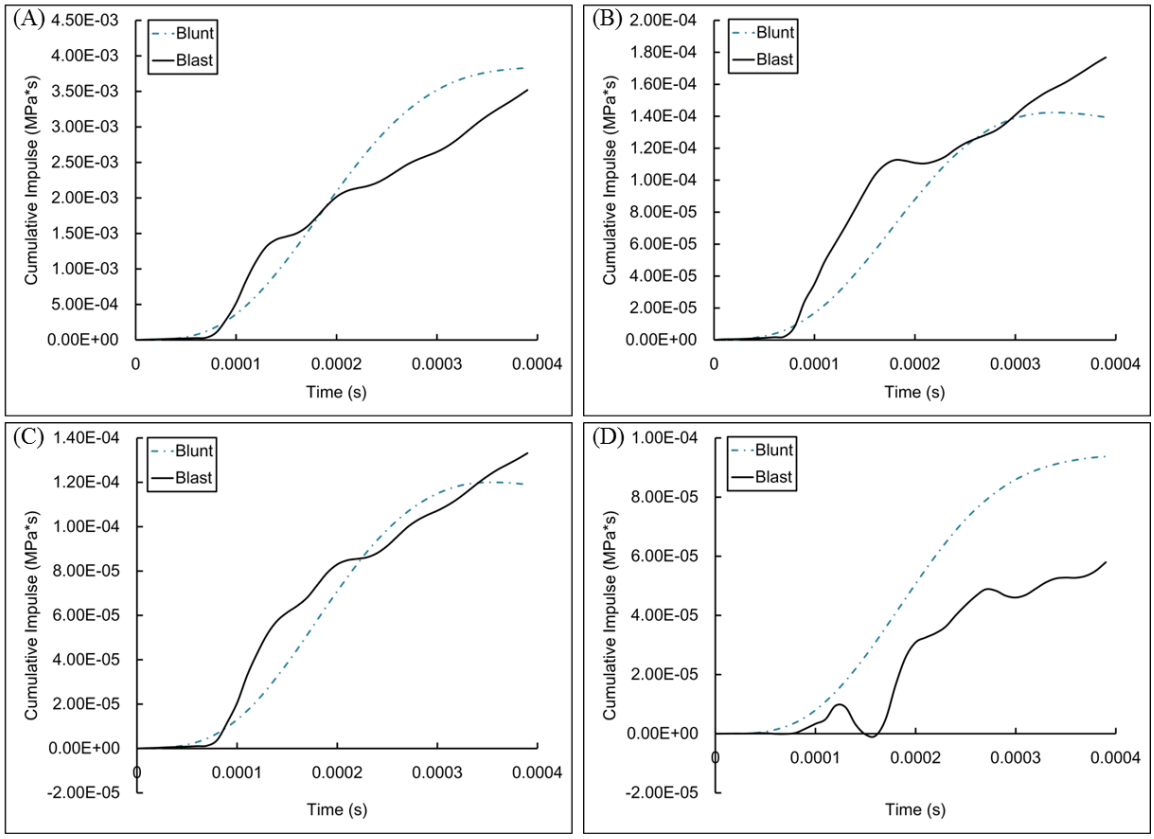

Figure 3.29 Comparison of the cumulative impulses from FE simulations of blunt and blast trauma, respectively.

Notes: The four locations analyzed included the (A) skull, (B) cerebral cortex, (C) corpus callosum, and (D) hypothalamus.

Blunt and blast trauma differentially influenced the normal and shear stresses at each head location. The normal stresses in the direction of loading (Figure 3.30) and orthogonal to the direction of loading (Figure 3.31 and Figure 3.32) exhibited a predominantly compressive response in the skull, cerebral cortex, and corpus callosum. However, the hypothalamus experienced both tension and compression as time progressed. Gradual transitions were also evident in the shear response following blunt injury, but blast injury generated shear stresses that were characterized by an oscillatory response (Figure 3.33, Figure 3.34, and Figure 3.35).

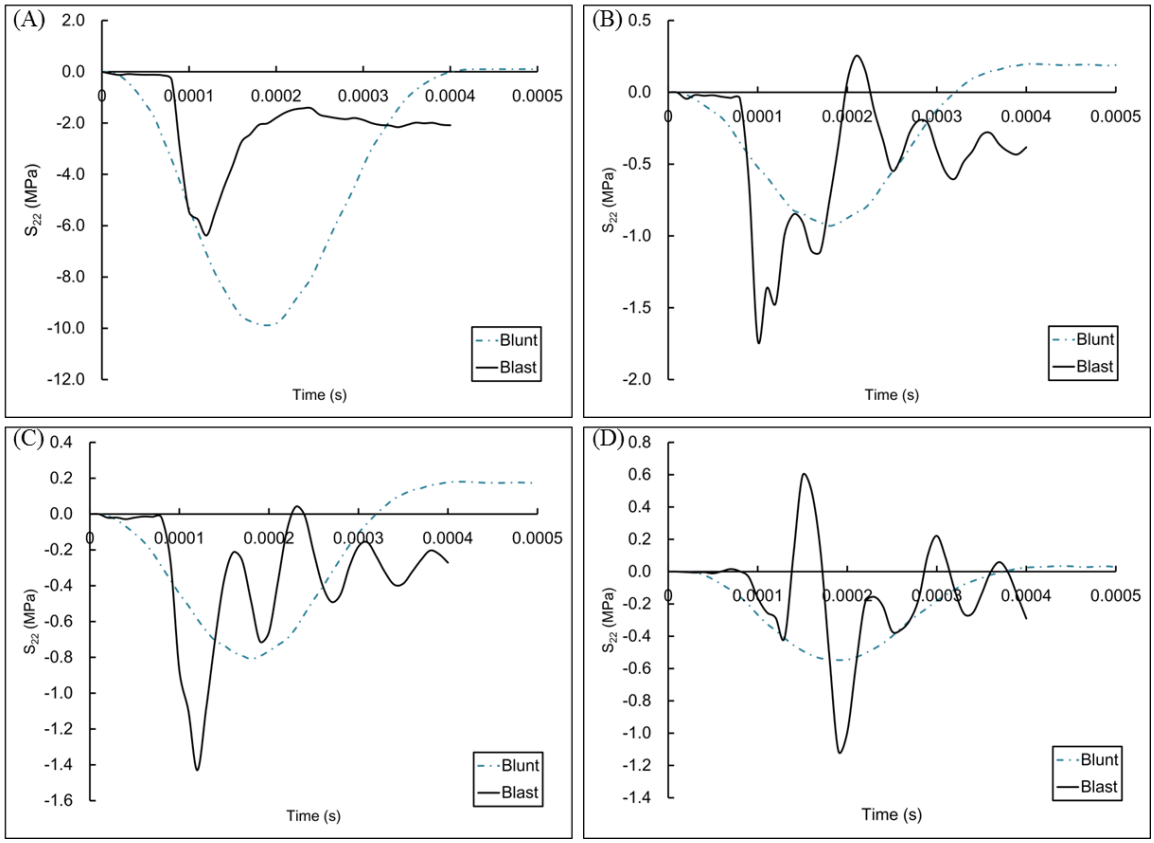

Figure 3.30 Comparison of the S22 stress components from FE simulations of blunt and blast trauma, respectively.

Notes: The four locations analyzed included the (A) skull, (B) cerebral cortex, (C) corpus callosum, and (D) hypothalamus. (C) corpus callosum, and (D) hypothalamus.

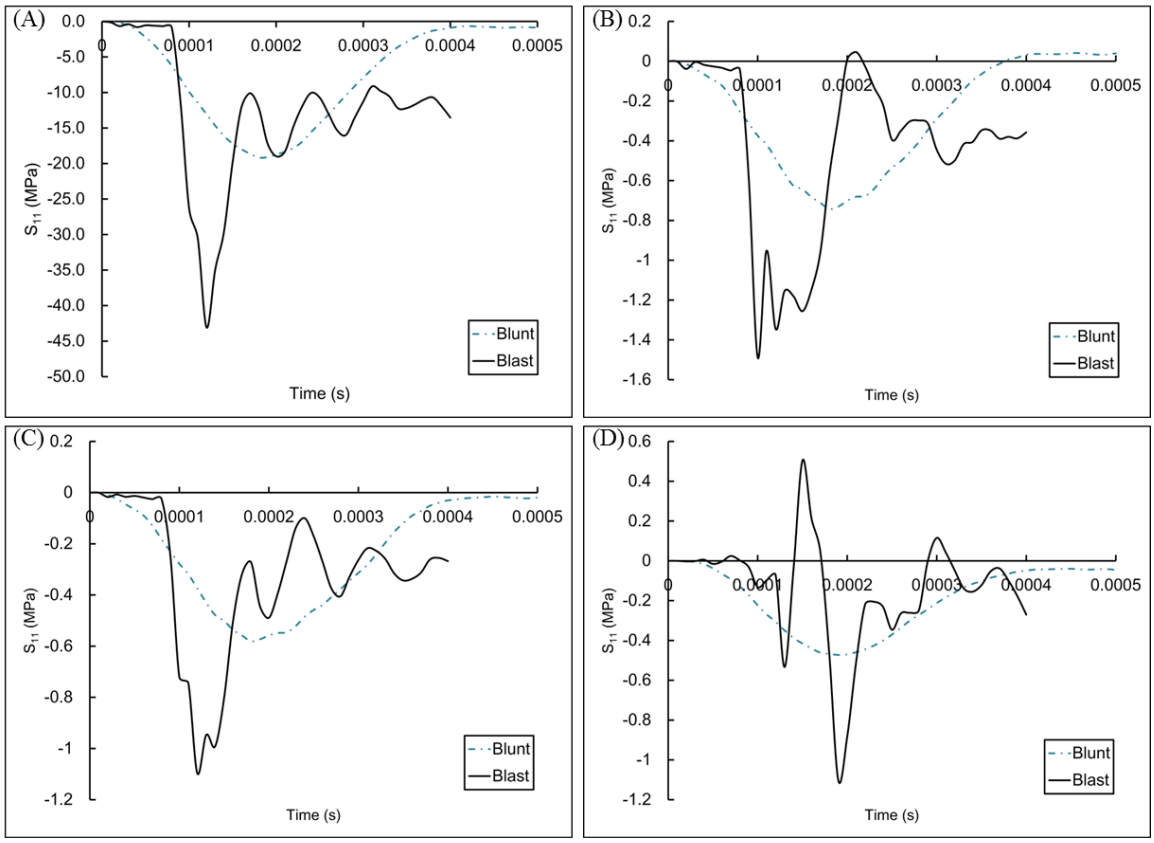

Figure 3.31 Comparison of the S11 stress components from FE simulations of blunt and blast trauma, respectively.

Notes: The four locations analyzed included the (A) skull, (B) cerebral cortex, (C) corpus callosum, and (D) hypothalamus. (C) corpus callosum, and (D) hypothalamus.

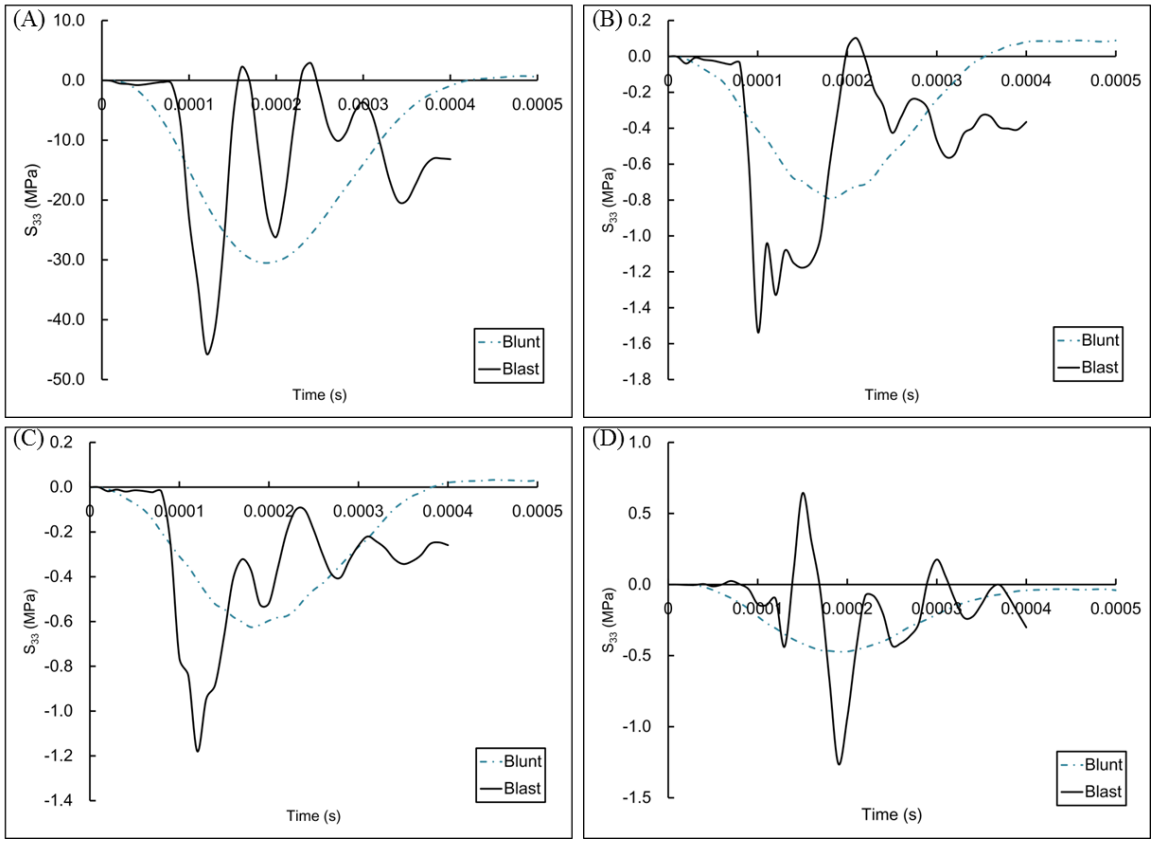

Figure 3.32 Comparison of the S33 stress components from FE simulations of blunt and blast trauma, respectively.

Notes: The four locations analyzed included the (A) skull, (B) cerebral cortex, (C) corpus callosum, and (D) hypothalamus. (C) corpus callosum, and (D) hypothalamus.

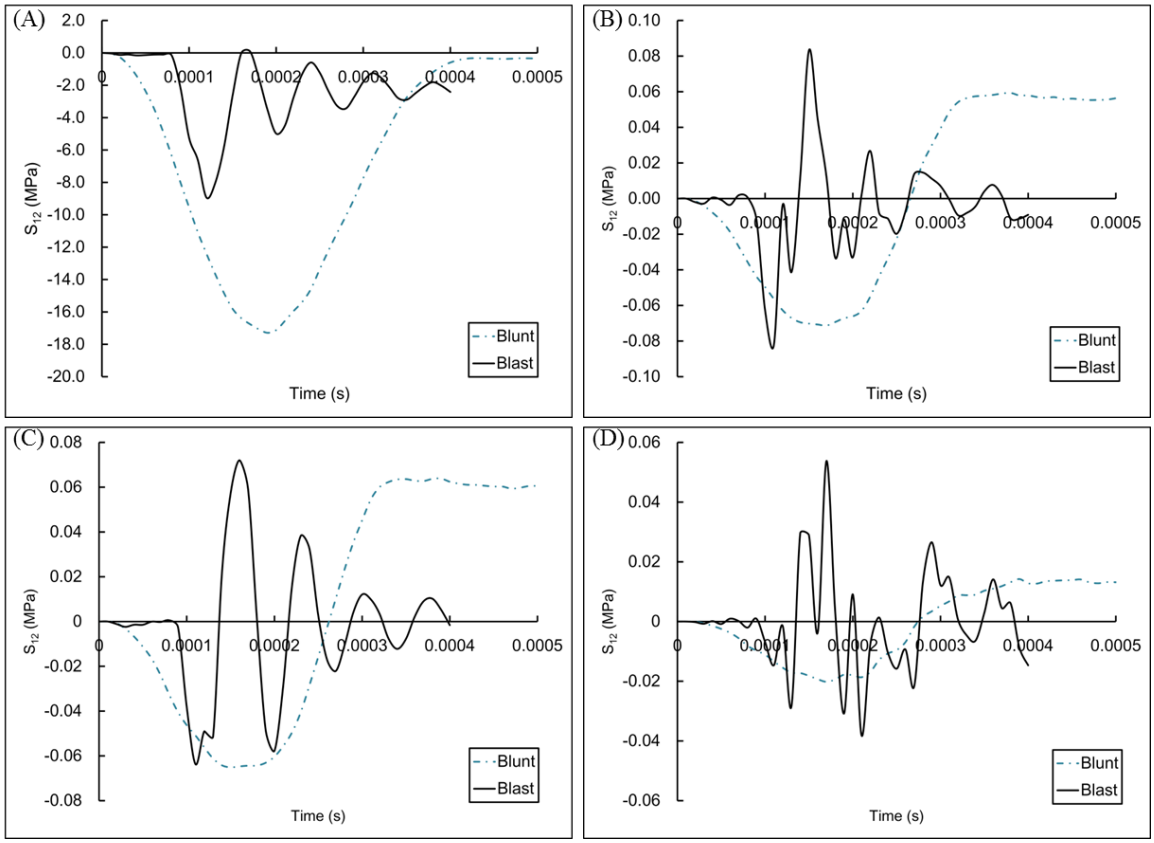

Figure 3.33 Comparison of the S12 stress components from FE simulations of blunt and blast trauma, respectively.

Notes: The four locations analyzed included the (A) skull, (B) cerebral cortex, (C) corpus callosum, and (D) hypothalamus. (C) corpus callosum, and (D) hypothalamus.

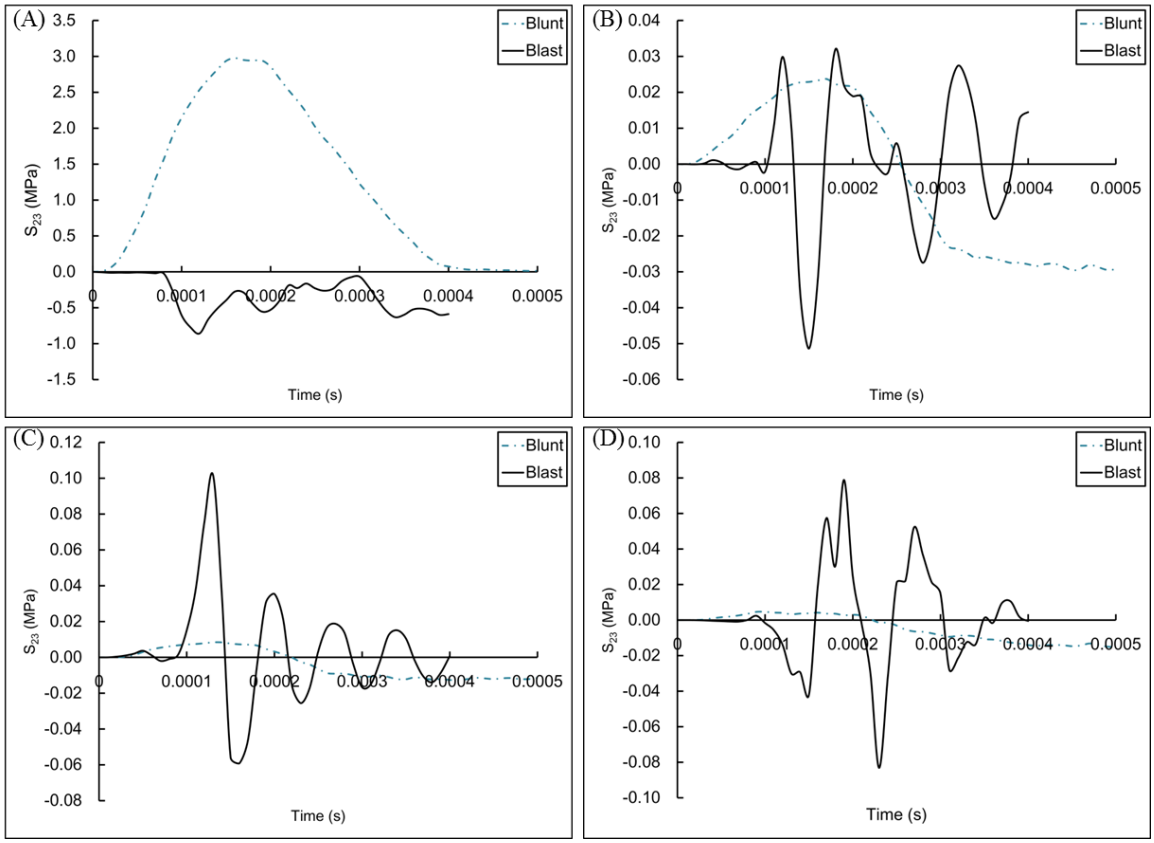

Figure 3.34 Comparison of the S23 stress components from FE simulations of blunt and blast trauma, respectively.

Notes: The four locations analyzed included the (A) skull, (B) cerebral cortex, (C) corpus callosum, and (D) hypothalamus. (C) corpus callosum, and (D) hypothalamus.

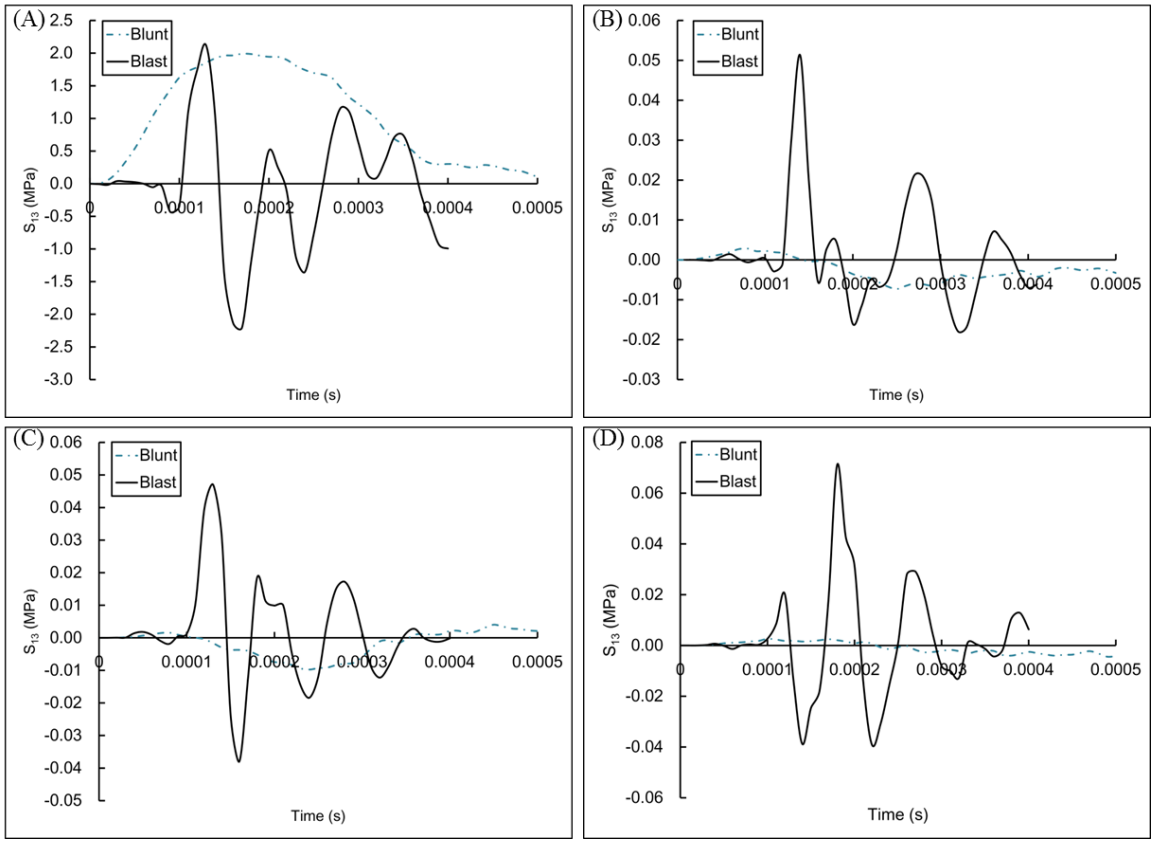

Figure 3.35 Comparison of the S13 stress components from FE simulations of blunt and blast trauma, respectively.

Notes: The four locations analyzed included the (A) skull, (B) cerebral cortex, (C) corpus callosum, and (D) hypothalamus. (C) corpus callosum, and (D) hypothalamus.

3.4 Discussion

The computational results from the mesh refinement study verified that the coarsest mesh available (i.e. Mesh #3) was suitable for generating reliable data (Figure 3.8). Slight variations in the durations of impact for all three meshes could be attributed to the proximity of the rigid impactor in relation to the head model. Although a predefined field was applied to reduce simulation time, the rigid impactor required meticulous alignment and positioning near the impact site without actually touching the

head model. For all three meshes, we positioned the rigid impactor within 0.002 mm from the outer surface of the head model, which comprised the scalp/muscle.

Experimental results were also in good agreement with FE simulation results with the pressure responses exhibiting similar trends for the blunt injury case. Differences in the overall mechanical response were still evident with the finite element analysis (FEA) plot demonstrating a more abrupt increase and subsequent decrease in pressure over time in contrast to the experimental plot (Figure 3.9). These minor differences could be linked to the respective data acquisition and data filtering procedures. Due to the short duration of impacts, both the LabVIEW virtual instrument (VI) and multifunction DAQ were programmed to collect 100,000 data points per second. This setup provided a sufficient amount of data but also produced a considerable amount of noise. Consequently, a low-pass filter was utilized to smooth the experimental data, which may have also resulted in a slightly slower response time compared to the FEA plot.

According to research by (Cullis, 2001), factors such as geometry, material properties, natural frequency, peak pressure, and impulse can influence a subsequent structural response. The geometry and material properties for the head model remained consistent for FE simulations of both blunt and blast trauma. Since the respective cumulative impulses were also equal in both injury cases, pressure became a significant metric for comparing FE results of blunt and blast trauma, respectively. Blast simulations produced overpressures that developed more quickly than in blunt simulations (Figure 3.27). This phenomenon is consistent with previous blast-related work in which investigators determined that higher pressure profiles led to a quicker onset of peak pressure (Chafi et al., 2010). In addition, the hypothalamus experienced a

fluctuating pressure response that may be attributed to its location with respect to the impact site as well as the pressure waves that propagated initially through the skull, cerebral cortex, and corpus callosum. Although these preceding head regions may have created a damping effect, the resulting out-of-phase pressures potentially propagated toward the hypothalamus to produce this initial tensile response. This finding suggests that blast trauma generates stress wave propagation with a cumulative effect in brain regions distal to the impact site.

The mechanical responses in the head were influenced differently not only by the type of injury, but also the location. Examination of the corresponding pressure in the hypothalamus indicated that blast injury generated a higher tensile response compared to blunt injury (Figure 3.27). Although the total impulse was equal in FE simulations of blunt and blast trauma, respectively, the cumulative impulse also differed mainly in the hypothalamus (Figure 3.29). These phenomena most likely occurred because the hypothalamus was distal to the outer surface of the skull (i.e. *coup* site). Consequently, the resulting stress waves propagated though this brain region but reflected inward after reaching the free surface of the hypothalamus (i.e. *countercoup* site). Additional comparisons of the normal stress components revealed that both blunt and blast trauma generated predominantly compressive responses (Figure 3.30, Figure 3.31, and Figure 3.32). However, blast trauma did produce normal stresses characterized by more oscillatory behavior. These fluctuating trends were also observed in the shear stress components within the skull and all three brain regions (Figure 3.33, Figure 3.34, and Figure 3.35). These findings indicate that both injury conditions induce compression and shear throughout all four head regions while the *countercoup* site also experienced a

subsequent tensile response. These variations in stress state, especially after blast trauma, could be sufficient to generate damage by disrupting the structural integrity of axonal fibers located throughout the white matter regions of the brain.

During blunt trauma, rotational forces generate angular accelerations that lead to the compression and shearing of brain tissue (Margulies et al., 1990; Fijalkowski et al., 2006; Fijalkowski et al., 2007; Sabet et al., 2008). However, in the absence of rotational accelerations, it is possible that blunt trauma would primarily produce focal impacts that lead to an elevated mechanical response in head regions near the coup site, which would correspond to the skull and cerebral cortex in the context of this study. Conversely, blast trauma could conceivably generate a diffuse impact that also affects brain regions distal to the coup site. Furthermore, the oscillating pressure responses created by blast trauma could induce tensile or shear stresses in the brain that could potentially be linked to complications that are often observed following TBI. For example, damage to the cerebral cortex could produce deficiencies in sustaining attention, retrieving memories, problem solving, and emotional responses. In addition, damage to the cerebellum and subcortical white matter structures (Figure 3.6) could impair coordination, memory, attention, and processing speed (McAllister, 2011)

FE simulations of blunt trauma (Figure 3.22 and Figure 3.23) and blast trauma (Figure 3.24 and Figure 3.25) revealed that the maximum principal strains were primarily found in the cerebral cortex and the corpus callosum. These locations were expected due to their proximity to the impact site, but values were relatively similar. This finding potentially indicates that maximum principal strains may be a difficult metric to utilize for studying the differential effects of blunt and blast trauma under mTBI conditions.

Previous studies have reported wide ranging thresholds for axonal strain, which include 0.05 (Margulies and Thibault, 1992), 0.21 (Kleiven, 2007), and 0.28 (Bain and Meaney, 2000). However, Bain and Meaney (2000) based their criteria from experiments on the guinea pig optic nerve. In addition, Margulies and Thibault (1992) studied moderate to severe diffuse axonal injury (DAI) in primates. Due to differences in experimental protocols, some results that have been previously reported in literature may not necessarily be comparable to the maximum principal strain reported in this study. Furthermore, this work was designed for examining the consequences of mTBI, which most likely involves experimental conditions that are less severe than work by other investigators.

3.5 Conclusions

In all four head regions, blast trauma produced von Mises stress responses that were characterized by a more fluctuating trend than in blunt trauma. Furthermore, the cerebral cortex, corpus callosum, and hypothalamus exhibited higher von Mises stresses after blast trauma while the skull exhibited a higher von Mises stress following blunt trauma. A comparison of pressure responses in all four head regions revealed that blast trauma generated higher peak pressures than blunt trauma despite equivalent total impulses. Blast trauma also produced more oscillations in the corresponding pressure responses with the hypothalamus exhibiting a tensile response. Higher values for the maximum principal strain were observed in both the cerebral cortex and corpus callosum, which could be attributed to the vicinity of these brain regions to the *coup* site.

If rotational accelerations were removed from the injury sequence, it is conceivable that blunt trauma would primarily generate focal impacts that lead to an

elevated mechanical response in head regions proximal to the *coup* site. Based on FE results, it may also be possible that blast trauma would primarily produce diffuse impacts that subsequently affect brain regions distal to the *coup* site (e.g. hypothalamus). Furthermore, blast trauma generated the normal and shear stresses characterized by fluctuating responses. While the normal stress components displayed relatively similar compressive behavior, each stress component followed unique trends at each head location. In general, the culmination of these stress states were believed to be sufficient to induce damage in brain regions that were either internal (e.g. corpus callosum) or distal (e.g. hypothalamus) to the *coup* site. Structural damage to these regions includes the disruption of axonal fibers and ultimately correlates with complications often observed following TBI.

This study focused on comparing the differential mechanical responses of the brain during blunt and blast trauma. Due to time constraints in acquiring MRI scans, the entire geometry of the rodent head could not be developed. However, MRI technicians prioritized obtaining high resolution scans of not only the brain, but the cranial tissues immediately surrounding the brain. The scanning procedure was assumed to be effective for generating a head mesh that could accurately simulate the biomechanical behavior of the brain in response to both blunt and blast trauma. This work is necessary for understanding the underlying mechanisms of mTBI since many patients are military personnel who have been exposed to IEDs and subsequently experienced blast trauma from the initial pressure wave as well as blunt trauma from ensuing head impacts. The frequency of mTBI cases highlights the need for this research, which could ultimately

lead to the development of not only enhanced protective equipment, but also updated injury thresholds and targeted pharmaceutical therapies.

3.6 References

Bain, A. and D.F. Meaney (2000). "Tissue-Level Thresholds for Axonal Damage in an Experimental Model of Central Nervous System White Matter Injury." *Journal of Biomechanical Engineering* 122(6): 615-622.

Belanger, H.G., T. Kretzmer, R.D. Vanderploeg, and L.M. French (2010). "Symptom Complaints Following Combat-Related Traumatic Brain Injury: Relationship to Traumatic Brain Injury Severity and Posttraumatic Stress Disorder." *Journal of the International Neuropsychological Society* 16: 194-199.

Belanger, H.G., T. Kretzmer, R. Yoash-Gantz, T. Pickett, and L.A. Tupler (2009). "Cognitive Sequelae of Blast-Related Versus Other Mechanisms of Brain Trauma." *Journal of the International Neuropsychological Society* 15(1): 1-8.

Bouvard, J.L., D.K. Ward, D. Hossain, E.B. Marin, D.J. Bammann, and M.F. Horstemeyer (2010). "A General Inelastic Internal State Variable Model for Amorphous Glassy Polymers." *Acta Mechanica* 213: 71-96.

Bryant, R., M. O'Donnell, and M. Creamer (2010). "The Psychiatric Sequelae of Traumatic Injury." *American Journal of Psychiatry* 167: 312-320.

Budde, M.D., L. Janes, E. Gold, L.C. Turtzo, and J.A. Frank (2011). "The Contribution of Gliosis to Diffusion Tensor Anisotropy and Tractography Following Traumatic Brain Injury: Validation in the Rat Using Fourier Analysis of Stained Tissue Sections." *Brain* 134: 2248-2260.

Carlson, K.F., S.M. Kehle, L.A. Meis, N. Greer, R. MacDonald, I. Rutks, N.A. Sayer, S.K. Dobscha, and T.J. Wilt (2011). "Prevalence, Assessment, and Treatment of Mild Traumatic Brain Injury and Posttraumatic Stress Disorder: A Systematic Review of the Evidence." *Journal of Head Trauma Rehabilitation* 26(2): 103-115.

Carlson, K.F., D. Nelson, R.J. Orazem, S. Nugent, D.X. Cifu, and N.A. Sayer (2010). "Psychiatric Diagnoses Among Iraq and Afghanistan War Veterans Screened for Deployment-Related Traumatic Brain Injury." *Journal of Traumatic Stress* 23: 17-24.

Cernak, I. and L.J. Noble-Haeusslein (2010). "Traumatic Brain Injury: An Overview of Pathobiology with Emphasis on Military Populations." *Journal of Cerebral Blood Flow & Metabolism* 30, 255-266.

Chafi, M.S., G. Karami, and M. Ziejewski (2010). "Biomechanical Assessment of Brain Dynamic Responses Due to Blast Pressure Waves." *Annals of Biomedical Engineering* 38(2): 490-504.

Cullis, I.G. (2001). "Blast Waves and How They Interact with Structures." *Journal of the Royal Army Medical Corps* 147(1): 16-26.

Elder, G.A. and A. Cristian (2009). "Blast-Related Mild Traumatic Brain Injury: Mechanisms of Injury and Impact on Clinical Care." *Mount Sinai Journal of Medicine* 76: 111-118.

Fijalkowski, R.J., B.M. Ellingson, B.D. Stemper, N. Yoganandan, T.A. Gennarelli, and F.A. Pintar (2006). "Interface Parameters of Impact-Induced Mild Traumatic Brain Injury." *Biomedical Sciences Instrumentation* 42: 108-113.

Fijalkowski, R.J., B.D. Stemper, F.A. Pintar, N. Yoganandan, and T.A. Gennarelli (2007). "Biomechanical Correlates of Mild Diffuse Brain Injury in the Rat." *Biomedical Sciences Instrumentation* 43: 18-23.

Hicks, R.R., S.J. Fertig, R.E. Desrocher, W.J. Koroshetz, and J.J. Pancrazio (2010). "Neurological Effects of Blast Injury." *Journal of Trauma and Acute Care Surgery* 68(5): 1257-1263.

Hoge, C.W., D. McGurk, J.L. Thomas, A.L. Cox, C.C. Engel, and C.A. Castro (2008). "Mild Traumatic Brain Injury in U.S. Soldiers Returning from Iraq." *New England Journal of Medicine* 358: 453-463.

Kleiven, S. (2007). "Predictors for Traumatic Brain Injuries Evaluated Through Accident Reconstructions." *Stapp Car Crash Journal* 51: 81-114.

Levin, H.S., E. Wilde, M. Troyanskaya, N.J. Peterson, R. Scheibel, M. Newsome, M. Radaideh, T. Wu, R. Yallampalli, Z. Chu, and X. Li (2010). "Diffusion Tensor Imaging of Mild to Moderate Blast-Related Traumatic Brain Injury and Its Sequelae." *Journal of Neurotrauma* 27(4): 683-694.

Ling, G., F. Bandak, R. Armonda, G. Grant, and J. Ecklund (2009). "Explosive Blast Neurotrauma." *Journal of Neurotrauma* 26: 815-825.

MacGregor, A.J., A.L. Dougherty, R.H. Morrison, K.H. Quinn, and M.R. Galarneau (2011). "Repeated Concussion Among U.S. Military Personnel During Operation Iraqi Freedom." *Journal of Rehabilitation Research & Development* 48(10): 1269-1278.

Margulies, S. and R. Hicks (2009). "Combination Therapies for Traumatic Brain Injury: Prospective Considerations." *Journal of Neurotrauma* 26, 925-939.

Margulies, S.S. and L.E. Thibault (1992). "A Proposed Tolerance Criterion for Diffuse Axonal Injury in Man." *Journal of Biomechanics* 25(8): 917-923.

Margulies, S.S., L.E. Thibault, and T.A. Gennarelli (1990). "Physical Model Simulations of Brain Injury in the Primate." *Journal of Biomechanics* 23: 823-836.

McAllister, T.W. (2011). "Neurobiological Consequences of TBI." *Dialogues in Clinical Neuroscience* 13(3): 287-300.

McCrory, P., W. Meeuwisse, K. Johnston, J. Dvorak, M. Aubry, M. Molloy, and R. Cantu (2009). "Consensus Statement on Concussion in Sport – The 3rd International Conference on Concussion in Sport held in Zurich, November 2008." *Journal of Clinical Neuroscience* 16(6): 755-763.

Prabhu, R., M.F. Horstemeyer, M.T. Tucker, E.B. Marin, J.L. Bouvard, J.A. Sherburn, J. Liao, and L.N. Williams (2011). "Coupled Experiment/Finite Element Analysis on the Mechanical Response of Porcine Brain under High Strain Rates." *Journal of the Mechanical Behavior of Biomedical Materials* 4: 1067-1080.

Sabet, A.A., E. Christoforou, B. Zatlin, G.M. Genin, and P.V. Bayly (2008). "Deformation of the Human Brain Induced by Mild Angular Head Acceleration." *Journal of Biomechanics* 41(2): 307-315.

Schneiderman, A., E. Braver, and H. Kang (2008). "Understanding Sequelae of Injury Mechanisms and Mild Traumatic Brain Injury Incurred During the Conflicts in Iraq and Afghanistan: Persistent Postconcussive Symptoms and Post-Traumatic Stress Disorder." *American Journal of Epidemiology* 167: 1446-1452.

Simulia (2010). *Abaqus 6.10 Online Documentation*. Providence, RI, Dassault Systemes Simulia Corp.

CHAPTER IV

STRESS STATE DEPENDENCE IN THE PORCINE BRAIN

4.1 Introduction

Studies on the mechanical characterization of soft biological tissues (e.g. skin, lungs, kidneys, brain) have shown that soft tissues exhibit behavior that is generally classified as nonlinear, anisotropic, and viscoelastic. In recent years, researchers have focused their attention on traumatic brain injury (TBI), which causes focal or diffuse damage and leads to symptoms that are mild to severe depending on injury extent. Investigators have subsequently created detailed finite element (FE) models of the human head to examine the internal mechanical response under various loading conditions (Horgan and Gilchrist, 2003; Takhounts et al., 2008; Ho and Kleiven, 2009). However, the accuracy of these FE models depends on the material properties assigned, which are based on experimental results (Rashid et al., 2012). Since the brain exhibits a compressive, tensile, and shear response during trauma, numerous research groups have performed a variety of experiments to investigate its mechanical properties.

Many researchers have studied the mechanical response of brain under a wide range of testing conditions in an effort to define the corresponding constitutive properties. Common experimental methods reported in literature include unconfined compression (Miller and Chinzei, 1997; Prange and Margulies, 2002; Cheng and Bilston, 2007; Tamura et al., 2007) and oscillatory shear testing (Donnelly and Medige, 1997; Arbogast

and Margulies, 1998; Darvish and Crandall, 2001; Brands et al., 2004; Nicolle et al., 2004; Hrapko et al., 2006). By comparison, fewer investigators have performed tension tests on the brain (Miller and Chinzei, 2002; Hrapko et al., 2006; Velardi et al., 2006). Thus, research focused on examining the stress state dependent response of the brain could be beneficial toward identifying the underlying mechanisms of TBI.

Due to ethical concerns and experimental limitations, researchers often resort to in vitro testing of animal brains (e.g. primate, porcine, bovine, murine). Previous studies report that primate brains possess shear, storage, and loss moduli that are 1.5, 1.4, and 2 times higher, respectively, than humans (Galford and McElhaney, 1970). Furthermore, primate brains demonstrated only a slightly stiffer mechanical response than human brains when exposed to similar strain rates (Estes and McElhaney, 1970). Although porcine brain has been reported to be 1.3 times stiffer than human brain (Prange et al., 2000), other researchers have suggested that the mechanical properties between human and porcine brain do not differ (Nicolle et al., 2004). Following dynamic in vitro experiments, researchers also determined that brains from different animals (e.g. porcine, bovine, caprine), breeds, and genders were not significantly different (Pervin and Chen, 2011). Based on previous brain comparisons, the porcine brain was considered to be a suitable surrogate for the human brain.

During head impacts, the brain experiences a combination of compression, tension, and shear. This multiaxial stress state can occur due to the substantial water content (~80% wt/wt) in the brain parenchyma, especially during high strain rate deformation (Prabhu et al., 2011). This phenomenon can also be attributed to the complex microstructure of the brain, which consists of gray matter and white matter with

each region possessing distinct microstructural components and inherent mechanical properties. For instance, gray matter comprises neuronal cell bodies that are distributed throughout the surface of the cerebral cortex without any directional preference. White matter consists of axon bundles, or myelinated nerve cell processes, that possess a more highly oriented structure than gray matter. While gray matter is typically considered to be isotropic, white matter is generally characterized as anisotropic (Arbogast and Margulies, 1999; Nicolle et al., 2004). Diffuse axonal injury (DAI) occurs when axons experience shearing during TBI. As a result, many researchers have conducted studies to identify the strain rates and strains that lead to DAI. Previous research suggests that macroscopic shear strains of 0.10-0.50 and strain rates of 10-50 s^{-1} are sufficient to induce DAI (Margulies et al., 1990). An in vivo study on the guinea pig optic nerve reported that the strains necessary for axonal injury were between 0.13 and 0.34 (Bain and Meaney, 2000). In studies on cultured brain cells, investigators claimed that strain rates greater than 10 s^{-1} and strains greater than 0.10 were sufficient to produce extensive damage (Morrison III et al., 2000; Morrison III et al., 2006). Due to the heterogeneous properties of the brain, further study is needed to link the effects of multiaxial stress states within the brain to conditions consistent with TBI.

In recent decades, internal state variable (ISV) theory has been utilized to achieve major advances in numerous applications such as failure analysis and the redesign of structural components. An ISV model is a constitutive model that can predict the mechanical properties of a material based on its comprehensive mechanical loading history. They can capture not only the elastic properties of a material but also inelastic properties such as viscoelasticity and viscoplasticity. Furthermore, ISV models for

various engineering materials have been modified to incorporate corresponding phenomena such as strain rate dependence, stress state dependence, and damage (Bouvard et al., 2010). For example, researchers examined the link between stress state and damage evolution in aluminum cast alloys and subsequently derived the hardening rate equations needed to identify the failure strains for compression, tension, and torsion (Horstemeyer et al., 2000). In addition, researchers recently developed a generalized ISV model from amorphous polymers, which was capable of predicting the mechanical response over a multitude of strain rates (Bouvard et al., 2010). ISV concepts have previously been applied to polymers, metal alloys, and ceramics, but recent work has applied this paradigm toward soft biological tissues. For instance, researchers developed structure-property relations for porcine brain tissue by correlating the strain rate dependent compressive response to the internal microstructure at different levels of strain (Begonia et al., 2010). Similarly, researchers have investigated both the strain rate and the stress state dependence of human placenta by analyzing the mechanical response of the tissue under compression, tension, and shear and subsequently quantifying the corresponding histological changes (Weed et al., 2012). Using ISV principles, researchers can further enhance an existing constitutive model by integrating damage parameters and deducing evolution equations, which can lead to a more detailed characterization of a material's mechanical properties.

FE simulations are effective for determining injury thresholds at varying TBI severities. However, the corresponding constitutive models could still be enhanced with more accurate material properties and depictions of the internal microstructure (Wright and Ramesh, 2012). One method for producing a more realistic (i.e. biofidelic)

constitutive model is to incorporate the arrangement of neuron and glial cells within the brain under multiple stress states compared to the uninjured state. Quantification of the corresponding microstructural changes combined with the characteristic mechanical response would allow researchers to eventually develop a more biofidelic brain model with higher predictive capabilities for TBI. In the present study, structure-property relationships were determined for porcine brain after completing interruption compression, tension, and shear experiments at a strain rate of 0.1 s^{-1}. For each stress state, in-house image analysis software was utilized to quantify the microstructural changes in brain sections stained with Hematoxylin and Eosin (H&E) at strains of 0.15, 0.30, and 0.40.

4.2 Methods

4.2.1 Sample Preparation

The extraction and dissection procedures required approximately one hour for completion, and all interruption mechanical testing was performed within three hours post-mortem. All experiments followed the protocol approved by the Office of Regulatory Compliance and Safety (ORSC) at Mississippi State University. Brains were obtained from healthy male pigs that were 22-26 weeks old and weighed 240-270 lbs. Brains were temporarily stored in 0.01 M phosphate buffered saline (Sigma-Aldrich, St. Louis, MO) to prevent dehydration and minimize tissue degradation. Before test samples could be procured, an incision was made along the longitudinal fissure to separate the left and right hemispheres. For compression and tension experiments, a stainless steel die was used for collecting cylindrical test samples in which the upper surface could be identified by the sulci and gyri from the cerebral cortex (Figure 4.1 A). The initial height

and initial diameter of cylindrical test samples were 15 mm and 30 mm, respectively. For shear experiments, rectangular test samples with dimensions 40 x 10 x 10 mm were collected from each hemisphere (Figure 4.1 B).

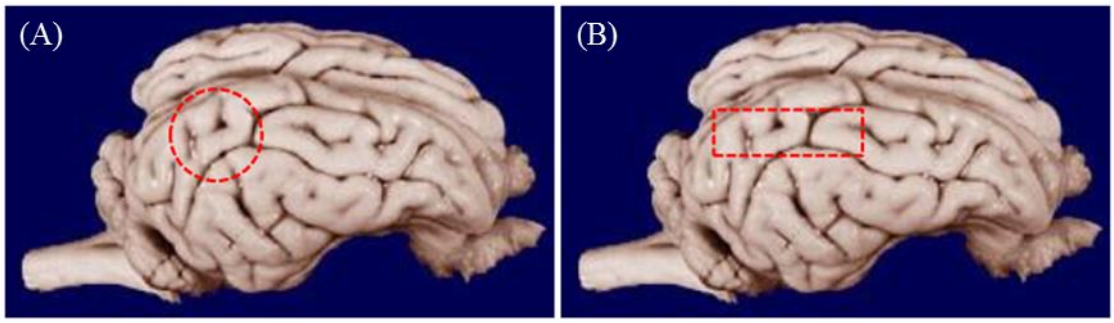

Figure 4.1 Geometry and location of samples for (A) compression/tension and (B) shear.

Notes: (A) Standard extraction location and orientation for samples procured for compression and tension experiments. (b) Standard extraction location and orientation for samples procured for shear experiments.

4.2.2 Testing System

The MACH-1^{TM} Micromechanical Testing System (BIOMOMENTUM Biomaterials and Cartilage Testing Solutions, Laval, QC, Canada) was used in all experiments. A 1 kg load cell with an error level of ± 0.00005 kg was selected for this study because its sensitivity was preferable in measuring the mechanical response of the porcine brain. The initial heights of test samples were determined by the Find Contact command in the MACH-1^{TM} programming. The sequence managing window was then used for configuring experimental parameters such as the strain distance (mm) and loading velocity (mm/s) while both the actuator control and real-time display windows were utilized for running experiments. The actuator control window enabled manual positioning of the platen prior to testing, and the real-time display window monitored the

fluctuations in the load (g) and the vertical position (mm) during testing. The compression and tension experimental setup utilized a 50 mm detachable circular platen and a chamber capable of housing 0.01 M PBS during testing (Figure 4.2 A). The shear experimental setup utilized a detachable shear platen and a custom plate that could be mounted onto an adjustable test stand (Figure 4.2 B).

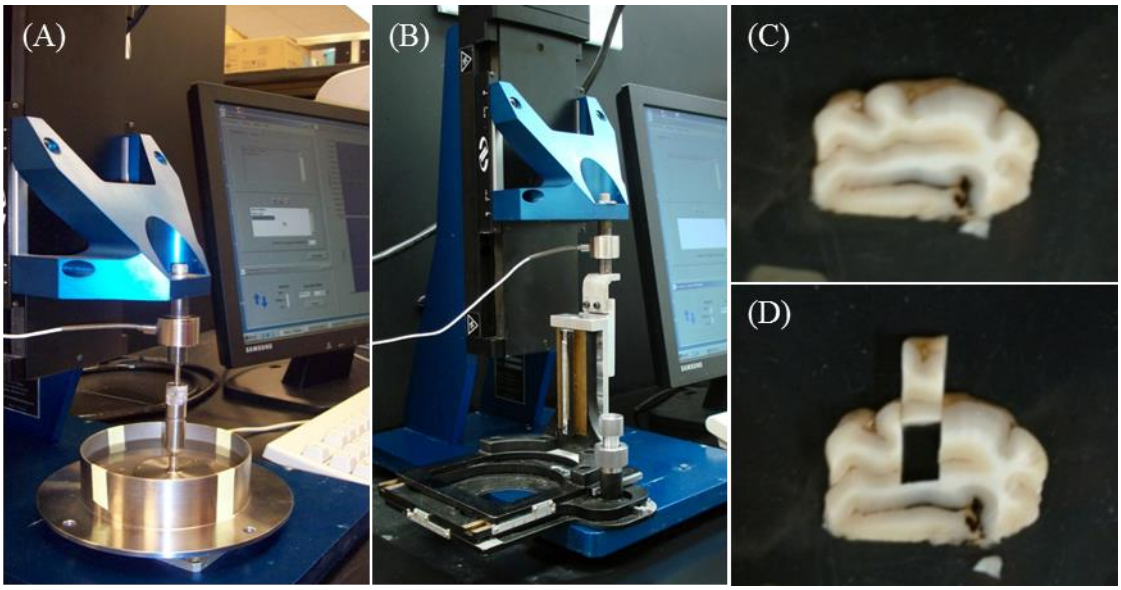

Figure 4.2 Diagram showing the (A,B) experimental setup and (C,D) histological processing.

Notes: MACH-1™ Micromechanical Testing System configured for (A) compression and tension experiments and (B) shear experiments. (C, D) Sectioning procedure of formalin-fixed brain samples for histological processing.

4.2.3 Testing Protocol

Interruption testing is a method of mechanical testing in which multiple groups of experiments are performed at a consistent strain rate but to different strains depending on the group assigned. When the stress-strain responses from each group are superimposed, the overall mechanical behavior of the material should be captured. Compression,

tension, and shear experiments were performed at a strain rate of 0.1 s^{-1} and to strains of 0.15, 0.30, and 0.40 in this study.

For compression experiments, cyanoacrylate was applied to the lower surface of each test sample to maintain a no-slip boundary condition. For tension experiments, cyanoacrylate was applied to the upper and lower surface of each test sample to maintain sufficient tissue adhesion throughout testing. For shear experiments, cyanoacrylate was used to secure each test sample to both the shear platen and the custom mounting plate. Test samples were hydrated with 0.01 M PBS during testing and then immersed in 10% neutral buffered formalin (NBF) for tissue fixation.

The initial heights of test samples in both compression and tension experiments were measured within mm using a custom programming sequence in the MACH-1™ Micromechanical Testing System. From a preset height, the circular platen lowered its vertical position until it registered a contact load of 0.5 g with the upper surface of the test sample. At this stopping point, the height of the test sample was determined and then used to calculate the corresponding loading velocity (mm/s) and strain distance (mm). For shear experiments, calipers were used to measure the average thickness from three locations along each test sample before the corresponding loading velocity and strain distance could be calculated.

4.2.4 Histological Processing

Each test sample remained in 10% NBF for 7 days prior to histological processing. Minimal tissue relaxation was anticipated and considered to be uniform for all test samples since the fixation process occurred in a consistent manner. Brain sections were collected from a region predominantly comprising the cerebral cortex (Figure 4.2 C

and Figure 4.2 D). This extraction site was selected because it captured the internal microstructure of the tissue during mechanical testing. Furthermore, this region of the test sample effectively illustrated the subtle deformations in the arrangement of microstructural components including the neurons and glial cells.

Tissue sections were rinsed in distilled water and dehydrated in a graded ethanol series. Afterward, they were infiltrated and embedded in Paraplast Plus (Oxford Labware, St. Louis, MO) using CitriSolve (Fisher Scientific, Houston, TX) as a transitional fluid. Multiple 5 μm sections were cut using an American Optical 820 rotary microtome (Fisher Scientific, Houston, TX) and mounted onto slides. Slides were deparaffinized using CitriSolve and a graded ethanol series and then stained with Hematoxylin and Eosin (H&E).

4.2.5 Quantitative Microstructural Analysis

All images were acquired with a LEICA DM2500 microscope at an objective magnification of 10X (Leica Microsystems Inc., Buffalo Grove, IL). The total analysis area for each image was 1.8 x 105 μm^2. In-house image analysis software (ImageAnalyzer Ver. 2.2-0, CAVS, Mississippi State University) was utilized for this study. This GUI provides analysis parameters that are designed for integration with a constitutive, or material, model that can be modified to include specific damage criteria. The area fraction and nearest neighbor distance (μm) were the quantitative parameters used to characterize the distribution of neurons and glial cells under different stress states and at different strains. The area fraction is defined as the area occupied by neurons and glial cells divided by the total image area. The nearest neighbor distance quantified the space separating the centroids of every neuron and glial cell examined by the GUI. After

converting images from RGB to grayscale intensity, the GUI analyzed images based on the minimum object area and threshold range. Fig. 3 summarizes the image analysis procedure for an H&E stained brain section from the uninjured state.

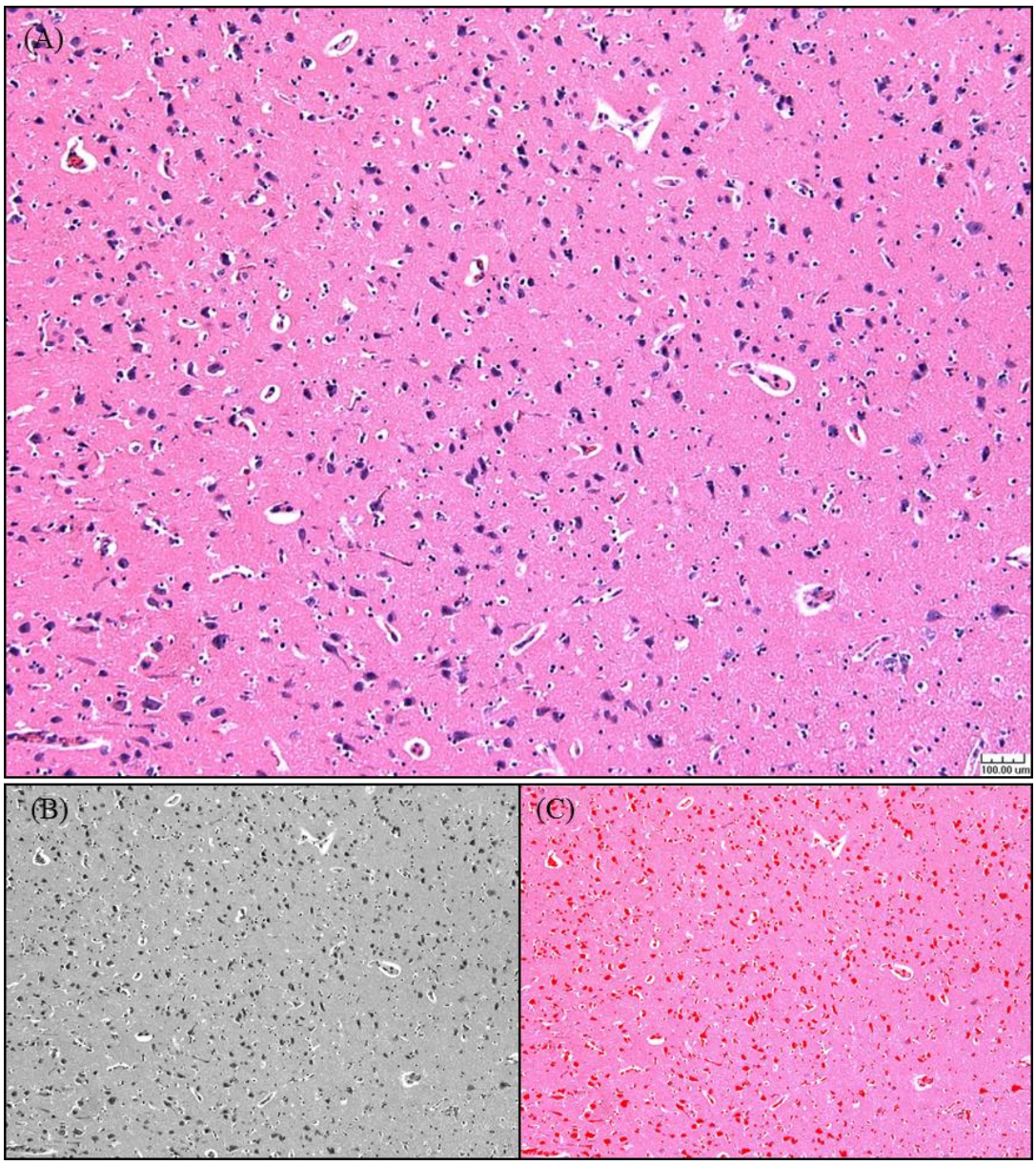

Figure 4.3 Pre- and post-processing results from ImageAnalyzer Ver. 2.2-0, which shows the (A) RGB image, (b) grayscale image, and (c) analyzed image.

Notes: The neurons and glial cells detected by the GUI are highlighted red.

4.3 Results

4.3.1 Mechanical Response

Variations in the mechanical behavior of porcine brain were observed under different stress states. Porcine brain exhibited a nonlinear mechanical response during compression, which was characterized by increased stiffening as the strain progressed to 0.40. Tangent moduli of 6.0, 14.1, and 20.2 kPa were determined at strains of 0.15, 0.30, and 0.40, respectively, and subsequently confirmed that the stiffness increased over time (Figure 4.4). While in tension, porcine brain demonstrated initial stiffening up to a strain of 0.05 and then displayed gradual softening as the strain increased to 0.40. Porcine brain also produced a yield stress and Young's modulus of 80.9 and 1.55 kPa, respectively, under tensile conditions (Figure 4.5). Under shear conditions, porcine brain exhibited a mechanical response that gradually stiffened as the strain increased. However, softening occurred at a strain of approximately 0.37 (Figure 4.6). Stress states were also compared at the same strain rate (0.1 s^{-1}) at a strain (0.40). The corresponding von Mises stresses for compression, tension, and shear were 3575.15, 335.32, and 553.94, respectively. Based on these results, porcine brain experienced compressive stresses that were 10.6% higher than the tensile stress and 6.5% higher than the shear stress (Figure 4.7).

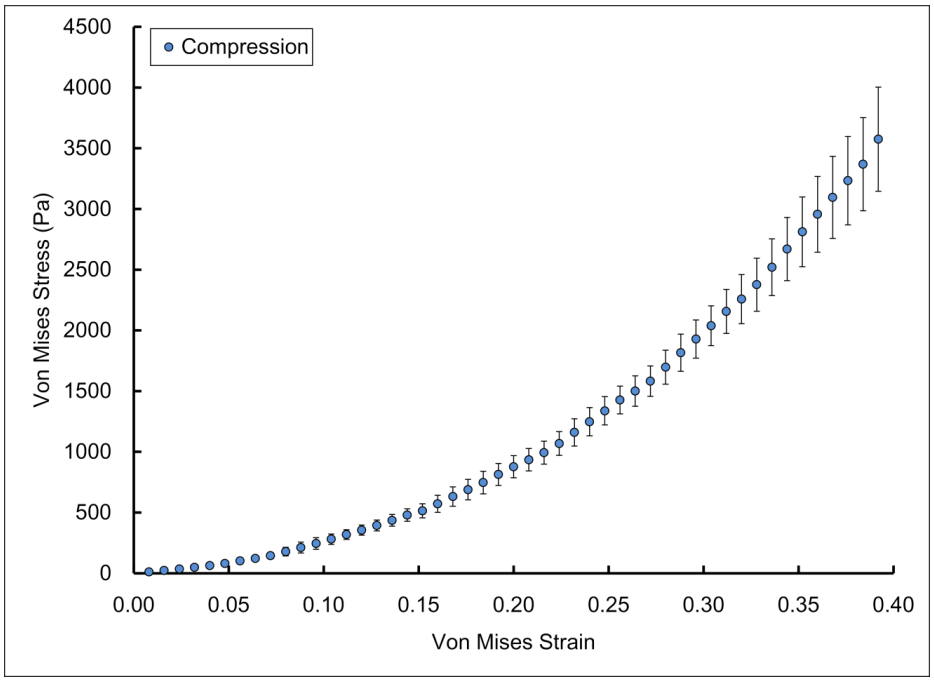

Figure 4.4 Compressive response of porcine brain at a strain rate of 0.1 s^{-1} (n = 9).

Note: Error bars represent standard deviations.

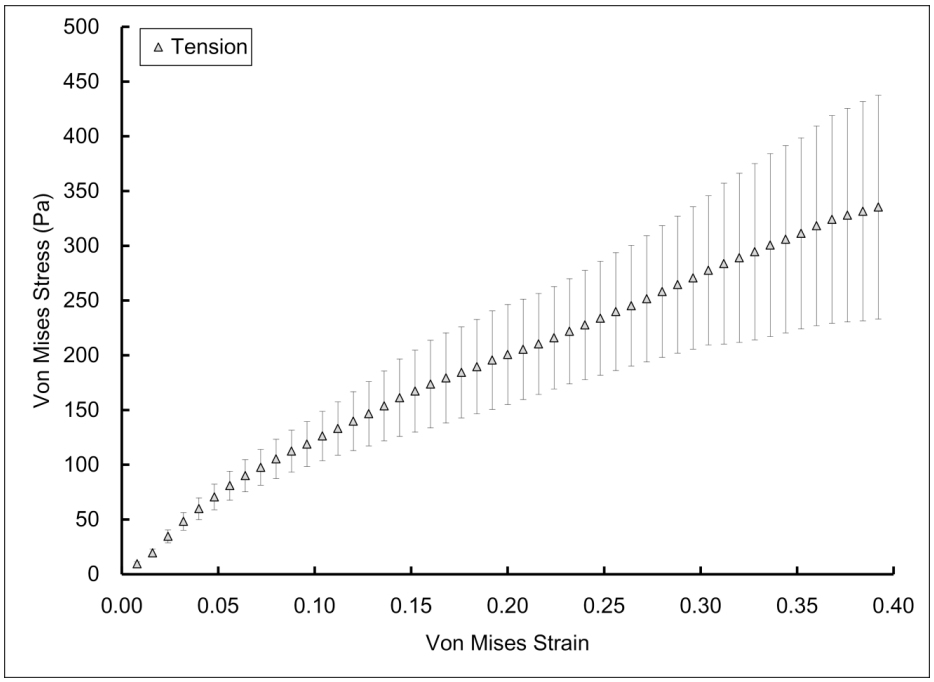

Figure 4.5 Tensile response of porcine brain at a strain rate of 0.1 s^{-1} (n = 12).

Note: Error bars represent standard deviations.

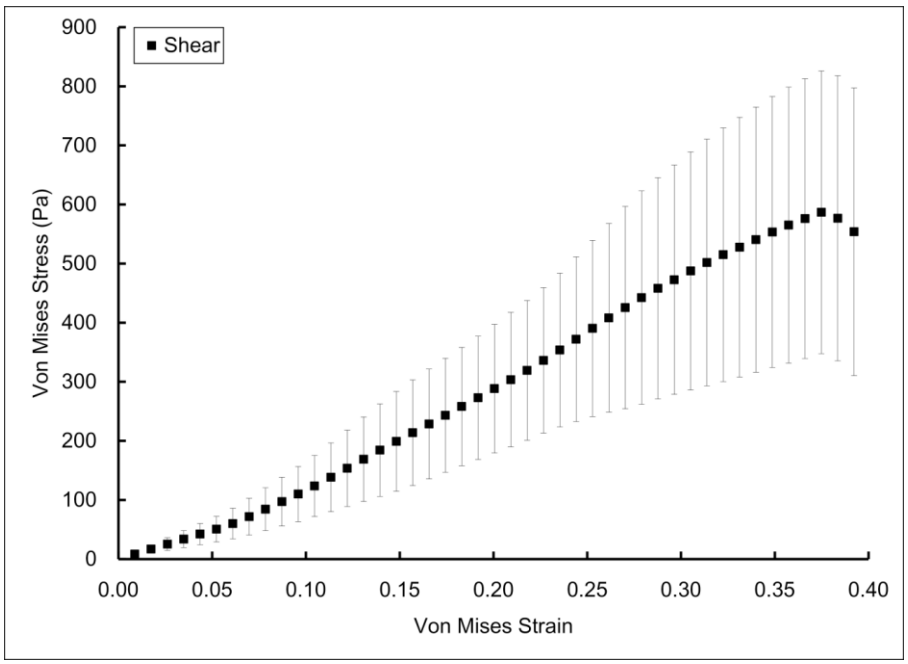

Figure 4.6 Shear response of porcine brain at a strain rate of 0.1 s^{-1} (n = 10).

Note: Error bars represent standard deviations.

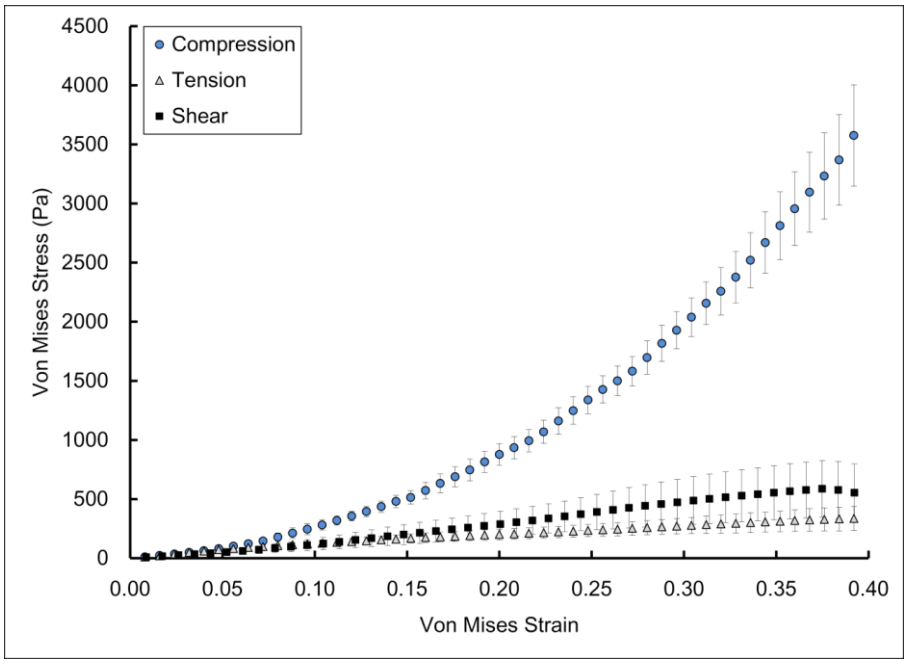

Figure 4.7 Comparison of the compressive, tensile, and shear response of porcine brain at a strain rate of 0.1 s^{-1}.

Note: Error bars represent standard deviations.

4.3.2 Microstructural Response

Variations in the internal microstructure of porcine brain were observed under compression (Figure 4.8), tension (Figure 4.9), and shear (Figure 4.10). Consequently, both the area fraction and the nearest neighbor distance displayed noticeable trends. During compression, porcine brain exhibited area fractions that subsequently increased as the strain progressed to 0.40. Conversely, porcine brain produced a gradually decreasing area fraction under tension and shear, respectively. Table 4.1 summarizes the area fractions for porcine brain for compression, tension, and shear at strains of 0.15, 0.30, and 0.40 while Figure 4.11 shows a plot of area fraction as a function of the von Mises strain. The nearest neighbor distance also followed specific trends based on the stress state applied. For example, porcine brain exhibited a steady decrease in the nearest neighbor distance as the strain progressed. However, both tension and shear led to corresponding increases in the nearest neighbor distance for porcine brain. Table 4.2 summarizes the nearest neighbor distances according to stress state and strain while Figure 4.12 provides a plots of nearest neighbor distance, respectively as a function of the von Mises strain.

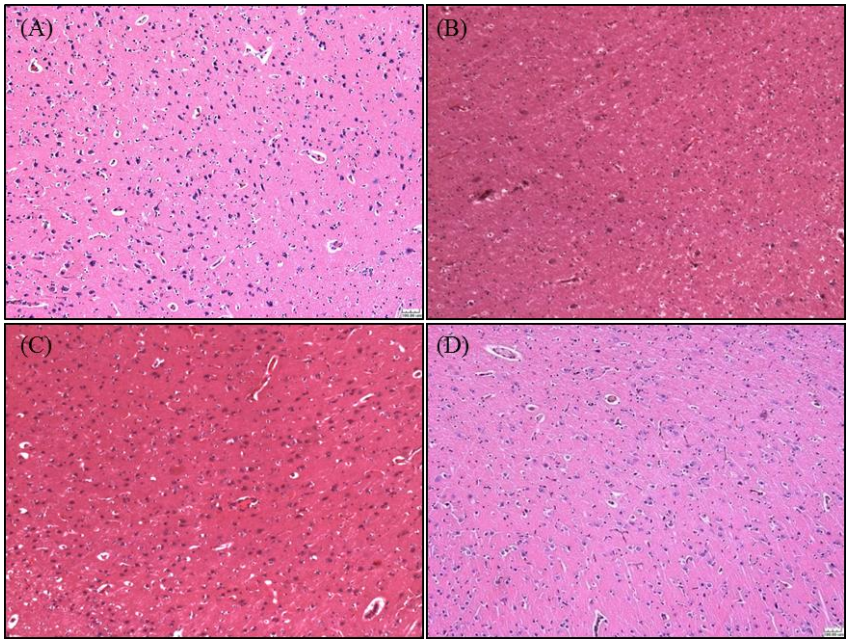

Figure 4.8 Representative microstructure for porcine brain after compressive interruption testing

at strains of (A) 0, (B) 0.15, (C) 0.30, and (4) 0.40.

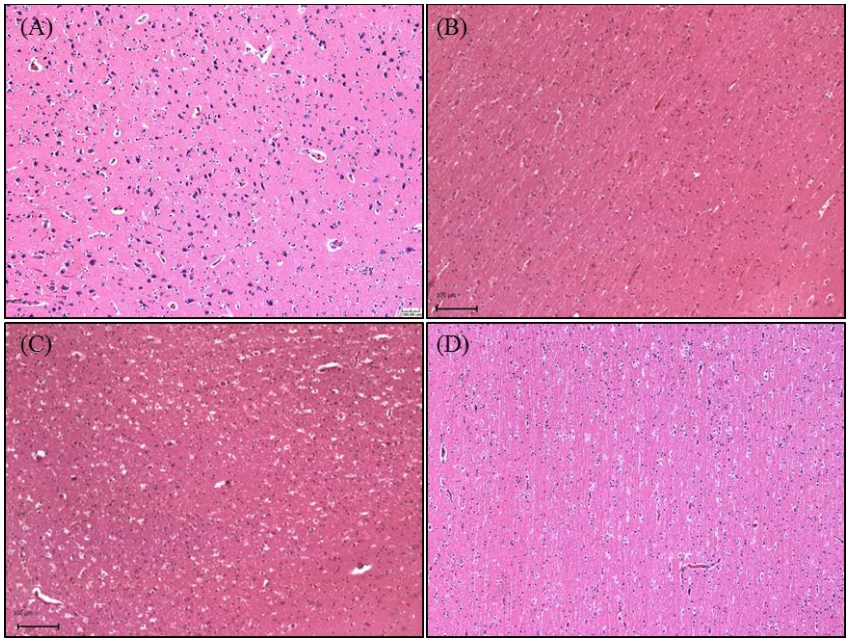

Figure 4.9 Representative microstructure for porcine brain after tensile interruption testing

at strains of (A) 0, (B) 0.15, (C) 0.30, and (4) 0.40.

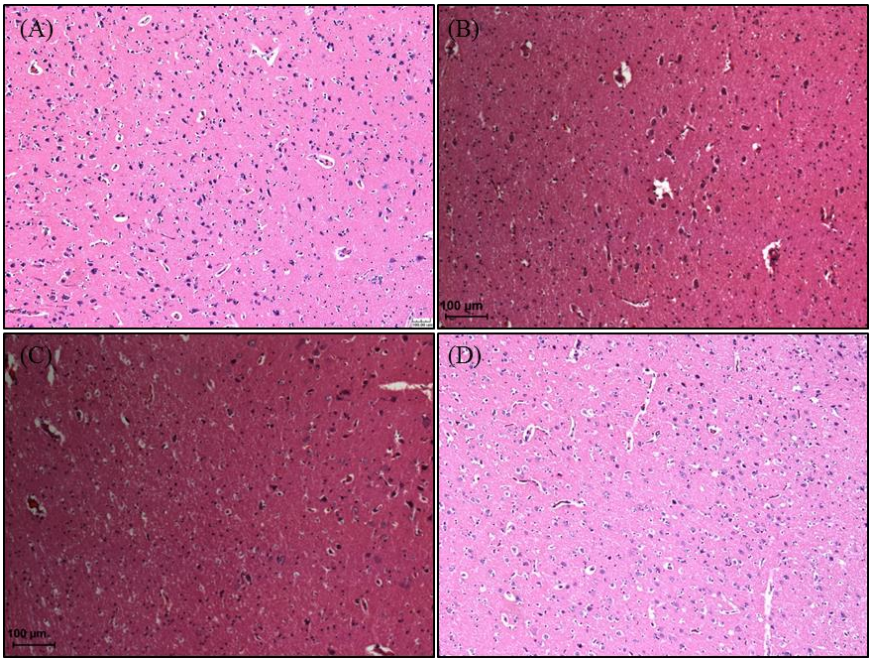

Figure 4.10 Representative microstructure for porcine brain after shear interruption testing

at strains of (A) 0, (B) 0.15, (C) 0.30, and (4) 0.40.

Table 4.1 Area fractions according to strain and stress state (Mean ± SD).

Strain	Compression	Tension	Shear
0	3.51 ± 0.34		
0.15	4.74 ± 0.82	2.89 ± 0.36	2.76 ± 0.21
0.30	6.43 ± 0.31	1.64 ± 0.51	2.04 ± 0.09
0.40	6.69 ± 0.77	1.05 ± 0.33	1.53 ± 0.34

Table 4.2 Nearest neighbor distances according to strain and stress state (Mean ± SD).

Strain	Compression	Tension	Shear
0	11.15 ± 0.39		
0.15	10.26 ± 0.67	10.28 ± 0.86	10.86 ± 1.21
0.30	8.79 ± 0.41	12.53 ± 1.28	11.90 ± 0.82
0.40	4.40 ± 0.75	14.96 ± 2.25	13.59 ± 0.97

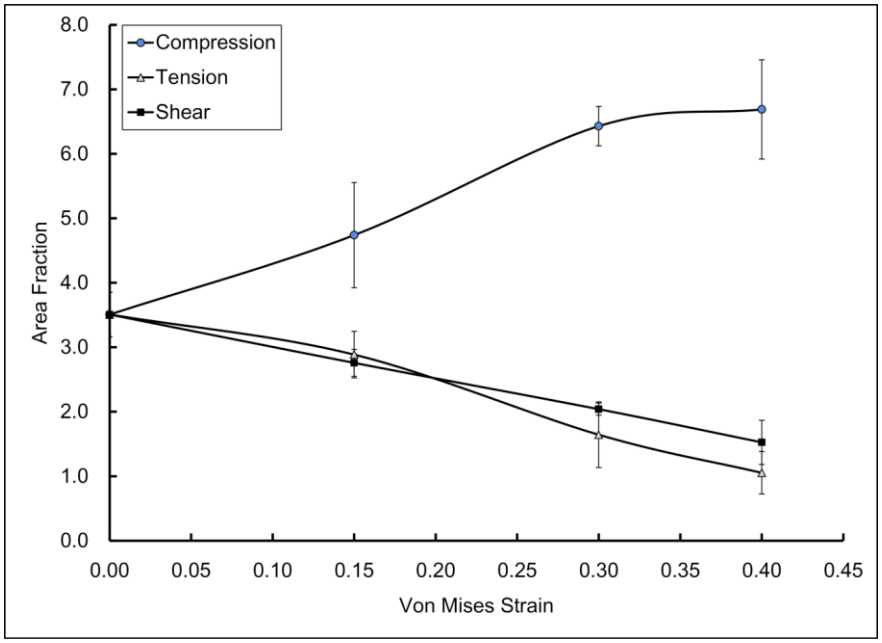

Figure 4.11 Area fraction comparison for porcine brain under different stress states and strains.

Note: Error bars represent standard deviations.

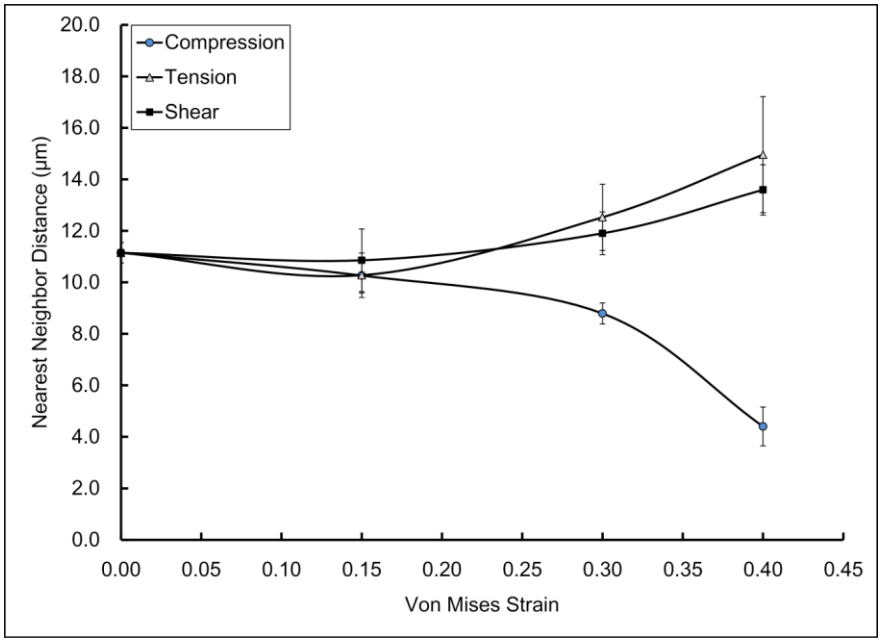

Figure 4.12 Nearest neighbor distance comparison for porcine brain under different stress states and strains.

Note: Error bars represent standard deviations.

4.4 Discussion and Conclusions

This study provides a structure-property relationship for porcine brain, which correlates the variations in the internal microstructure (i.e. arrangement of neurons and glial cells) to different stress states (e.g. compression, tension, and shear). While stress-strain plots captured the mechanical behavior, image analysis parameters such as area fraction and nearest neighbor distance captured the corresponding microstructural response. This work could be applicable toward understanding the secondary injury phase of TBI, which occurs hours or days after the initial physical impact (O'Connor et al., 2011). Secondary injury mechanisms include disrupted axonal transport, axonal swelling, and secondary axotomy (Johnson et al., 2013) but may also involve improper cytoskeleton alignment, denser compaction of neurofilaments, and deterioration of microtubules (Kelley et al., 2006). These secondary injury processes may occur if the homeostatic brain microstructure is sufficiently disrupted. Therefore, we quantified the layout of neurons and glial cells at different stress states and strains in order to develop a structure-property relationship. This coupled mechanical/microstructural characterization of the brain is necessary for eventually developing a more biofidelic FE brain model that can accurately depict damage progression.

The mechanical response of porcine brain under different stress states was also compared to similar studies reported in literature. For instance, the compressive response observed in this study was compared to previous research on porcine brain (Miller, 2000; 2005). Under quasistatic compression, porcine brain exhibited a hyperelastic response characterized by increased stiffening as the strain increased. Although these results were also observed by Miller (2000, 2005), this studied applied a strain rate (0.1 s^{-1}) that was

two orders of magnitude higher than the strain rate employed by Miller (0.006 s^{-1}). Consequently, the compressive response of porcine brain in this study demonstrated a more pronounced stiffening as the strain progressed. For a tensile stress state, porcine brain demonstrated a nonlinear mechanical response that was similarly observed by other investigators (Miller and Chinzei, 2002). Because this study employed a higher strain rate (0.1 s^{-1}) compared to Miller's work (0.006 s^{-1}), porcine brain subsequently exhibited more abrupt stiffening that started at a strain of approximately 0.03. This study also compared the shear response for porcine brain to previous work (Donnelly and Medige, 1997). However, the corresponding mechanical responses differed immensely due to two main factors. First, Donnelly and Medige (1997) performed oscillatory shear testing while this study utilized fixed-end shear testing. This difference in testing modalities produced more variability in their shear data compared to the results shown in Figure 4.6. Second, the inherent macroscopic differences between human and porcine brain could have also been a factor despite the similarly gyrencephalic structure (i.e. convolutions in the cerebral cortex). Furthermore, the use of human cadaver brains versus freshly procured porcine brains (within 3-4 hours after sacrifice) may have affected the initial microstructure and, therefore, magnified the differences in the respective mechanical responses.

Both tension and shear produced decreasing trends in area fraction and increasing trends in nearest neighbor distance. These results correspond to wider dispersions of neurons and glial cells due to increased stretching of the brain tissue. Conversely, compression led to an increasing area fraction and decreasing nearest neighbor distance, which could be attributed to a more densely packed arrangement of neurons and glial

cells caused by increased compaction of the brain tissue. Although the neurons and glial cells may individually experience each stress state at a lower extent, the surrounding extracellular matrix primarily experiences deformations from compression, tension, and shear, which could potentially induce the aforementioned secondary injury processes in an *in vivo* environment. The current structure-property relationship also showed that compression, tension, and shear produced nonlinear trends for area fraction and nearest neighbor distance. However, additional microstructural data many need to be collected at other strains (e.g. 0.05, 0.10, 0.20, 0.25, 0.35) in order to gain a more accurate depiction of these trends. Although this method would require exhaustive experimentation, this microstructural characterization combined with appropriate implementation of ISV principles could ultimately lead to a biofidelic FE model of the brain, which could capture damage from loading history effects. This study provides initial results from quantitative analysis of the microstructural composition of neurons and glial cells under all three stress states. However, these methods could be expanded through additional histological techniques to specifically track the microstructural integrity of other brain constituents (e.g. microglia, astrocytes) that emerge following TBI.

This study shows that at a quasistatic strain rate of 0.1 s^{-1}, porcine brain exhibits a characteristic mechanical response under compression, tension, and shear. Furthermore, image analysis parameters including the area fraction and nearest neighbor distance followed specific trends according to the stress state applied. As the strain increased, the area fraction subsequently increased under compression but decreased under tension and shear. Conversely, the nearest neighbor distance decreased under compression and increased under tension and shear as the strain progressed to 0.40. These image analysis

results indicate that variations in brain microstructure correspond to changes in stress state, which likely occurs during trauma. Although this work utilized quasistatic strain rates, we believe this data is applicable toward the study of TBI with an emphasis on the milder regime of injury, where typical pathology (e.g. macroscopic lesions) are often not present. In addition, our structure-property relationship for the brain may ultimately provide researchers with data that could lead to more effective mitigation of secondary injury. Researchers could also utilize this data to develop more biofidelic brain models that would not only expand predictive capabilities of FE simulations, but also lead to safer equipment design and improved diagnostic criteria for TBI.

4.5 References

Arbogast, K.B. and S.S. Margulies (1998). "Material Characterization of the Brainstem from Oscillatory Shear Tests." *Journal of Biomechanics* 31: 801-807.

Arbogast, K.B. and S.S. Margulies (1999). "A Fiber-Reinforced Composite Model of the Viscoelastic Behavior of the Brainstem in Shear." *Journal of Biomechanics* 32: 865-870.

Bain, A.C. and D.F. Meaney (2000). "Tissue-Level Thresholds for Axonal Damage in an Experimental Model of Central Nervous System White Matter Injury." *Journal of Biomechanical Engineering* 122: 615-622.

Begonia, M.T., R. Prabhu, J. Liao, M.F. Horstemeyer, and L.N. Williams (2010). "The Influence of Strain Rate Dependency on the Structure-Property Relations of Porcine Brain." *Annals of Biomedical Engineering* 38(10): 3043-3057.

Bouvard, J.L., D.K. Ward, D. Hossain, E.B. Marin, D.J. Bammann, and M.F. Horstemeyer (2010). "A General Inelastic Internal State Variable Model for Amorphous Glassy Polymers." *Acta Mechanica* 213: 71-96.

Brands, D.W.A., G.W.M. Peters, and P.H.M. Bovendeerd (2004). "Design and Numerical Implementation of a 3-D Non-Linear Viscoelastic Constitutive Model for Brain Tissue During Impact." *Journal of Biomechanics* 37: 127-134.

Cheng, S. and L.E. Bilston (2007). "Unconfined Compression of White Matter." *Journal of Biomechanics* 40: 117-124.

Darvish, K.K. and J.R. Crandall (2001). "Nonlinear Viscoelastic Effects in Oscillatory Shear Deformation of Brain Tissue." *Medical Engineering & Physics* 23: 633-645.

Donnelly, B.R. and J. Medige (1997). "Shear Properties of Human Brain Tissue." *Journal of Biomechanical Engineering* 119: 423-432.

Estes, M.S. and J.H. McElhaney (1970). *Response of Brain Tissue of Compressive Loading*. ASME Biomechanical and Human Factors Conference, Washington, D.C.

Galford, J.E. and J.H. McElhaney (1970). "A Viscoelastic Study of Scalp, Brain, and Dura." *Journal of Biomechanics* 3: 211-221.

Ho, J. and S. Kleiven (2009). "Can Sulci Protect the Brain from Traumatic Injury." *Journal of Biomechanics* 42: 2074-2080.

Horgan, T.J. and M.D. Gilchrist (2003). "The Creation of Three-Dimensional Finite Element Models for Simulating Head Impact Biomechanics." *International Journal of Crashworthiness* 8(4): 353-366.

Horstemeyer, M.F., J. Lathrop, A.M. Gokhale, and M. Dighe (2000). "Modeling Stress State Dependent Damage Evolution in a Cast Al-Si-Mg Aluminum Alloy." *Theoretical and Applied Fracture Mechanics* 33: 31-47.

Hrapko, M., J.A.W. van Dommelen, G.W.M. Peters, and J.S.H.M. Wismans (2006). "The Mechanical Behaviour of Brain Tissue: Large Strain Response and Constitutive Modelling." *Biorheology* 43: 623-636.

Johnson, V.E., W. Stewart, and D.H. Smith (2013). "Axonal Pathology in Traumatic Brain Injury." *Experimental Neurology* 246: 35-43.

Kelley, B.J., O. Farkas, J. Lifshitz, and J.T. Povlishock (2006). "Traumatic Axonal Injury in the Perisomatic Domain Triggers Ultrarapid Secondary Axotomy and Wallerian Degeneration." *Experimental Neurology* 198: 350-360.

Margulies, S.S., L.E. Thibault, and T.A. Gennarelli (1990). "Physical Model Simulations of Brain Injury in the Primate." *Journal of Biomechanics* 23: 823-836.

Miller, K. (2000). "Biomechanics of Soft Tissues." *Medical Science Monitor* 6(1): 158-167.

Miller, K. (2005). "Method of Testing Very Soft Biological Tissues in Compression." *Journal of Biomechanics* 38: 153-158.

Miller, K. and K. Chinzei (1997). "Constitutive Modelling of Brain Tissue: Experiment and Theory." *Journal of Biomechanics* 30(11): 1115-1121.

Miller, K. and K. Chinzei (2002). "Mechanical Properties of Brain Tissue in Tension." *Journal of Biomechanics* 35: 483-490.

Morrison III, B., H.L. Cater, C.D. Benham, and L.E. Sundstrom (2006). "An In Vitro Model of Traumatic Brain Injury Utilising Two-Dimensional Stretch of Organotypic Hippocampal Slice Cultures." *Journal of Neuroscience Methods* 150: 192-201.

Morrison III, B., D.F. Meaney, S.S. Margulies, and T.K. McIntosh (2000). "Dynamic Mechanical Stretrch of Organotypic Brain Slice Cultures Induces Differential Genomic Expression: Relationship to Mechanical Parameters." *Journal of Biomechanical Engineering* 122: 224-230.

Nicolle, S., M. Lounis, and R. Willinger (2004). "Shear Properties of Brain Tissue Over a Frequency Range Relevant for Automotive Impact Situations: New Experimental Results." *Stapp Car Crash Journal* 48: 239-258.

O'Connor, W.T., A. Smyth, and M.D. Gilchrist (2011). "Animal Models of Traumatic Brain Injury: A Critical Evaluation." *Pharmacology & Therapeutics* 130, 106-113.

Pervin, F. and W.W. Chen (2011). "Effect of Inter-Species, Gender, and Breeding on the Mechanical Behavior of Brain Tissue." *NeuroImage* 54: S98-S102.

Prabhu, R., M.F. Horstemeyer, M.T. Tucker, E.B. Marin, J.L. Bouvard, J.A. Sherburn, J. Liao, and L.N. Williams (2011). "Coupled Experimental/Finite Element Analysis on the Mechanical Response of Porcine Brain Under High Strain Rates." *Journal of the Mechanical Behavior of Biomedical Materials* 4: 1067-1080.

Prange, M.T. and S.S. Margulies (2002). "Regional, Directional, and Age-Dependent Properties of the Brain Undergoing Large Deformation." *Journal of Biomechanical Engineering* 124: 244-252.

Prange, M.T., D.F. Meaney, and S.S. Margulies (2000). "Defining Brain Mechanical Properties: Effects of Region, Direction, and Species." *Proceedings of the 44th Stapp Car Crash Conference*: 205-213.

Rashid, B., M. Destrade, and M.D. Gilchrist (2012). "Mechanical Characterization of Brain Tissue in Tension at Dynamic Strain Rates." *Journal of the Mechanical Behavior of Biomedical Materials*.

Takhounts, E.G., S.A. Ridella, V. Hasija, R.E. Tannous, J.Q. Campbell, D. Malone, K. Danelson, J. Stitzel, S. Rowson, and S. Duma (2008). "Investigation of Traumatic Brain Injuries Using the Next Generation of Simulated Injury Monitor (SIMon) Finite Element Head Model." *Stapp Car Crash Journal* 52.

Tamura, A., S. Hayashi, I. Watanabe, K. Nagayama, and T. Matsumoto (2007). "Mechanical Characterization of Brain Tissue in High-Rate Compression." *Journal of Biomechanical Science and Engineering* 2(3): 115-126.

Velardi, F., F. Fraternali, and M. Angelillo (2006). "Anisotropic Constitutive Equations and Experimental Tensile Behavior of Brain Tissue." *Biomechanics and Modeling in Mechanobiology* 5: 53-61.

Weed, B.C., A. Borazjani, S.S. Patnaik, R. Prabhu, M.F. Horstemeyer, P.L. Ryan, T. Franz, L.N. Williams, and J. Liao (2012). "Stress State and Strain Rate Dependence of the Human Placenta." *Annals of Biomedical Engineering* 40(10): 2255-2265.

Wright, R.M. and K.T. Ramesh (2012). "An Axonal Strain Injury Criterion for Traumatic Brain Injury." *Biomechanics and Modeling in Mechanobiology* 11: 245-260.

CHAPTER V

CONCLUSIONS

In vivo experiments were performed on Sprague-Dawley rats to simulate mild levels of blunt and blast trauma, which produced microstructural alterations in the brain that were quantified through both DTI and image analysis. Reductions in the fiber count and nearest neighbor distance were observed and attributed to diverted water diffusion following injury. However, a consistent fiber length and differential changes in FA were not anticipated and may have been influenced by various factors including axonal pathology or edema. Future studies should focus on the underlying mechanisms that differentiate blunt and blast trauma, especially since DTI results produced a decreased FA following blunt injuries and an increased FA following blast injuries.

Von Mises stress, pressure, and maximum principal strain were selected for examining the mechanical behavior of the skull and multiple brain regions following blunt and blast trauma. Finite element (FE) simulations of blast trauma were performed twice with the first utilizing the initial blast profile from experimental data and the second utilizing an adjusted blast profile, which possessed a cumulative impulse that was equivalent to the cumulative impulse calculated from blunt trauma. In the skull, cerebral cortex, corpus callosum, and hypothalamus, blast trauma produced von Mises stress responses that were characterized by a more fluctuating trend than in blunt trauma. Furthermore, the three brain structures exhibited higher von Mises stresses after blast

trauma while the skull exhibited a higher von Mises stress following blunt trauma. A comparison of pressure responses in all four head regions revealed that blast trauma generated higher peak pressures than blunt trauma. Blast trauma also produced more oscillations in the corresponding pressure responses with the hypothalamus exhibiting an initial tensile response. Higher values for the maximum principal strain were observed in both the cerebral cortex and corpus callosum compared to other brain regions. These results could be attributed to the vicinity of both the cerebral cortex and the corpus callosum to the initial impact site.

In vitro experiments at a quasistatic strain rate of 0.1 s^{-1} showed that porcine brain exhibits a characteristic mechanical response under compression, tension, and shear. Image analysis parameters including the area fraction and nearest neighbor distance followed certain trends that corresponded to the stress state applied. As the strain increased, the area fraction subsequently increased under compression but decreased under tension and shear. Conversely, the nearest neighbor distance decreased under compression and increased under tension and shear as the strain progressed to 0.40. Although this work utilized quasistatic strain rates, this data is beneficial toward the study of TBI with an emphasis on the milder regime of injury in which typical pathology (e.g. macroscopic lesions) is often not present. Successful treatment of TBI depends on health care professionals and their abilities to effectively mitigate the secondary injury mechanisms that result from an initial physical trauma. Capturing the stress state dependent microstructural phenomena within the brain provides the key toward enhancing current thresholds for injury. Researchers can subsequently utilize this data to develop more biofidelic brain models that would not only expand predictive capabilities

of FE simulations, but could also lead to safer equipment design and improved diagnostic criteria for TBI.

CHAPTER VI

FUTURE WORK

6.1 Enhanced Biomechanical Testing

Although the experimental setup utilized for the dissertation study was sufficient, improvements to the test device could still be made in an effort to enable easier biomechanical testing. For instance, the mount for the pressure vessel could be modified to allow a vertical setup for both blunt and blast experiments. This adjustable setup would facilitate animal positioning and also reduce the space required to perform tests. In addition, the animal stage could be redesigned to allow rotational acceleration of the head, which is a biomechanical factor that contributes to DAI. This design feature could also enable quicker repositioning of the animal following an impact test, thereby facilitating a study on repetitive head injury.

The manner in which head impacts are generated could also be adapted to reproduce more realistic injury conditions. To the author's knowledge, experimental models have been designed to reproduce either blunt or blast trauma separately, but not both sequentially. In mTBI scenarios, military personnel often experience blast trauma due to the pressure wave from an IED as well as blunt trauma from subsequent head impacts. Developing an experimental model that recreated both injury events sequentially would be novel. The current test device may potentially achieve this objective through a few experimental modifications. First, the test device could be

vertically positioned underneath the head of the animal with the opening of the test device facing upward. Second, the animal's head could be placed inside a rigid structure, thus simulating a soldier confined within an armored vehicle. The resulting setup would expose the animal to blast trauma from the test apparatus in addition to blunt trauma from the rigid encasing. This experimental model could be further adapted to recreate an open-field blast through the simple removal of the rigid covering. Although this modified setup would be more difficult to perform in a reproducible manner, it would enable more extreme head rotations to occur.

6.2 Enhanced Mesh for the Rodent Brain

This study utilized a rodent brain mesh with various external features including the olfactory bulb, cerebellum, and brainstem. Due to limitations in scan time and the lack of a small animal coil, however, there was insufficient image resolution to clearly delineate internal structures such as the corpus callosum, thalamus, and hypothalamus. These regions were manually identified as individual element sets in ABAQUS Explicit 6.10-3 (ref), but this process could be facilitated with higher quality MRI or CT scans of the rodent brain. Fortunately, the Duke University Center for In Vivo Microscopy (CIVM) has a multiple high-contrast image volumes of an adult male Wistar rat brain that could be imported into ScanIP. Figure 6.1 shows the 4-view display of a TIFF image stack imported from the CIVM online database. Researchers acquired images with a 7.0T small animal MRI system and perfused the brain with an MRI contrast agent. In addition, researchers immersed the brain in liquid fluorocarbon inside custom-built MRI-compatible tubes, which prevented specimen dehydration and reduced the potential for imaging artifacts (Johnson et al., 2012). Figure 6.2 shows the results of preliminary

segmentation with the red mask indicating the entire brain and the cyan mask identifying the corpus callosum.

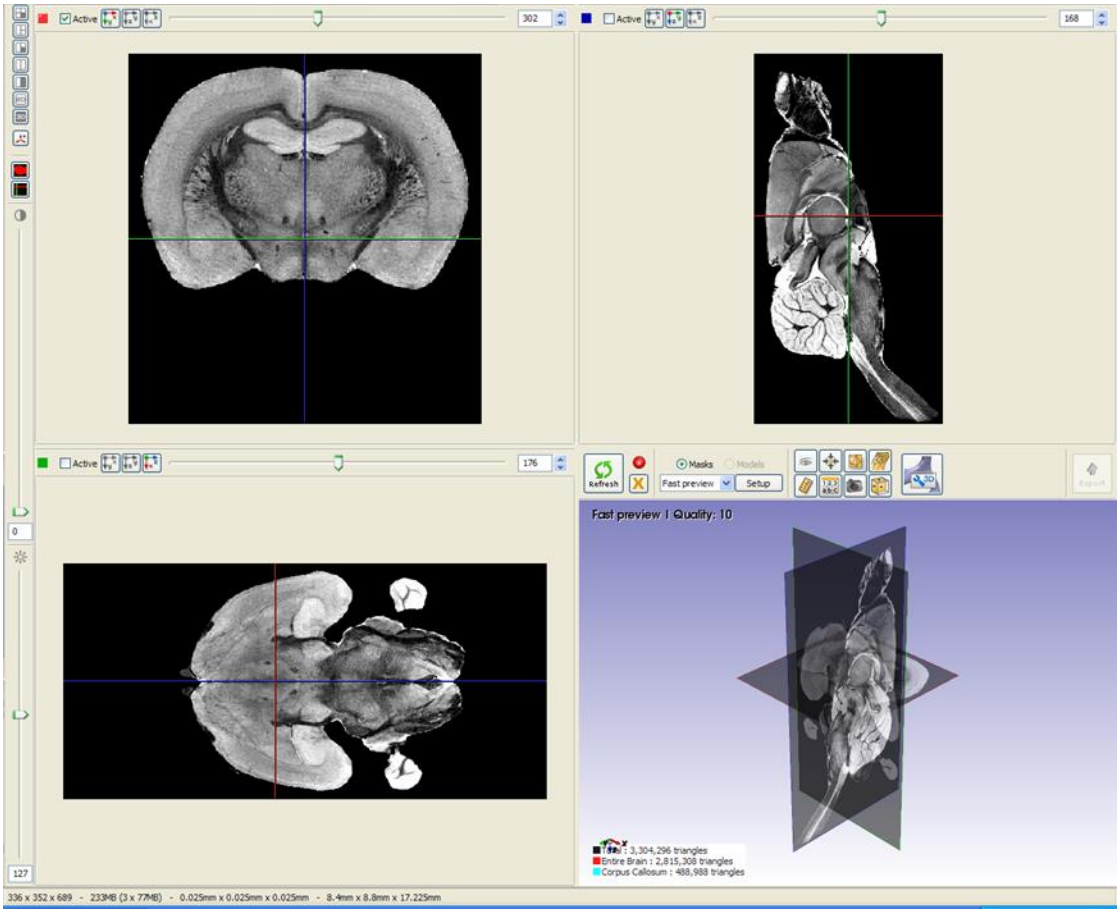

Figure 6.1 TIFF stack of adult Wistar rat brain imported into ScanIP from the Duke University Center for In Vivo Microscopy (CIVM).

Note: (www.civm.duhs.duke.edu/neuro201001/index.html).

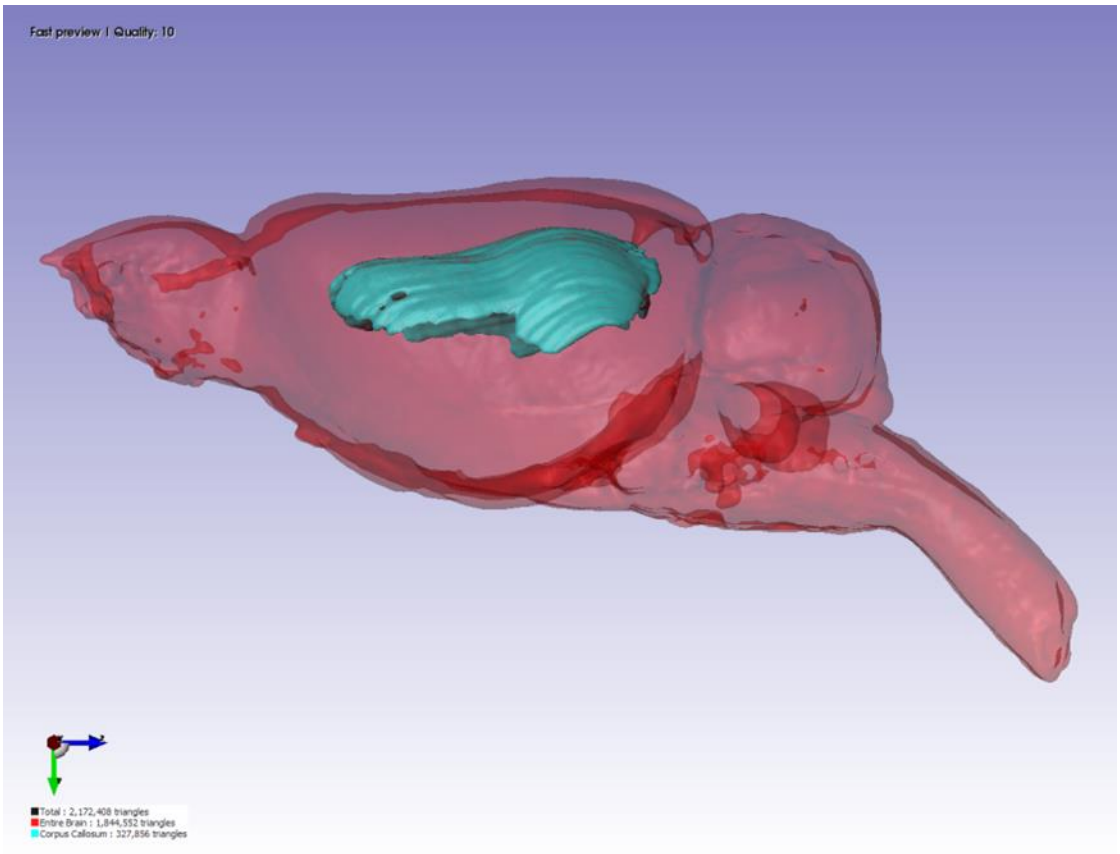

Figure 6.2 Preliminary segmentation of CIVM brain that shows the entire brain (red) and corpus callosum (cyan).

An accompanying atlas of the male Wistar rat brain (Watson and Paxinos, 2007) can also be referenced while attempting to segment more detailed internal brain structures. Figure 6.3 shows a scanned image overlaid with a histological section, which illustrates the level of detail achieved by CIVM. An experienced ScanIP user could utilize the thresholding algorithms and manual segmentation to generate a brain mesh with predefined regions. In addition, an experienced ScanIP user could also create contact pairs in order to automatically generate contact surfaces in ABAQUS Explicit,

which would facilitate the process of selecting and analyzing the field outputs of specific brain regions.

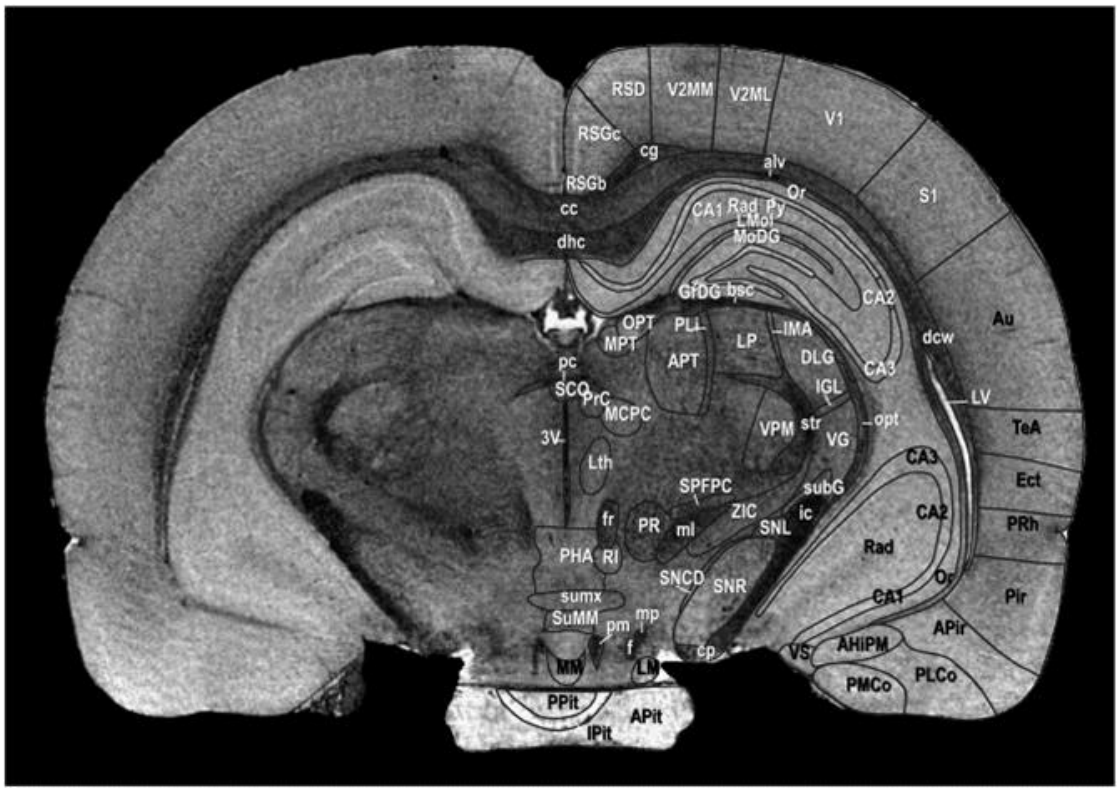

Figure 6.3 Annotated coronal GRE image corresponding to Figure 71 (interaural 4.44 mm) in Watson and Paxinos, 2007.

6.3 Mechanical Response of Microstructural Brain Components

A separate analysis focusing on the mechanical response of various brain constituents (e.g. neurons, axons, astrocytes, oligodendrocytes) would be beneficial toward the study of mTBI. Researchers employ a variety of histological techniques to examine the progression of microstructural damage in the brain following injury. In addition, recent neuroimaging modalities such as DTI provide researchers with *in vivo*

visualization of microstructural changes within the brain. The underlying mechanisms of mTBI are inferred from pathological and neuroimaging findings and are most likely associated with the individual stress-strain responses of these microstructural components. Obtaining stress-strain data through experiments remains a challenge; however, this data could conceivably be determined through computational means.

A method for analyzing the stress-strain response of individual brain components would require multiple steps that include histological processing, image segmentation, and molecular dynamic (MD) simulations. First, serial sections of brain tissue before and after injury should be collected and stained appropriately to visualize the corresponding cellular structures in the brain. Second, numerous serial sections could be imaged in order to create an image volume that could be imported into ScanIP. An individual could utilize these image stacks to generate 3-D models corresponding to finite sections of the brain before and after injury. Furthermore, these ScanIP models could be used as templates for constructing MD-based models with enhanced structural details for multiple brain constituents, which could then be arranged in various ways to represent different brain regions such as white matter or gray matter. Although achieving this level of sophistication could prove to be exhaustive, the resulting MD-based model would be novel and adaptable to a wide range of biomechanical conditions.

6.4 References

Johnson, G.A., E. Calabrese, A. Badea, G. Paxinos, and C. Watson (2012). "A Multidimensional Magnetic Resonance Histology Atlas of the Wister Rat Brain." *NeuroImage* 62: 1848-1856.

Watson, C. and G. Paxinos (2007). *The Rat Brain in Stereotaxic Coordinates*. New York, Academic Press.